Seasonal and Multi-year Variability of Ice Dynamics of South Croker Bay Glacier, Devon Ice Cap, Canadian Arctic from 2015 to 2021

by

Natalija Nikolić

A thesis

presented to the University of Waterloo

in fulfillment of the

thesis requirement for the degree of

Master of Science

in

Geography

Waterloo, Ontario, Canada, 2023

Author's Declaration

This thesis consists of material all of which I authored or co-authored: see Statement of Contributions included in the thesis. This is a true copy of the thesis, including any required final revisions, as accepted by my examiners.

I understand that my thesis may be made electronically available to the public.

Statement of Contributions

This thesis is presented in the manuscript option, with Chapter 4 containing the manuscript named “Seasonal and Multi-year Variability of Ice Dynamics of South Croker Bay Glacier, Devon Ice Cap, Canadian Arctic from 2015 to 2021” which has been written for submission to the *Journal of Glaciology* (or a journal of similar scope). Natalija Nikolić conducted all analysis and data processing in the manuscript, under the supervision of Dr. Wesley Van Wychen. TerraSAR-X data and editorial comments were provided by Anna Wendleder.

Abstract

The effects of climate change have already been observed across the globe, impacting weather, ecosystems, and society. These effects have been most pronounced in polar regions, which experience warming at a faster rate than other latitudes due to positive feedbacks resulting from reduced ice and snow cover. Compared to the 1.1^{o}C of warming around the globe since the 1980s, the Arctic has warmed by 3^{o}C. Glaciers and ice caps are of particular concern as they have profound impacts on water resources, shipping and travel routes, and global sea level rise. As such, glacier dynamics play a key role in understanding effects on the global system. The Canadian High Arctic in particular has doubled in rates of mass loss since the 1990s, which is of great concern as it is the third largest contributor to global sea level rise after Antarctica and Greenland. While glacier flow within the region has been studied, some glaciers have been observed to not align with current understandings of dynamics. The subject of this study, South Croker Bay Glacier, located on Devon Ice Cap in Nunavut, Canada has exhibited velocity variability on oscillating temporal scales which do not align with surging, pulsing, or consistent acceleration explanations. The primary objective of this thesis was to create a dense record of velocities derived from TerraSAR-X imagery every 11 days from 2015 to 2021 to gain insight into seasonal and multi-annual velocity variability. As a result, a near-continuous velocity record of South Croker Bay Glacier has been created, highlighting a shift in velocities which occurred during the winter of 2018/19. The second objective was to explore the potential drivers of the observed velocity variability, which were hydrology, sea ice buttressing, and bed topography. Looking at the spatial propagation of acceleration and terminus position as well, it is concluded that the variability is not driven by surge- or pulse-type mechanisms. Instead, it is suggested that the driver of the observed variability on the glacier is the result of the evolving configuration of the hydrological network. This is supported by surface air temperature and surface lake area records during the study period. Finally, the third objective was to assess the feasibility of utilizing remote sensing for seasonal variability detection. Based on the analysis, the method was successful in the proposed objectives, creating a record of velocities that was not previously available for South Croker Bay Glacier.

Acknowledgements

I would first like to acknowledge Wesley Van Wychen, my supervisor who has given me the opportunity to work on this research. Without the endless support through advising and editing my work, and the number of opportunities he has provided me ranging from field experience to international conferences, this work would not have been possible. You have taught me more than I could have asked for and created a supportive lab group as well. I would also like to acknowledge my lab mates, Lauren Samo, Courtney Bayer, Monika Wagner, and Danielle Hallé for being a source of support and valuable feedback.

I would also like to acknowledge my parents, Nevenka and Petar, for the sacrifices they have made in their lives to give me the opportunity and resources to pursue an education. Finally, I'd like to acknowledge all of the support Nikola has given me.

Table of Contents

List of Figures

List of Tables

List of Abbreviations

a.s.l	Above Sea Level
AWS	Automated Weather Station
CAA	Canadian Arctic Archipelago
CHA	Canadian High Arctic
DEM	Digital Elevation Model
DIC	Devon Ice Cap
DLR	German Aerospace Center
EDN	Efficient Drainage Network
EMR	Electromagnetic Radiation
FR	Flow Regime
GPS	Global Positioning System
GRD	Ground Range Detected
HH	Horizontal-Horizontal
HV	Horizontal-Vertical
IDN	Inefficient Drainage Network
L8/9	Landsat-8/9
MB	Mass Balance
OLI	Operational Land Imager
OIB	NASA's Operation IceBridge
PDD	Positive Degree Day
QEI	Queen Elizabeth Islands
RADAR	Radio Detection And Ranging
RGI	Randolph Glacier Inventory
R2	RADARSAT-2
SAR	Synthetic Aperture RADAR
SATs	Surface Air Temperatures
SCB Glacier	South Croker Bay Glacier
sd	Standard Deviation
SLC	Single Look Complex
SMB	Surface Mass Balance

S2	Sentinel-2
TDX	TanDEM-X
TRIS	Thermal Infrared Sensor
TSX	TerraSAR-X
VV	Vertical-Vertical
VH	Vertical-Horizontal

Chapter 1 - Introduction

1.1 Overview and Research Objectives

Climate change is an undeniable reality, and it is putting ecosystems and people at risk (Abram et al., 2019). Compared to non-Arctic latitudes, the Arctic will be disproportionately affected by climate change due to polar amplification (caused by the feedback mechanisms which are affected by snow, ice, and permafrost) (Abram et al., 2019). As such, contemporary climate change has major implications for glacier dynamics and mass balance, which increases and intensifies regional contributions of terrestrial ice to global sea level rise via mechanisms of mass loss (Boon et al., 2010; Strozzi et al., 2017). In order to understand and project the larger scale global impacts of climate change, measuring and quantifying the evolution of the Arctic's physical environment is a crucial first step (Schellenberger et al., 2016). The effects of climate change can already be identified in the Canadian High Arctic (CHA), with reduced snow cover duration and accumulation, reduced lake ice duration, thawing of permafrost, thinning of sea ice, and the loss of multi-year ice (Derksen et al., 2019). Effects on glaciers and ice caps have been observed through the rates of thinning and mass loss in the CHA accelerating in recent years as a result of rising air temperatures (Derksen et al., 2019). The CHA is the third largest contributor to global sea level rise after Greenland and Antarctica (Derksen et al., 2019), which makes understanding the glacier dynamics in the region important as it helps refine estimates of sea level rise (Van Wychen et al., 2016).

The majority of winter surface velocities observed on glaciers in the CHA have remained relatively consistent from 2015 to 2020 (Van Wychen et al., 2020; section 2.3.6 Trends in the Velocity Structure CAA). This is true for Devon Ice Cap (DIC), Nunavut, Canada where the interior of the ice cap is assumed to be frozen to the bed, with surface velocities of < 20 m a^{-1} observed (indicating that the flow dynamics are driven by internal deformation) (Van Wychen et al., 2012; section 2.2.1 Ice flow processes and dynamics). While the majority of research focuses on DIC's larger glaciers (i.e. Belcher Glacier), smaller glaciers have not been examined to the same degree. For example, there is currently little understanding of the dynamics of the third fastest flowing glacier on DIC, South Croker Bay (SCB) Glacier (Figure 2-1) which has exhibited highly variable surface velocities which do not fit within the processes already identified in the Canadian

Arctic Archipelago (CAA) (i.e. surging, pulsing, or consistent acceleration; section 2.2.1 Ice flow processes and dynamics) (Van Wychen et al., 2017; 2020). With the growing volume of data available from Synthetic Aperture RADAR (SAR) satellites (i.e. TerraSAR-X, RADARSAT-2; section 3.1 Datasets), our ability to investigate the poorly understood dynamics of SCB Glacier, and other glaciers in secluded Arctic environments grows as well. The current body of literature reports interannual variability during the winters with oscillating periods of faster and slower flow for South Croker Bay Glacier (Van Wychen et al., 2017; 2020), but generally it has been found to be one of the only glaciers on DIC which has been generally increasing in velocity since 1991 (Millan et al., 2017).

This pattern differs from surge-type glaciers, which exhibit cyclical fluctuations in velocity from a short phase of surging (months to years) where velocities accelerate and transport mass down glacier from the thicker upper reaches; to a longer phase of quiescence (decades to centuries) where velocities are at a minimum (Copland et al., 2003). During this time the ablation zone thins while the accumulation area gains mass (Copland et al., 2003). SCB Glacier's velocities also vary from pulse-type flow variability, which is the other main mechanism that has been identified in the Canadian Arctic as modifying glacier motion. Pulsing is characterized by regions of the glacier grounded below sea level experiencing either multiple years of deceleration or acceleration, initiating up glacier from near terminus region, followed by a slowdown (Van Wychen et al., 2016). Given that the dynamics of SCB Glacier do not fit fully into either of these categories, the process driving the dynamics of this glacier warrants further investigation. While SCB Glacier experiences multiple years of deceleration and acceleration in the near terminus region, the velocity variability extends up to 15 km from the terminus into areas of the glacier which are above sea level. As such, to identify the processes occurring on SCB Glacier and understand why they differ from the surge- and pulse-type glaciers in the CHA we must first characterize the variability that is occurring. While interannual velocities have been investigated they have not yet been the focus of a singular study (Van Wychen et al., 2017; 2020; Millan et al., 2017), and intraannual dynamics have not yet been examined. The increasing volume of available data presents an opportunity to build upon findings presented in existing literature. As such, this study focuses on quantifying the seasonal and multi-annual changes in ice velocity for South Croker Bay Glacier on Devon Ice Cap, Nunavut, Canada (Figure 2-1).

1.1.1 Research Objectives

The specific objectives of this thesis are to:

1) Quantify the seasonal and multi-annual ice motion of SCB Glacier, a major tidewater terminating glacier on DIC primarily using remote sensing data and methods;
2) Examine the relationship between sea ice conditions, hydrology and glacier bed topography as drivers and controls on the observed variability; and
3) Assess the feasibility of using remote sensing methods to track seasonal changes in glacier motion in the Canadian High Arctic.

The study period spans from 2015 to 2021, during which there is a large archive of remotely sensed data (TerraSAR-X, Landsat 8/9, and Sentinel-2; section 3.1 Datasets and Processing Methods) that is utilized to complete this analysis.

1. 2 Thesis structure

This thesis consists of five chapters and follows a 'thesis by manuscript' format. - Introduction is the introduction, in which an overview of the research problem and research objectives are provided. In - Study Site and Literature Review, background to the study area, glacier processes, and general trends in the area are described. - Methodology details the methodology of the study, as well as a description of the relevant theoretical background. - Seasonal and Multi-year Variability of Ice Dynamics of South Croker Bay Glacier, Devon Ice Cap, Canadian Arctic from 2015 to 2021 presents the manuscript titled *Seasonal and Multi-year Variability of Ice Dynamics of South Croker Bay Glacier, Devon Ice Cap, Canadian Arctic from 2015 to 2021* which is written for submission to the Journal of Glaciology (or a journal of a similar scope). Finally, Conclusions is the conclusion of the research, in which the research objectives and outcomes are summarized, and future research is identified.

Chapter 2 - Study Site and Literature Review

This chapter provides a broad description and overview to the Devon Ice Cap and South Croker Bay Glacier as a study site, then transitions into a literature review which provides a broad background to the relevant glacier processes needed as context for this thesis.

2.1 Study Area

The study area of this research is South Croker Bay Glacier, Devon Ice Cap, Devon Island, Nunavut, Canada (Figure 2-1). Of all the ice masses in the CAA, DIC is one of the most intensely studied, being the only ice mass that has been regularly surveyed with in situ mass balance measurements since 1951 (Boon et al., 2010; Sharp et al., 2014). From a glacier dynamics perspective, the first mapping of surface ice velocities for DIC was completed by Burgess and others (2005), using InSAR techniques applied to the SAR based European Remote Sensing 1 and 2 satellites on scenes from the mid-1990s (Sharp et al., 2014). Since then, this work has been built on by tracking interannual glacier dynamics and variability (Van Wychen et al., 2012; 2017; 2020; Millan et al., 2017); and estimating discharge to the ocean via surface velocities (Van Wychen et al., 2012; 2014; 2017; 2020; Millan et al., 2017; Shepherd et al., 2007). DIC is the southernmost ice cap of the eight major ice caps in the Queen Elizabeth Islands (QEI) (Figure 2-1a) (Millan et al., 2017), with an area of ~14,000 km^2 and summit elevation of 1930 m a.s.l. (Noël et al, 2018; Mair et al., 2005; Dowdeswell et al., 2004). This area is one of the largest contributors of ice discharge in the QEI, discharging an average of 0.46 Gt a^{-1} between 1991 and 2015 (Millan et al., 2017), with other studies finding similar results of 0.41 Gt a^{-1} during overlapping periods (Figure 2-2; Van Wychen et al., 2017). The melt season usually starts in early June to July and drives 90% of seasonal mass balance variability rather than annual variation in precipitation, which is on average ~ 320 mm w.e. a^{-1} (Sharp et al., 2014; Boon et al., 2010).

DIC has 11 tidewater terminating glaciers, 1 piedmont lobe, and some land terminating glaciers, with 8% of the ice cap being situated below sea level (Van Wychen et al., 2020; Dowdeswell et al., 2004). Differences exist between the flow patterns on the east and west side of the ice cap, where the western half is predominantly moving by sheet flow (< 15 m a^{-1}), aside from several rapidly flowing glaciers along the southwest margin which is seen most prominently up-

glacier of SCB Glacier and neighbouring North Croker Bay Glacier, where the elevated velocities propagate up to > 20 km inland from the ice cap margin (Burgess et al., 2005). DIC experiences long, cold winters which are punctuated by short, cool summers; changes in summer melt (surface mass balance (SMB) loss) rather than changes in winter precipitation (SMB accumulation) is likely the driver of mass loss, which is a common trend in the QEI (Van Wychen et al., 2014; 2020; Noël et al, 2018). This is important because there has been an identified doubling of glacier motion during the summer, which is hypothesized to be driven by basal lubrication, causing annual discharge to be 7% higher than that of the winter season (Shepherd et al., 2007).

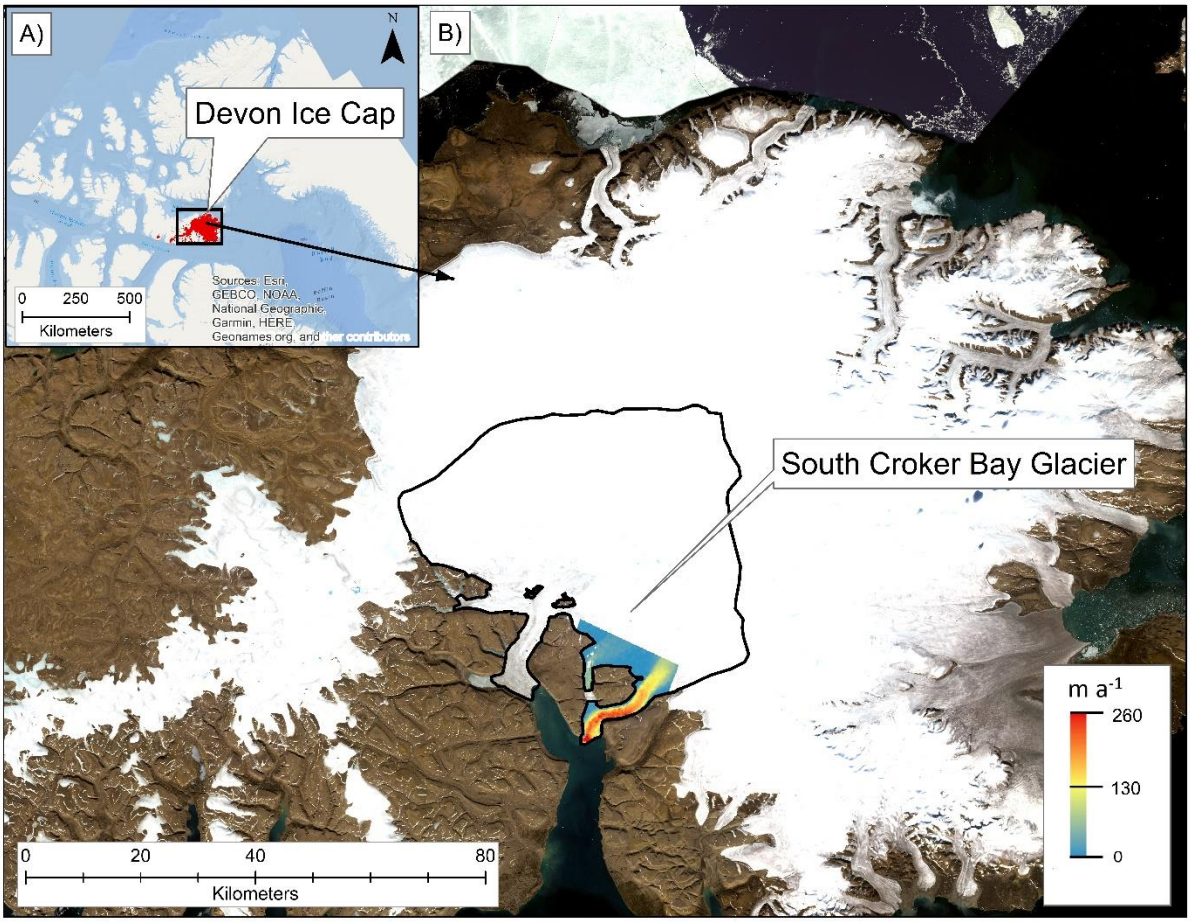

Figure 2-1: A) Devon Ice Cap highlighted in red within the Queen Elizabeth Islands; B) SCB Glacier basin outlined in black on Devon Ice Cap with TSX/TDX derived velocities overlaid on a cloud free Landsat-7 image

Generally, the velocity structure of DIC is dominated by slow flow (<20 m a^{-1}) in the interior regions (suggesting that ice in this area is frozen to the bed), with higher velocities occurring on tidewater, outlet glaciers (>20 m a^{-1}) (Figure 2-1; Burgess et al., 2005; Van Wychen

et al., 2012; 2017). The fastest velocities on the ice cap are observed at the termini of Belcher and Fitzroy Glaciers with speeds ≥ 300 m a^{-1} before 2015 (Van Wychen et al., 2017), accelerating up to > 400 m a^{-1} after 2015 (Van Wychen et al., 2020). SCB Glacier is the third fastest flowing glacier on the ice cap (Millan et al., 2017), with velocities ranging from 120 to 180 m a^{-1}, while other outlet glaciers have speeds of 60-150 m a^{-1} (Van Wychen et al., 2017). Areas of greatest dynamic variability on the ice cap occur where the glacier is grounded below sea level, suggesting that bed morphology is a significant factor in flow regulation (Van Wychen et al., 2017). Seasonal velocity variability is expected in these areas as well due to the flow regime mapping completed by previous studies, which is further described in Section 2.2.1 Ice flow processes and dynamics.

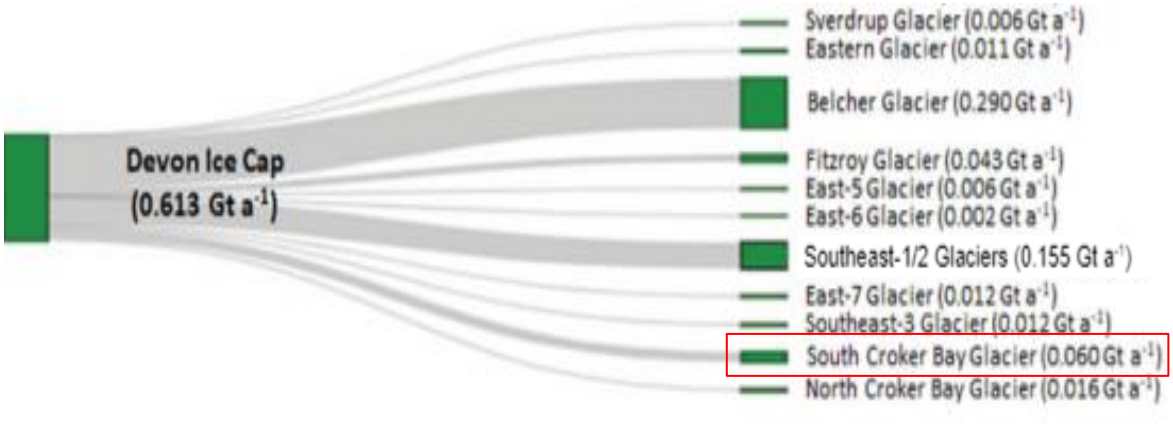

Figure 2-2. Distribution of ice discharged to the ocean from the Devon Ice Cap broken down by ice mass and glacier, for winter 2019/2020 (Modified from Van Wychen et al., 2020).

Discharge from the ice cap has been previously calculated using ice thickness (NASA's Operation IceBridge; Paden et al., 2010) and depth-averaged ice velocity data (Van Wychen et al., 2012; Millan et al., 2017), with recent studies reporting total discharge for Devon Ice Cap in 2019/20 as 0.613 Gt a^{-1} (Figure 2-2; Van Wychen et al., 2020). However, discharge from the ice cap is sensitive to the changing dynamics of a few individual glaciers, which makes characterizing variability in ice motion important for estimating future contributions (Van Wychen et al., 2014). Indeed, recent studies (Van Wychen et al., 2020) have indicated that South Croker Bay has experienced significant variability in glacier flow since 1999. With this context, the next section focusses on the characteristics of SCB Glacier itself.

2.1.1 South Croker Bay Glacier

Located in the southwestern quadrant of DIC, SCB Glacier is a ~43 km long glacier with two main tributaries terminating in Lancaster Sound (Figure 2-1b; Burgess et al., 2005). During the winter of 2018-2019 the highest velocity measurements in the lowermost 12 km of the glacier were observed to be > 200 m a^{-1} since 2015 (Van Wychen et al., 2020). The underlying bed material is speculated to be composed of marine till in the terminus region, which is grounded below sea level, with a bedrock step located ~18 km up-glacier from the terminus (potentially acting as a pinning point) (Dowdeswell et al., 2004). Faster velocities are initiated down glacier of this bedrock step, occurring where the bed descends below sea level (Dowdeswell et al., 2004). High driving stress and increased velocities occur up to 22 km from the terminus of South Croker Bay Glacier, placing this region of the glacier within the 'flow regime 3' classification (described further in section 2.2.1 Ice flow processes and dynamics; Burgess et al., 2005; Van Wychen et al., 2017).

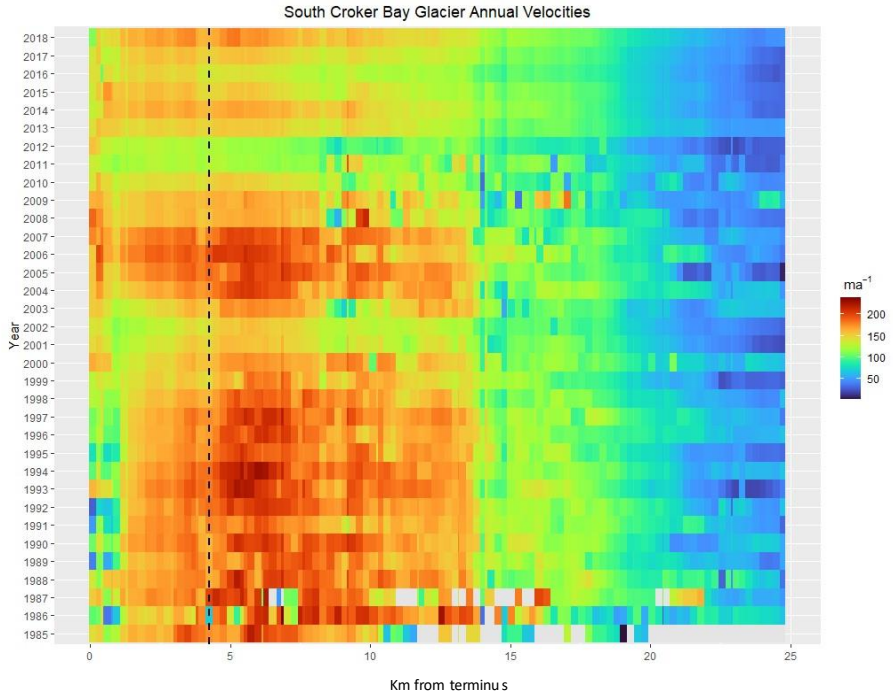

Figure 2-3. Centerline South Croker Bay Glacier velocities from 1985-2018 provided by the NASA Its-LIVE project (https://its-live.jpl.nasa.gov/)

Figure 2-3 illustrates the large degree of velocity variability from year to year. Velocity mapping of SCB Glacier in 1999 compared to measurements from 2018/19 show a speed up from

~120 m a^{-1} to >200 m a^{-1} in the lowermost 12 km of the glacier (Figure 2-3; Van Wychen et al., 2020). This variability has not yet been fully attributed to any processes, nor does it fit into any glacier surge types (pulsing or surging) as the velocity uniformly accelerates and decelerates at unequal intervals along the trunk of the glacier. As such there must be another mechanism causing this behaviour that is yet to be identified (Van Wychen et al., 2017).

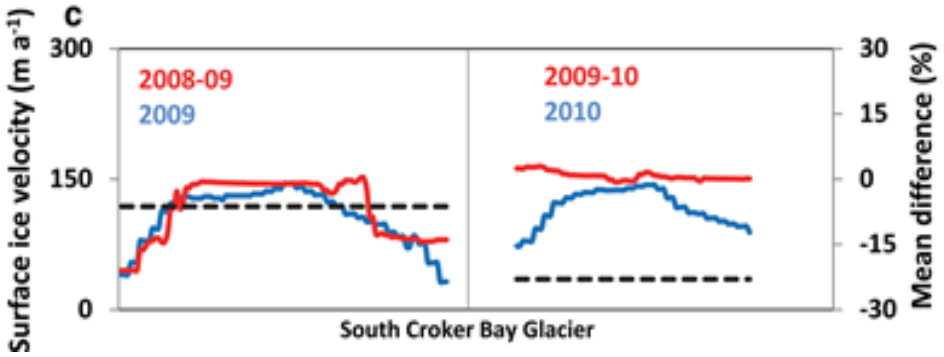

Figure 2-4. South Croker Bay cross section comparison of near-terminus flux gates between feature tracking and speckle tracking, red lines denote feature tracked results and blue lines denote speckle tracked results (Modified from Van Wychen et al., 2017)

In terms of seasonality, results from Van Wychen et al., (2016) have indicated the presence of a seasonal signal when comparing annual and winter-only velocities (Figure 2-4). This was further supported by the terminus velocity structure detected in annual velocities displaying signs of plug flow (uniform flow along the valley width, unconstrained by the wall) (Figure 2-4 right pane), which when combined with the increased interannual variability occurring since 2003 makes it an interesting candidate to further explore its seasonality (Van Wychen et al., 2020). There currently has not yet been an in-depth investigation of this using either in situ or remote sensing methods.

2.2 Background and Literature Review

2.2.1 Ice flow processes and dynamics

Glaciers are terrestrial based ice which form through the accumulation of snow, which transitions to firn over time due to the pressure of overlying snow (Benn and Evans, 2010). Firn is an intermediate state between snow and ice, becoming increasingly dense as it transitions to ice

(Benn and Evans, 2010). This ice then begins to flow like a frozen river, pulled downslope by gravity from the accumulation area towards the ablation zone, where mass is generally lost and requires replenishment in order to persist (Benn and Evans, 2010). The rate at which a glacier flows is dependent on the stress applied to it as well as the processes of glacier motion (Benn and Evans, 2010). Stresses applied to glacier include gravitational stress and resistive stress. The former is variable depending on the density of the ice, gravitational acceleration, ice thickness, and surface slope; and the latter pertains to longitudinal forces, basal and lateral drag (Benn and Evans, 2010).

There are three main processes by which glaciers flow; internal deformation (also commonly referred to as ice creep), basal sliding, and soft bed deformation (Benn and Evans, 2010). Internal deformation occurs on all glaciers as a result of the weight of the ice on the crystal fabric (Benn and Evans, 2010). Rather than acting as a brittle material, ice acts as a plastic due to the pressure exerted on it, allowing ice crystals to slide over one another (Benn and Evans, 2010). Ice deforms preferentially in the direction of least resistance, which is most commonly in the direction which crystals are aligned (Benn and Evans, 2010). Water content can also act as a contributor to increased crystal movement as it acts as a lubricant to allow for increased sliding (Benn and Evans, 2010). As such this process is a function of applied stress, ice softness, and temperature. Temperature impacts how easily ice is deformed, as warmer ice is more malleable than colder ice (Benn and Evans, 2010). Impurities in the ice can also impact this process, with some acting to harden the ice while others can soften (Benn and Evans, 2010).

Basal sliding only occurs on glaciers that are approaching melting point at their base, as sliding is not possible when the glacier is frozen to its bed (Benn and Evans, 2010). There are two types of basal sliding, without and with cavitation (Benn and Evans, 2010). Sliding without cavitation occurs when ice deforms around an object and creeps closed immediately, while cavities remain open and allow for the storage of water in sliding with cavitation (Benn and Evans, 2010). Sliding is increased when cavities are present due to the water content reducing the roughness and stress at the ice-bed interface (Benn and Evans, 2010). In addition to this, basal sliding can be enhanced by the driving stress caused by pressurized water flowing down glacier at the bed (Benn and Evans, 2010). Finally, soft bed deformation also occurs on glaciers that are close to the melting

point at their base, with soft beds deforming under lower stress more easily than those made up of harder materials (Benn and Evans, 2010).

Flow regime (FR) mapping is the classification of patterns of co-variability between the amount which ice thickness and local driving stress affect surface velocities and is used to infer which flow processes (i.e. ice creep, basal sliding or bed deformation) are likely to be dominant at particular areas of a glacier (Burgess et al., 2005). This relationship varies spatially from the ice cap interior to the terminus of outlet glaciers (Boon et al., 2010). There are four FR classifications, in FR1 the glacier is frozen to the bed and surface velocities are affected by internal deformation alone (Boon et al., 2010), with no lateral constraint from bedrock topography (Burgess et al., 2005). Basal sliding begins to contribute to flow in addition to internal deformation in FR2 due to meltwater penetrating to the glacier bed (Boon et al., 2010). FR2 usually occurs over bedrock steps, which indicates that there is a contribution from subglacial topography (Burgess et al., 2005). Increased influence of basal sliding occurs in FR3, likely as a result of increased meltwater penetration to the bed (Boon et al., 2010). This is the flow regime in which we would expect to see seasonal velocity variability due to the melt season providing additional water inputs. Lastly, basal sliding is a dominant contributor in FR4, occurring commonly in areas of the glacier below sea level (Boon et al., 2010; Burgess et al., 2005). Generally, this means that in FR4 there is low friction occurring at the ice-bed interface, which suggests that the glacier is underlain by deformable sediments (Burgess et al., 2005). FR tends to transition at the head of a glacier where there is a change of thermal condition or increased driving stress due to the channeling of ice into narrow bedrock valleys (Burgess et al., 2005). Figure 2-5 shows the FR map for DIC presented in Van Wychen et al., (2017). The ice cap interior is classified as FR1 (which indicates that it is frozen to the bed), and transitions into FR2 (indicating that basal ice is approaching the pressure-melting point) at the point where glaciers enter narrow valleys (Van Wychen et al., 2017). FR3 (indicates reduction in ice viscosity and greater basal contribution to ice motion) appears at the near terminus region of Belcher and Fitzroy Glaciers, and along the valleys of East-7 and SCB Glacier (Van Wychen et al., 2017). Finally, FR4 (high basal motion and deformation of basal sediments) occurs at the terminus of Sverdrup, Belcher, Fitzroy, East-6, East-7, Southeast-3, and SCB Glaciers.

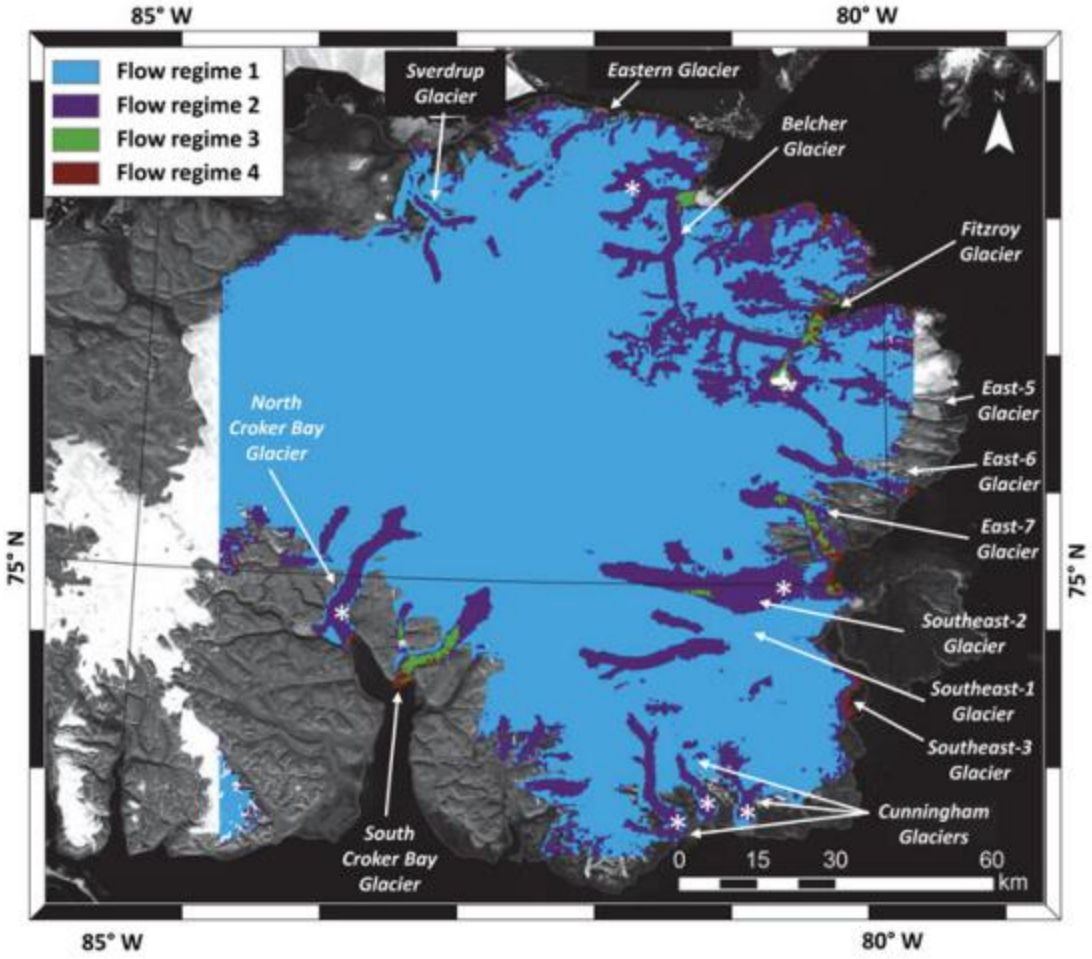

Figure 2-5. Flow regime map of DIC on a Landsat-7 mosaic (Van Wychen et al., 2017)

2.2.2 Multi-annual variations in ice flow observed in the Canadian Arctic

It is generally described that there are three processes driving velocity variability in the CAA (Van Wychen et al., 2016). These processes are 'glacier surging', 'glacier pulsing', and 'consistent acceleration' (Van Wychen et al., 2016). Surging glaciers have two distinct phases between which they cycle; the active phase during which there is rapid acceleration and terminus advance, and the subsequent quiescent phase during which ice flow is lower than the balance flux (Benn and Evans, 2010). Within surge-type glaciers, there is further distinction based on the duration of the active and quiescent phases, which is used to infer the mechanism that initiates the surge phase (Benn and Evans, 2010). Alaskan-type surging glaciers have shorter cycles with active phases which last 1-4 years and quiescent phases lasting 34-40 years (Van Wychen et al., 2016).

Alaskan-type surging ends concurrently with large glacial outburst floods, which indicates that the surge may be initiated by increasing water pressures in a linked-cavity subglacial drainage system (Van Wychen et al., 2016). The second type is Svalbard-type surge glaciers, which experience longer cycles with active phases lasting 7-15 years and quiescent phases lasting 50-100 years (Van Wychen et al., 2016). Svalbard-type surges terminate over a period of multiple years, which suggests that the surge is related to the thermal conditions at the bed rather than subglacial water pressure (Van Wychen et al., 2016). Glaciers in the CAA have been hypothesized to be more like Svalbard-type glaciers due to their longer active phases (Van Wychen et al., 2016; Copland et al., 2003). More generally, an active surge is associated with high velocities initiating up glacier propagating downstream along the entire length of the glacier, terminus advance during the active phase and retreat during the quiescent phase (Van Wychen et al., 2016).

In a pulsing cycle, there is a multi-year speed up followed by a multi-year slow down, with the terminus advancing during speed up and retreating during slowdown, which is a similar pattern expected of glacier surging (Van Wychen et al., 2016). However, for pulse events, velocity variability is not transmitted the same way as in a surge. Rather, the increased velocity is initiated in the near terminus region and is restricted to areas of the bed below sea level (Van Wychen et al., 2016). There has been evidence on other glaciers in the CAA that ice thickens at locations of bedrock sills which causes the surface to steepen and increase flow rates which can result in a pulse (Van Wychen et al., 2016). To highlight the difference between surging and pulsing, the main divergence is that in a pulse all velocity variability initiates in the near terminus region and propagates up glacier from the lowermost sections, largely being restricted to regions of the bed below sea level (Van Wychen et al., 2016). Finally, consistent acceleration has been identified as velocities which fairly continuously increase, associated with terminus retreat and thinning (Van Wychen et al., 2016; 2020). This is different than other patterns and behaviours of dynamic instabilities which have been identified in the CAA and is suggested to be driven by changing atmospheric conditions and bed topography (Van Wychen et al., 2016; Dalton et al., 2022).

2.3 Drivers and controls of seasonal variability of glacier motion

2.3.1 Seasonality description

Glaciers were first identified to flow at varying speeds on varying time scales (from hours to months to years) in the 1930s (Thomson & Copland, 2017). Iken (1974) highlighted three different kinds of glacier velocity variation in their work: short-period, medium-interval, annual and seasonal fluctuations. Short period variations are attributed to the relationship between glacier velocities and the incoming water supply (Iken, 1974). Medium-interval variations take into consideration the lag between run-off entering the hydrological system and velocity peaks at the beginning of the melt season (discussed further in Section 2.3.2 Glacier hydrology and melt induced flow variability; Iken, 1974). Current documentation and understanding of seasonal velocity variation are limited by remote sensing technologies and in-situ data collection capabilities (Boon et al., 2010), and one of the only studies to explore seasonality on DIC identified a clear seasonal signal using in situ methods (Danielson and Sharp, 2013). Danielson and Sharp (2013) identified that both seasonal and diurnal fluctuations in velocities were correlated with lake drainage events and temperature variations. This provides a basis for exploring the seasonality of glaciers and studying their seasonal signals. Velocity increases have been identified using only remote sensing imagery during the summer months for other large glaciers in the CAA (Eugenie, Antoinette, Lake Tuborg, and d'Iberville Glaciers) with rates of ice motion up to eight times greater than their winter baseline (Williamson et al., 2008). There has also been evidence that land-terminating glaciers have peak summer velocities 400% greater than their winter velocities in the CAA (Williamson et al., 2008; Iken 1972). There are two main reasons as to why velocities are lower in the fall and winter compared to the spring and summer seasons, these include:

1. the presence of sea ice acting as a buttressing force along the terminus (Van Wychen et al., 2012);
2. and reduced, or absence of, melt water production during the winter and fall, and without this hydraulic stimulus the glacier flows at slower speeds (Pimentel et al., 2017; Danielson and Sharp, 2013).

Given that the delivery of water to the glacier bed is a key driver of seasonality in the Canadian Arctic (Bingham et al., 2006; Copland et al., 2003; Danielson & Sharp, 2013), the following section will provide an overview of the glacier hydrological system.

2.3.2 Glacier hydrology and melt induced flow variability

The glacier hydrological system has four components: the supraglacial, englacial, subglacial drainage networks, and proglacial run off (Figure 2-6; Benn and Evans, 2010). For the purposes of this study, there will be a focus on the first three of these systems, as the proglacial system is difficult to measure in tidewater terminating glaciers. Inputs to the hydrological network come from the melt of snow and ice, melt at the glacier bed, rainfall, runoff, and groundwater (Benn and Evans, 2010). For the supraglacial portion of the system specifically, the main inputs are rainfall and meltwater which are routed into and through the englacial system to the subglacial system. The subglacial system is also contributed to by groundwater and melt at the glacier bed (Benn and Evans, 2010). The contributions of each of these inputs are affected by the climate, energy balance of the glacier surface and bed, time of day, and the season (Benn and Evans, 2010).

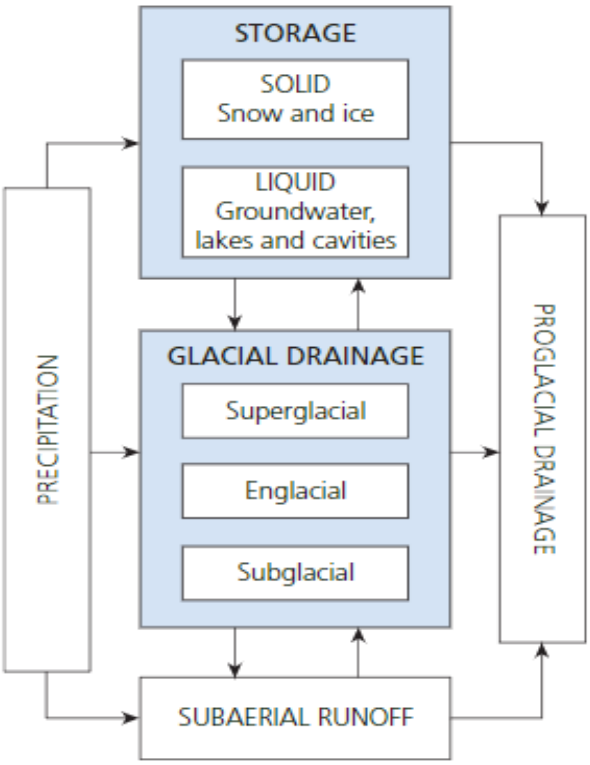

Figure 2-6. Glacier hydrological system schematic (Benn & Evans, 2010)

The supraglacial network refers to the storage and flow of water on the glacier surface (Benn and Evans, 2010). Water can be stored in the supraglacial network in ponds and lakes, which

form in topographic depressions (Sundal et al., 2009; Harcourt et al., 2020). These features expand and grow as the melt season progresses, eventually draining over the course of days to weeks (Benn and Evans, 2010). Lake drainage events have been linked to increases in glacier surface velocities via basal lubrication, as seen by Danielson and Sharp (2013) on Belcher Glacier, where glacier velocities increased from 219 m a^{-1} at the beginning of the acceleration period to 580 m a^{-1} at the peak of the acceleration period (the acceleration period refers to the period in which lakes on the glacier begin to drain), with an overall velocity increase of 5.1% (Danielson & Sharp, 2013). Besides lake drainage events, meltwater can be routed into moulins or crevasses from the supraglacial network into the englacial network, where water can be stored or flow through the glacier (Figure 2-7; Benn and Evans, 2010).

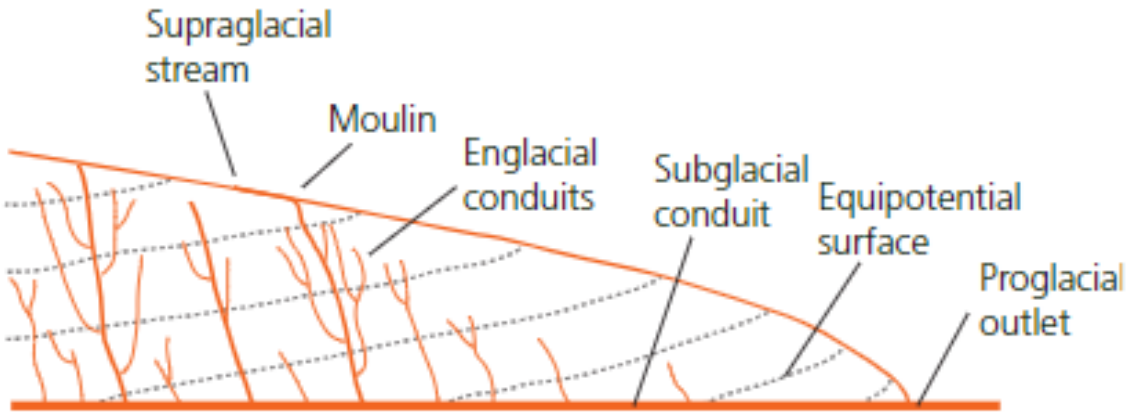

Figure 2-7. Glacier hydrological network features (Modified from Benn & Evans, 2010)

The third component of the glacial hydrological network is the subglacial network, which is the storage and flow of water along or within a glacier bed (Benn and Evans, 2010). This system can be further differentiated based on two main configurations: efficient and inefficient systems. When the system is efficient at moving water through the glacier, it is a channelized system; and when the system is inefficient at doing this it is a distributed system (Benn and Evans, 2010). Networks can evolve from distributed to channelized over time, and vice versa. Efficient system development is usually initiated near the terminus, evolving up-glacier as time progresses. The amount of meltwater that enters the bed of the glacier, which in turn impacts the amount of basal

sliding, depends on how efficient the subglacial hydrological network is (Thomson & Copland, 2017). This affects ice dynamics, as they are influenced by the hydrological system within the glacier. For example, Pimentel and others (2017) found that peak velocities (~450 m a^{-1}) on Belcher Glacier initiated 10 days prior to peak runoff production in their study period in 2009, slowly returning to baseline velocities (~150 to 200 m a^{-1}) during peak runoff production. This is an example of a hydrological switch occurring from an inefficient to efficient drainage network and impacting glacier flow rates (Pimentel et al., 2017).

Findings from Danielson and Sharp (2013) on Belcher Glacier can be used to illustrate the relationship between the supraglacial, englacial, subglacial drainage network, and lake drainage events on glacier velocity spikes. Velocity spikes were correlated with meltwater production, which was caused by increased temperatures, as well as increased water inputs to the hydrological network from lake drainage events (Danielson & Sharp, 2013). Increased water inputs create conditions favourable for the initiation of basal sliding (Danielson & Sharp, 2013). The glacier is likely underlain by marine sediments (Dowdeswell et al., 2004), which is an important consideration as it is a deformable sediment and more vulnerable to the penetration of meltwater, contributing to conditions which facilitate increased surface velocities (Williamson et al., 2008). The high rates of ice discharge from this glacier are due to the high rate of ice flux, which is caused predominantly by rapid velocities rather than terminus retreat (Burgess et al., 2005; Danielson & Sharp, 2013).

2.3.3 Sea ice and mélange conditions

The main drainage of the ice caps in the QEI is facilitated through tidewater terminating glaciers (Sharp et al., 2014), which makes the ice-ocean interface an important consideration. Faster-flowing glaciers are more vulnerable to terminus conditions at the ice-ocean interface than their slower counterparts, which makes this interface specifically important for SCB Glacier (Carr et al., 2013). The main factor that will be investigated in this study for the ocean-ice interface is sea ice buttressing, but generally reduced sea ice cover can have many effects, some of which include altering the thermal regime of the ice, increased open water causing increased precipitation, and higher glacier equilibrium lines (Strozzi et al., 2017). This is an important consideration because there has been an 8.6% decrease of sea ice extent during the summer

months, along with a 50% thinner ice presence at the end of the melt season since the 1960s in the Central Arctic (Dalton et al., 2019). Glaciers are suggested to be stabilized by the presence of landfast sea ice, where the ice acts as a barrier between the glacier front and ocean waters (Figure 2-8A; Carr et al., 2013). Presently sea ice is breaking up earlier and more frequently than it has been historically (Carr et al., 2013). This has implications for increased seasonal calving, as well as reducing the duration of ice presence in areas which had previously experienced year-round landfast ice (Carr et al., 2013).

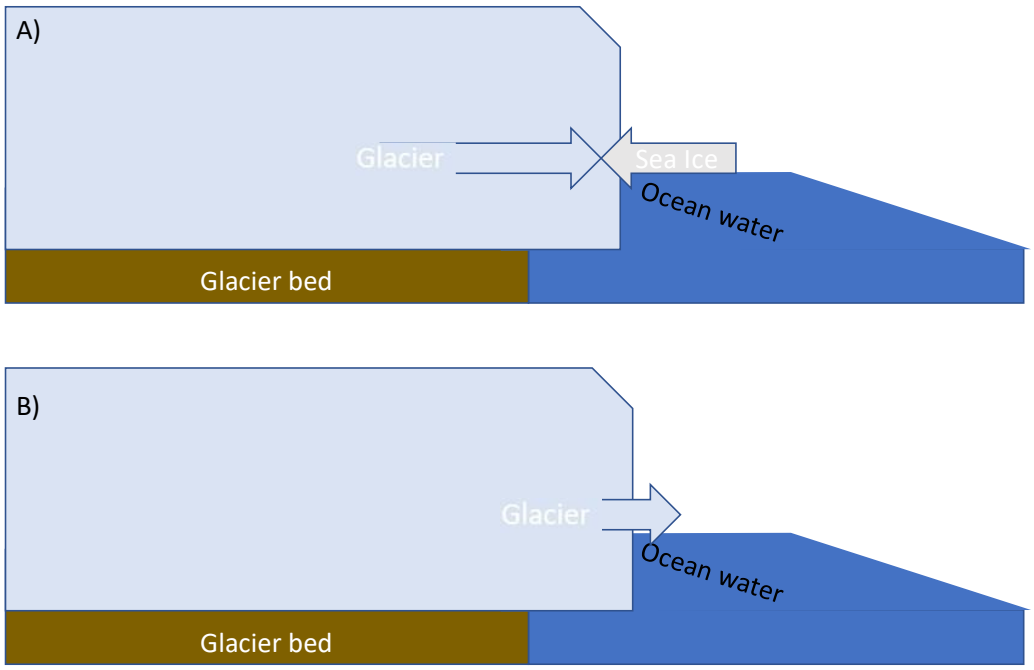

Figure 2-8. A) Glacier with sea ice buttressing at the terminus, B) Glacier without sea ice buttressing at the terminus

Pimentel and others (2017) modelled interannual dynamics for Belcher Glacier specifically including estimated backstress provided by sea ice at the terminus, which was found to not be able to produce the velocity increase that was observed on the glacier. When investigated further, it was found by Herdes and others (2012) that the breakup of landfast sea ice occurred well into the melt season when velocities were already increasing, but the weakening of the ice mélange may be consistent with the acceleration events of the glacier (Pimentel et al., 2017). It should also be noted that velocities return to baseline before landfast sea ice is re-formed at the terminus of Belcher

Glacier, again indicating a weak contribution to the seasonal velocity pattern (Pimentel et al., 2017). However, there is evidence that sea ice does resist the forward pressure during the winter months, as seen in the concentric-folds and longitudinal fractures which appear in the ice during the spring season (Pimentel et al., 2017). As such, the progressive weakening of the mélange may be a contributing factor to the velocity speed up near the terminus of the glacier, but not a driving factor (Pimentel et al., 2017).

2.3.4 Bed topography as a control on flow variability

The underlying topography of a glacier also acts as a control on its flow, with areas of faster flow and highest velocity variability generally located in troughs and areas where the bed descends below sea level in the underlying topography (Dowdeswell et al., 2004; Van Wychen et al., 2017). Bed topography affects velocity through two different bedrock-topographic setting mechanisms (Dowdeswell et al., 2004). One of these settings is when there is a bedrock step which causes down glacier acceleration to occur, and this same mechanism can stop accelerated velocities initiated at the terminus from propagating up glacier (Dowdeswell et al., 2004). The latter example can be seen on SCB Glacier, where ~18 km up glacier from the terminus there is a "pinning point" that prevents faster velocities from penetrating further into the ice cap (Dowdeswell et al., 2004). The second mechanism is when there is a continual decrease in elevation as the glacier moves toward the ablation zone, and faster velocities can be further encouraged by narrow valley walls (Dowdeswell et al., 2004). An example of this can be seen on Belcher Glacier, where the lowermost 10 km experience the largest amount of seasonal variability, with the bed descending below sea level. Generally, where there is available bed elevation and velocity data, interannual variability is seen downglacier of the bed descending below sea level, with little to no variability upglacier from this point, such as what is observed on Dobbin, Trinity, Parrish, Wykeham, Antoinette, Tuborg, Eugenie, and Ekblaw Glaciers (Van Wychen et al., 2016).

Glacier beds which descend below sea level cause the greatest amount of variability as a result of a few factors. Due to their elevation, it is suggested that they are more likely to be made up of marine till, which is more easily deformed and displaced than bedrock (Dowdeswell et al., 2004). These areas are also more susceptible to meltwater access, especially when crevasses are present (Wyatt & Sharp, 2015). In combination with easily deformable underlying sediment, this

increase of water inputs to the subglacial drainage system allows for more uniformly high velocity variability across the glacier. Although this has not been identified on SCB Glacier, tidewater termini below sea level allow for increased incursions of warm water, which can lead to terminus flotation (Wyatt & Sharp, 2015).

2.3.5 Terminus behaviour

Terminus positions can provide insights as to the dynamic processes occurring at specific glaciers. Variability in velocity can be identified in terminus position change depending on the process associated with the variability (Van Wychen et al., 2016; 2020). For example, as previously discussed, terminus position varies with surge and pulse cycles due to increased velocities and the conveyance of mass downglacier (Van Wychen et al., 2016). Logically then, it follows that terminus position can also reflect mass balance conditions of a glacier (Medrzycka et al., 2019). Examples of surge related terminus change have been observed in the CAA, such as on Milne Glacier which advanced and retreated 4 km during its surge and subsequent quiescent phase (Van Wychen et al., 2020). Besides surge and pulse dynamics, there are terminus position changes associated with oscillations in the tidewater glacier cycle (Van Wychen et al., 2020). This cycle has a retreat phase which is initiated when the lowermost terminus region experiences increased flow which begins to thin the upstream ice (Van Wychen et al., 2016). This in turn reduces the effective pressure at the bed, providing less resistance and contributing to faster velocities (Van Wychen et al., 2016). As such, this pulls more mass towards the terminus, allowing for terminus advance. An example of this can be seen on Parrish Glacier, which advanced coincident with a period of faster flow localized to the terminus (Van Wychen et al., 2016). This advance then turned into retreating once the terminus velocities reduced to stagnation, indicating that it became overextended during increased velocities and was not able to replenish mass once they slowed (Van Wychen et al., 2016).

2.3.6 Trends in the Velocity Structure CAA Glaciers

Within Devon, Axel Heiberg, and Ellesmere Islands 51 surge type glaciers have been identified (Van Wychen et al., 2016). From 1999 to 2015, 101 out of 117 glaciers in the CAA that

Van Wychen and others (2016) studied exhibited no significant velocity variability, with only the remaining 16 having velocity changes which exceeded the margin of error (Van Wychen et al., 2016). Seven of these 16 glaciers with significant changes were associated with a slowing of velocity, which mostly occurred on large tidewater terminating glaciers in no specific spatial pattern (Van Wychen et al., 2016). Bidirectional velocity variation was detected on six glaciers, and velocity increases were identified on two glaciers out of 117 (Van Wychen et al., 2016).

Chapter 3 - Methodology

This chapter provides an overview of the datasets and methodologies used to determine the velocity structure of SCB glacier over the study period along with a description of the auxiliary datasets used in the analysis. Remote sensing datasets and methodologies were primarily used in this study due to the remoteness of the study area as well as the availability of spatio-temporally dense time series of TerraSAR-X (TSX) and TanDEM-X (TDX) Synthetic Aperture RADAR (SAR) data which has been collected over SCB Glacier. This TSX/TDX data provides the foundation of velocity mapping which has been done for this study and was utilized with the supplemental use of Sentinel-2 (S2), Landsat-8/9 (L8/9), and NASA's Operation IceBridge (OIB) data products. Specifics about each data type and how it was used is elaborated on in the following subsections, but generally they were utilized in the following ways:

- Velocity maps were derived from high resolution TSX/TDX Stripmap imagery for South Croker Bay Glacier for 11-day periods continuously from January 2015 to October 2021;
- TSX/TDX data acquired over SCB Glacier was used for terminus position delineation;
- Sentinel-2 and Landsat-7/8 imagery for surface melt and surface lake identification; and
- Operation IceBridge MCoRDs data to explore the underlying bed topography of SCB.

3.1 Datasets and Processing Methods

Remotely sensed data can be acquired in different portions of the electromagnetic radiation spectrum depending on the sensor, which in this study was primarily Synthetic Aperture RADAR (discussed further in Section 3.1.1 Synthetic Aperture R). A combination of GAMMA InSAR and ArcMap software packages were used to prepare and analyze the data to explore glacier dynamic variability (discussed further in Section 3.2 Processing Methods). Table 3-1 below outlines additional details pertaining to the resolution, band, repeat pass, and number of scenes used in this study for each sensor. Importantly, it should be noted that the TSX/TDX data has been obtained through an agreement with DLR (German Aerospace courtesy of Anna Wendleder). The remaining datasets that were utilized are all freely available through open repositories (Landsat 8/9, Sentinel-2, Operation IceBridge).

Table 3-1. Major remote sensing datasets utilized in this study including a description of their important characteristics (sensor resolution and repeat pass, number of scenes, date range).

Mission	Wavelength (λ)	Polarization	Product Type	Resolution	Repeat Pass	# of scenes	Date Range
TerraSAR-X	X (3.8-2.4 cm)	HH/VV	StripMap	1.2 m x 3.3 m	11 days	468	2015 to 2021
TanDEM-X	X (3.8-2.4 cm)	HH/VV	StripMap	1.2 m x 3.3 m	11 days	265	2015 to 2021
Landsat 8/9	0.43-12.52 µm	N/A	Earth Observation	50 m	16 days	170	2015 to 2021
Sentinel-2	0.44-2.20 µm	N/A	Top-of-Atmosphere	50 m	5 days	23	2017 to 2018
Sentinel-2	0.44-2.20 µm	N/A	Bottom-of-Atmosphere	50 m	5 days	121	2018 to 2021
Operation IceBridge	180-210 MHz		MCoRDS L2 Ice Thickness	13 m	Ad hoc data collection	1	2011
Operation IceBridge	180-210 MHz		MCoRDS L2 Ice Thickness	30 m	Ad hoc data collection	1	2012

3.1.1 Synthetic Aperture Radar

SAR is a type of RADAR which uses the forward motion of the imaging platform to simulate a "larger" antenna to increase the swath and resolution of the product (Dingle-Robertson et al., 2021). RADAR is an active sensor (emits its own EMR), which can acquire data in conditions that would not be favourable for some passive sensors. The wavelength of the sensor allows for data to be acquired during day or night and in all-weather conditions, with the exception of some potential additional noise from weather related interference (Alaskan Satellite Facility, n.d. ; Dingle-Robertson et al., 2021). These characteristics become valuable in polar regions which are frequently cloud covered and experience 'polar night'. Dry snow can also be penetrated at these wavelengths, which is a benefit to applying this sensor to the study of glaciers (Alaskan Satellite Facility, n.d.).

RADAR was originally named as an acronym for its purpose (Radio Detection And Ranging), and functions essentially as a ranging device. Sensors are equipped with a transmitter,

receiver, antenna, and electrical systems to process and record the signals which are being transmitted and received (Government of Canada, 2015). The transmitter generates a sequence of regularly timed short bursts which are focused into a beam ('B' in Figure 3-1) through an antenna. This beam is emitted at an obliquely at a right angle to the direction of sensor travel, where it interacts and is scattered by the target surface. Energy which is scattered and detected by the sensor is called backscatter ('C' in Figure 3-1). The time delay between the transmission and receiving and the intensity of the pulse of energy is recorded by the sensor (Government of Canada, 2015). Backscatter is affected by the surface characteristics of the target, namely surface roughness and moisture content (Dingle-Robertson et al., 2021). Higher values in backscatter are associated with more energy reflected to the sensor, while lower values have less. It is important to note here that moisture, such as melt production on a glacier surface, reduces the backscatter returns and shows up darker on the image of the glacier surface due to the dielectric constant (Dingle-Robertson et al., 2021).

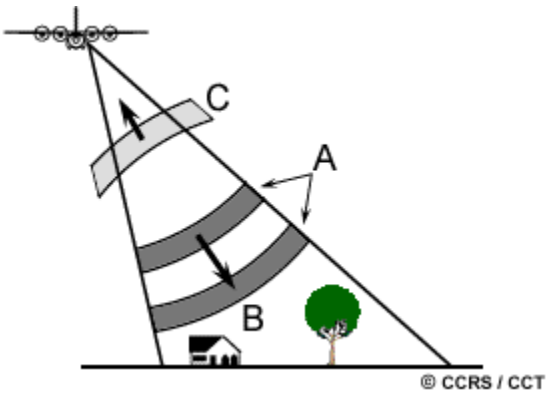

Figure 3-1. Radar energy transmission and receiving (Government of Canada, 2015; https://www.nrcan.gc.ca/sites/www.nrcan.gc.ca/files/earthsciences/images/resource/tutor/fundam/images/radar.gif)

An important consideration when comparing imagery is the geometric distortion that is produced by differing imaging geometries. Changes in flight direction, the direction in which the sensor moves (Figure 3-2A), are the most common when comparing imagery from the same sensor. Microwave sensors transmit EMR at an oblique right angle to the flight direction. The area that is covered by the transmitted EMR is the "swath" ('C' in Figure 3-2) and is offset from the "nadir" ('B' in Figure 3-2), which is the point immediately beneath the sensor (Government of

Canada, 2016). The image is taken within the swath, with the "range" ('D' in Figure 3-2) and "azimuth" ('E' in Figure 3-2) referring to the across-track and along-track dimensions of the acquired image, respectively (Government of Canada, 2016). Range resolution is dependent on the length of the pulse of transmitted EMR, and azimuth resolution is dependent on the angular width and slant range distance. "Slant range" is the line-of-sight distance between the sensor and the target, and azimuth resolution becomes increasingly coarser with distance from the sensor (Government of Canada, 2016). Finally, ground range resolution is how much distance in the slant range corresponds to real world distance (Government of Canada, 2016).

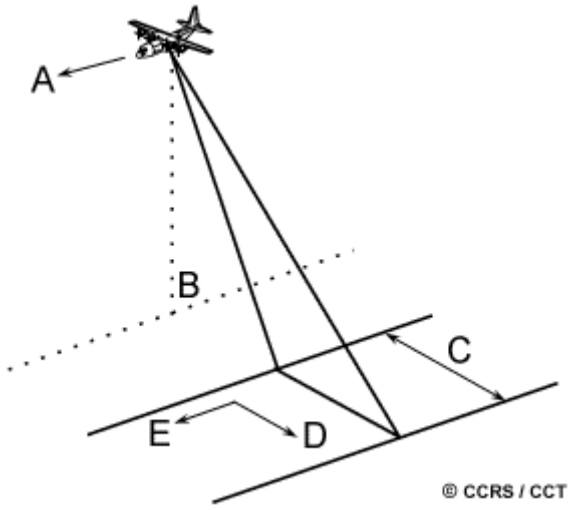

Figure 3-2. Radar imaging geometry diagram (Government of Canada, 2016; https://www.nrcan.gc.ca/sites/www.nrcan.gc.ca/files/earthsciences/images/resource/tutor/fundam/images/radgeom.gif)

SAR operates in the microwave portion of the electromagnetic spectrum, which has wavelengths ranging from 10^{-3} m to 1 m, or frequencies of 0.3 to 40 GHz (Government of Canada, 2015). There are eight main bands, with Ka (0.75 – 1.1 cm), K (1.1 – 1.67 cm), and Ku (1.67 – 2.4 cm) bands being the shortest wavelengths. These bands are uncommonly used today, predominantly being utilized in earlier systems (Government of Canada, 2015). X band (2.4 – 3.75 cm), utilized for TSX/TDX, is commonly used today in terrain mapping applications such as glaciology, as well as for military reconnaissance (Government of Canada, 2015). Then increasing in wavelength there are C (3.75 - 7.5 cm), S (7.5 – 15 cm), L (15 – 30 cm), and P (30 – 100 cm) bands (Government of Canada, 2015). Polarization is important to discuss for microwave energy,

as it refers to the electric field's orientation, which impacts how the energy interacts with the target surface (Government of Canada, 2015). RADAR systems can be single, dual, alternating, or polarimetrically polarized. For the purposes of this work only single and dual polarized data was used. Single polarizations are transmitted and received in the same polarization (also referred to as "like-polarized"), which is either horizontal-horizontal (HH) or vertical-vertical (VV) (Government of Canada, 2015). Dual polarizations are transmitted in one orientation and received in the other (also referred to as "cross-polarized"), which can either be horizontal-vertical (HV) or vertical-horizontal (VH).

3.1.1.1 Radar for Measuring Glacier Motion via Offset Tracking

Methods for measuring glacier motion from SAR imagery have been developed and are well utilized within the glaciological community. The method utilized by this study is "offset tracking", which derives velocities by tracking the displacement of identical speckle chips between two images (discussed further in Section 3.2.1 GAMMA Offset Tracking) (Strozzi et al., 2002). For this process to be successful images must be acquired in the same geometry and the glacier surface must remain relatively consistent to retain coherence (Strozzi et al., 2002). Coherence can be lost as a result of multiple factors, including the accumulation or precipitation of snow on the ice surface, and the melt of either snow/ice causing the EMR to be absorbed by the surface or reflected away from the sensor. Offsets are detected in the slant-range and azimuth directions based on the satellite orbit configurations of the input imagery (Strozzi et al., 2002). Orbit configurations are used to remove the effects of orbital changes so that only glacier specific changes are detected by subtracting the orbital offsets (Strozzi et al., 2002). Here, 11-day separated TSX/TDX imagery acquired on the same orbital path was used to track speckle chip displacements to calculate surface displacement. This approach has been used widely in the field of glaciology and is a common approach to studying glacier dynamics (Strozzi et al., 2002; Van Wychen et al. 2012; 2016; 2020; Short & Gray, 2005). Offset tracking and cross-correlation have been identified as a preferred method as the tuning is less intense than in other methods while yielding good results (Schubert et al., 2013).

3.1.2 TerraSAR-X/TanDEM-X

TSX is a German SAR satellite managed by the German Aerospace Center (DLR) with an 11-day repeat pass (AIRBUS, 2015; European Space Agency, n.d.d). It was launched in 2007, and its twin satellite TanDEM-X (TDX) was launched in 2010 (European Space Agency, n.d.d). Both continue to be operational, with an orbit height of ~514 km at the equator (European Space Agency, n.d.d). The satellites are equipped with an X-band (2.4 – 3.75 cm) radar sensor, which can image in different swaths, resolutions, and in several beam modes, including: Stripmap, Spotlight and ScanSAR modes. Products range from Single Polarization to an experimental QuadPol mode, with products of VV, HH, and VH (European Space Agency, n.d.d). In this study, data acquired in the Stripmap beam mode was used (European Space Agency, n.d.d). The high temporal and spatial resolution of the sensor, combined with the all-weather and daylight imaging capabilities make TSX and TDX highly valuable tools for deriving glacier velocities in remote regions (Schubert et al., 2013).

TSX data has previously been used to track glacier motion in Switzerland and Svalbard (Schubert et al., 2013; Luckman et al., 2015). Previously unutilized data from January 2015 to October 2021 were used to do this for SCB Glacier, which comprised of 336 image pairs acquired in four imaging geometries (Table 3-1). The imaging geometries were: relative orbit 22, orbit cycles 252 and 452; relative orbit 37, orbit cycle 262; and relative orbit 28, orbit cycle 263. Products were processed using offset tracking procedures implemented in the GAMMA InSAR remote sensing software package, which is a common approach in the glaciological community for determining glacier velocities (Schellenberger et al., 2016).

3.2 Processing Methods

3.2.1 GAMMA Offset Tracking

Offset tracking was applied to all acquired TSX/TDX image pairs (Table 3-1) using the GAMMA InSAR software package. The algorithm works on 11-day separated image pairs acquired in the same imaging geometry. Image pairs were manually created and input to the software, where they were converted from their proprietary data format to the generic format used in the GAMMA Software. Then, orbit information found in the metadata of the reference (earlier

dated image) and secondary (later dated image) images was used to co-register the images to ensure they were properly aligned prior to calculating the displacement. Once co-registered, a cross-correlation algorithm was used to search for matching speckle-patterns between the reference and secondary images in user-defined pixel search windows. In this study, window sizes of 512 in azimuth and 256 pixels in range were used (~307 x 1690 m), with a step size of 32 by 16 pixels. For each search window the cross-correlation algorithm found the strongest match between the reference and secondary images and the displacement between them in azimuth and range were derived. The algorithm then calculates the total displacement which is interpreted as glacier surface velocity. For the cross-correlation process to be successful, the target surface needs to have returned similar enough backscatter to the sensor for both images or else coherence is lost between the images, resulting in erroneous displacement calculations.

The final outputs produce a geocoded magnitude GeoTIFF file in the unit of meters per number of days between the reference and secondary image (in this case 11 days). Filtering is not required as the algorithm removes points which do not meet the cross-correlation threshold of 0.1, producing relatively clean velocity maps with little need for post-processing. Figure 3-3 (top) illustrates the GAMMA process.

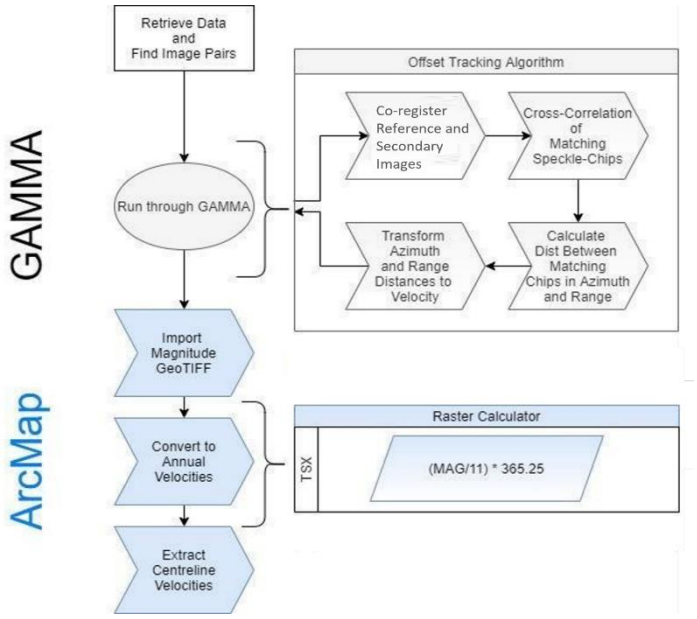

Figure 3-3. Offset tracking data processing workflow

3.2.2 ArcMap

When the offset tracking is complete, the magnitude file for each image pair during the study period was brought into ArcMap 10.8.1 where it was normalized to annual values from 11-day values to assist in direct comparison to the large body of literature (Wyatt & Sharp, 2015; Van Wychen et al., 2012; 2014; 2017; 2020; Millan et al., 2017) using the same units. To calculate annual displacements, values were first converted to daily displacements and then multiplied by 365.25 using the 'Raster Calculator' tool in ArcMap 10.8.1 (Figure 3-3 bottom). Finally, velocities were extracted along the valley centerline. This was done by creating a new shapefile in ArcMap 10.8.1 and manually digitizing a polyline along the centerline using L7 optical imagery (Figure 3-4). This line was then converted to points at 50 m intervals using the 'Edit Features' toolbar, starting with 0 at the terminus. The points were then input to the 'Extract Multi to Point' tool and used to extract velocities from each of the 11-day TSX/TDX pairs. This shapefile was then exported to an Excel sheet for faster manipulation of the data.

Once in Excel, each 11-day pair was labelled with the middle date (six days after the reference date) and averaged together based on the month for each point. This resulted in monthly velocities for SCB Glacier's centerline. Velocities were further grouped into two seasonal averages for the purpose of identifying seasonality, summer (melt season from June to August), and winter (non-melt season, September to May). The percent difference of velocities at the point 4.25 km (highest point up glacier with coherence year-round) from the terminus was calculated in Excel using the following formula:

$$s\Delta = \left(\frac{S_p - S_c}{S_p}\right) \times 100 \qquad (3\text{-}1)$$

where $s\Delta$ is the seasonal change, S_p is the previous seasonal velocity and S_c is the current seasonal velocity.

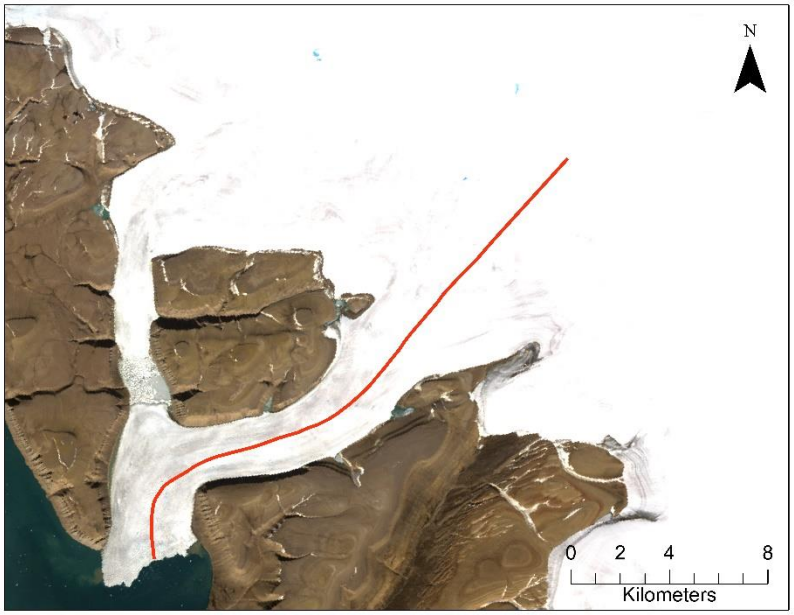

Figure 3-4. Manually digitized SCB Glacier centerline (in red) used to extract glacier velocities from offset tracking products overlaid on an L7 image of SCB Glacier overlaid on a Landsat-7 image of Devon Ice Cap

3.3 Error Analysis of TSX/TDX Derived Glacier Velocity Products

Due to slight problems in the image co-registration process and mismatches that occur in the cross-correlation algorithm (where the algorithm erroneously finds a stronger match between incorrect pixels) errors are introduced into the results (Van Wychen et al., 2012). When coherence is lost between images erroneous pixel matches occur more commonly, in addition to blank spots where no matches could be found (Van Wychen et al., 2012). Quantifying the error and uncertainty of glacier velocities is therefore important in identifying whether real change has been detected on the surface. It is generally accepted that offset tracking has an associated margin of error of ~20 m a^{-1} (Van Wychen et al., 2012), but this can be fine-tuned for individual results by measuring displacements over areas of known zero-motion, such as bedrock outcrops (Schellenberger et al., 2016; Van Wychen et al., 2012). Once the margin of error is identified, velocity variability that exceeds this threshold is considered to be real. Where in-situ data is available, additional methods of quantifying uncertainty are possible, such as validating remotely-sensed velocities against dGPS records (Rohner et al., 2019). While there are no in-situ velocity data for SCB Glacier, previous studies have identified good agreement between remotely sensed and GPS recorded velocities, with an R^2 of 0.675 when comparing Sentinel-1 and RADARSAT-2 to GPS records (Figure 3-5; Rohner et al., 2019).

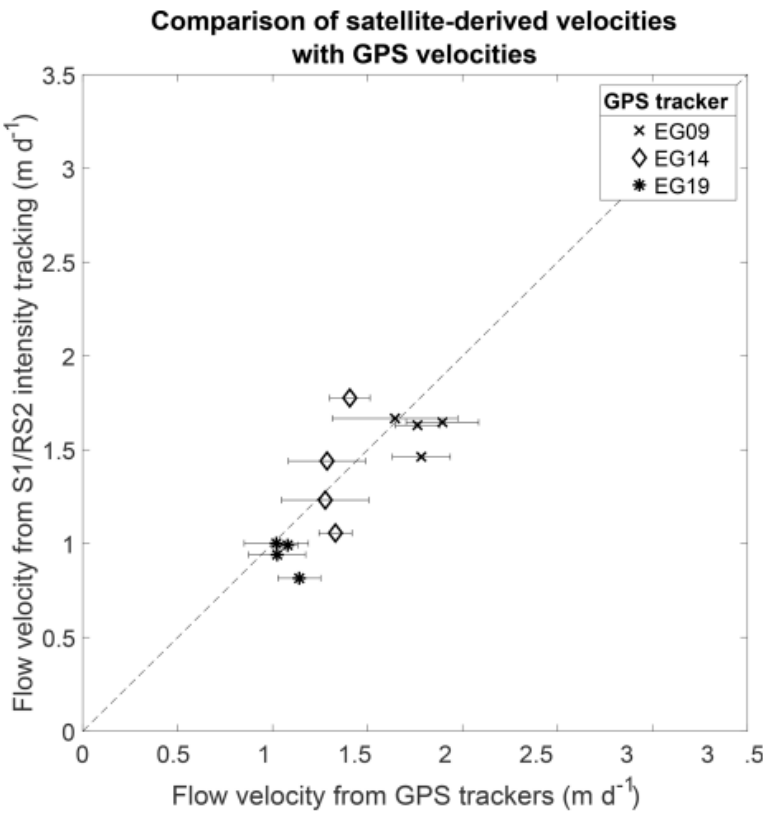

Figure 3-5. S1/R2 velocities plotted against GPS velocities for corresponding periods on the Greenland Ice Sheet, diagonal is where values would be equal, horizontal bars are S1/R2 std, vertical bars are GPS std (Modified from Rohner et al., 2019)

In this study, velocities were extracted over areas of known-zero motion, which were bedrock outcrops in this case. To accomplish this, a box-like polygon was drawn in a new shapefile which covered the area of SCB Glacier, including areas of bedrock. The SCB Glacier basin was selected from the Randolph Glacier Inventory (RGI) (version 6.0, https://www.glims.org/RGI/) and exported as its own shapefile. This shapefile was then used to remove the glacier basin area from the box-like polygon that was drawn with the "Erase" tool in ArcMap 10.8.1 so that the result would be a shapefile containing only bedrock areas within the glacier basin extent. To ensure that influences from the fjord and glacier velocities were removed from the margin of error quantification, a 250 m buffer was created within the bedrock area and erased from the shapefile as well. This ensured that the resulting polygon contained velocities that were purely the result over bedrock.

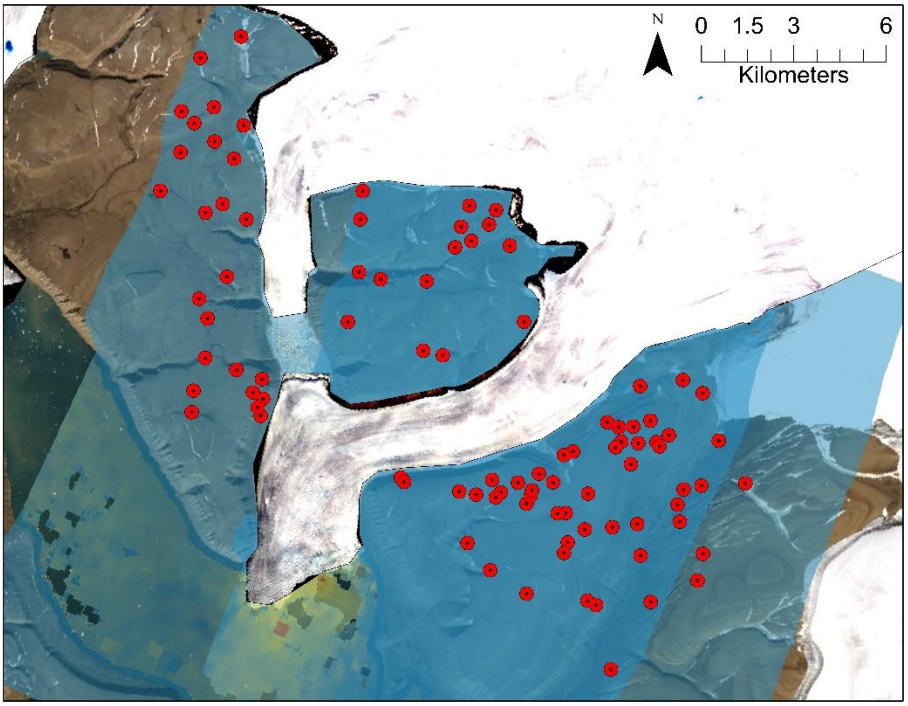

Figure 3-6. Locations of bedrock velocity extracts for uncertainty analysis (red circles), overlaid on velocity map derived over bedrock in SCB Glacier basin overlaid on a velocity map

Using this bedrock shapefile as a constraining polygon, 100 random points were generated with a minimum distance of 3 m between each point using the "Create Random Points" tool in ArcMap 10.8.1 (Figure 3-6). Points generated over gaps in the data were removed, resulting in 96 points. This minimum allowed distance was selected to be the same as the pixel resolution of the input TSX/TDX imagery. These points were then used to extract the velocities derived from each image pair using the "Extract Multi Values to Points" tool in ArcMap 10.8.1, which were then exported to Excel for analysis. The average and standard deviation of the velocities were calculated using built-in Excel functions. VV and HH polarized imagery were separately analyzed for the margin of error to assess whether there was a significant difference between the two and to ensure the two could be compared. The difference was not significant between polarizations, with an average velocity over bedrock of 5.1 m a^{-1} and standard deviation of 11.7 and 6.4 m a^{-1} and 12.7 for VV and HH polarized results, respectively (Table 3-2). Therefore, the error is ~ 5.75 m a^{-1}, with a margin of error of ~ 15 m a^{-1}. As such, variability which exceeds 15 m a^{-1} is considered real, aligning with previous studies which have used this method (Van Wychen et al., 2017; 2020).

Table 3-2. Uncertainty analysis of velocities derived over areas of known zero for VV and HH polarized results

Measurement	VV	HH
Min	0.02	0.01
Mean	5.19	6.47
Max	581.59	496.72
sd	11.78	12.76

3.4 Description of complimentary datasets and methods for investigating variations of ice motion for SCB Glacier

As previously stated in - Study Site and Literature Review, glacier velocity variability may be driven and controlled by a combination of surface melt that penetrates to the glacier bed, sea ice buttressing, and underlying bed topography. Each of these drivers and controls were investigated using complementary data sets discussed in the sections below (Sections 3.4.1 Surface lake delineation to 3.4.5 Bed topography). Each of the drivers and controls described in the following sections were compared against the derived velocity record of SCB Glacier from 2015-2021 to determine if there was a relationship between these variables and the change in ice motion.

3.4.1 Surface lake delineation

Because direct hydrological data was not available for SCB Glacier, surface melt via surface lakes was used as a proxy as it suggests the potential inputs to the hydrological system during the study period. To investigate the annual evolution of surface melt and detect surface lake development and drainage events for each melt season during the study period, Landsat-8/9 (L8/9) and Sentinel-2 (S2) quick looks were downloaded from Sentinel Hub EO (https://apps.sentinel-hub.com/eo-browser/). Each cloud free image that was available during the study period was downloaded (Appendix A). The L8 satellite has been imaging the earth surface since February 2013 with the Operational Land Imager (OLI) and Thermal Infrared Sensor (TRIS) sensors; while L9 was launched in 2021 with OLI-2 and TRIS-2 sensors (Earth Resource Observation and Science Center, 2020). Each satellite has a repeat-pass of 16 days, but the two are offset by 8 days (Earth Resource Observation and Science Center, 2020). Acquired imagery consists of 11 bands with a 30 x 30 m spatial resolution (B1-7, B9-11), and a 15 x 15 m spatial resolution for the panchromatic band (B8) (Earth Resource Observation and Science Center, 2020). For the purposes

of this study 170 scenes were collected from 2015 to 2021. Another 145 scenes were collected from 2017 to 2021 from S2, which is a polar orbiting two-satellite constellation that is 180^{o} out of phase to halve the repeat pass from 10 days to 5 days (European Space Agency, n.d.c). S2 has 13 spectral bands from visible to shortwave infrared, with resolutions from 10 m to 60 m depending on the wavelength (European Space Agency, n.d.b). Quick looks have a resolution of 50 m, which should be noted.

Using this imagery, five annually reoccurring lakes that formed on the surface of SCB Glacier were selected for the study. Each lake was manually digitized using a variable scale in ArcMap 10.8.1 (Figure 3-7). All imagery was projected using a UTM Zone 17N projection to maintain consistency with all other data in the study. The lakes were labelled, and shapefiles were created for each, which were then added to a common geodatabase. Lake area, perimeter, and location were automatically recorded during the digitization process, and the date of the imagery was manually recorded in the attribute table. Both true-colour and false-colour composites were used for visualization during digitization. Once this process was complete the information was exported to Excel where areas were manually converted from m^2 to km^2 and surface lake area was totaled for monthly values using built in Excel functions. If multiple acquisitions were taken on the same day, area values were averaged.

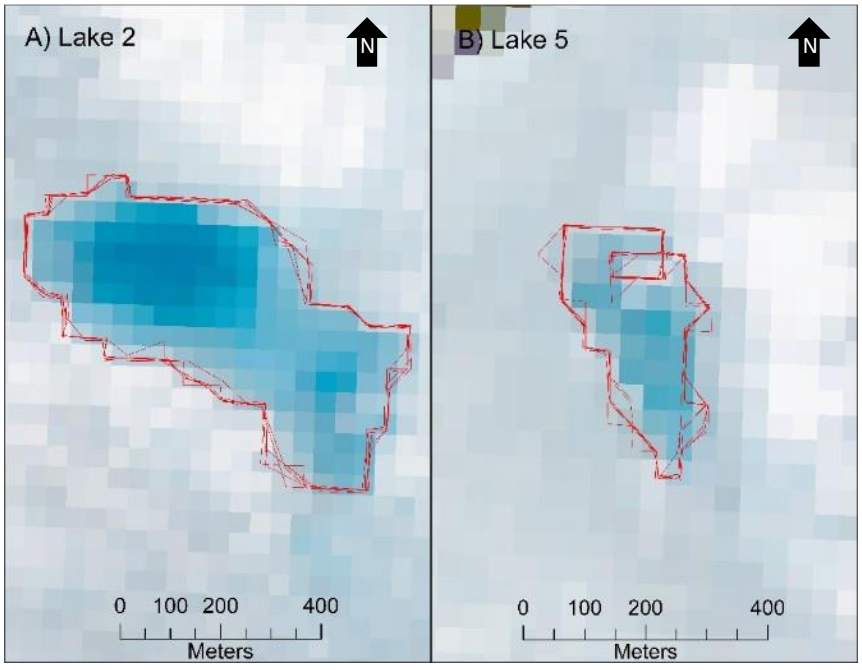

Figure 3-7. Example supraglacial lake delineation in red of lakes 2 and 5 on L8/9 quick looks

This information can be used to assess the intensity of each melt season and track the development of each lake throughout the melt season, with individual drainage events being recorded. Unfortunately, due to the temporal distribution, this data cannot be used to make concrete conclusions, but it does provide contextual information. In addition to the temporal distribution, the margin of error must be considered when using this information. To quantify this, the largest lake (lake 5) and the smallest lake (lake 2) were each manually digitized 5 times to get an estimate of user error (Figure 3-7). It was found that on average the difference was 9%.

3.4.2 SCB Terminus positions

The position of a glacier's terminus informs the processes occurring on a glacier and is useful in identifying potential pulse and/or surge activity. Terminus positions were delineated using TSX/TDX Ground Range Detected (GRD) imagery provided with the SLC data from DLR (previously discussed in Section 3.1.2 TerraSAR-X). GRD products were used in this analysis because they are multi-looked (once in both azimuth and range), which enhances visual clarity by reducing the noise present in SLC products (European Space Agency, n.d.a). Multi-looking reduces the spatial resolution of GRD products, which in this case is 2.4 x 2.4 m. Like the method used for supraglacial lake delineation, the terminus position of SCB Glacier was manually digitized on a variable scale in ArcMap 10.8.1 with the map projection set to UTM Zone 17 N.

A common approach for measuring change in terminus position (Moon and Joughin, 2008; Van Wychen et al., 2022) was adopted for this study, where a box-shaped polygon was drawn around the terminus region to ensure a consistent reference point for measuring advance or retreat. One box was drawn for each imaging geometry and added to a common geodatabase. Each geometry had its own shapefile which was automatically populated with the perimeter (m) and area (m^2) of the terminus, and the date of the image was manually added to the attribute table. The earliest dated acquisition was digitized first, and only positions which deviated from the previous digitization were drawn, producing 170 delineations. Change in terminus position was assessed by comparing the greatest terminus area and the least terminus area. The distance between the two was taken across five evenly spaced points using the 'Measure tool' in ArcMap 10.8.1 in UTM Zone 17N and transcribed in Excel, where they were averaged.

3.4.3 Sea ice buttressing

To understand the effects of sea ice buttressing on velocity variability, sea ice conditions at the terminus of SCB Glacier were recorded throughout the study period. Weekly Regional Ice Charts – WMO Colour of the "Eastern Arctic" (Figure 3-8) were retrieved for each image pair date during the study period from the Government of Canada's Sea Ice Archive: https://iceweb1.cis.ec.gc.ca/Archive/page1.xhtml?lang=en (Environment and Climate Change Canada, 2016). Regional Ice Charts are created by trained meteorologists based on information acquired by satellite imagery, weather, and oceanographic information, as well as in situ observations. Each observed area in the region has an associated "Egg Code" containing sea ice concentrations, which range from open water (> 1) to landfast sea ice (10+) (Figure 3-8). The WMO Colour classifications provide 11 categories for ice conditions, rating the strength and concentration out of 10, as well as information about the ice stage of development and type (Environment and Climate Change Canada, 2016). This information was transcribed into an Excel Sheet for each week for the study period and used to determine the presence or absence of sea ice at SCB Glacier terminus, enabling for the investigation of the timing of sea ice free conditions. With that, velocity variability can be compared against changes in sea ice conditions.

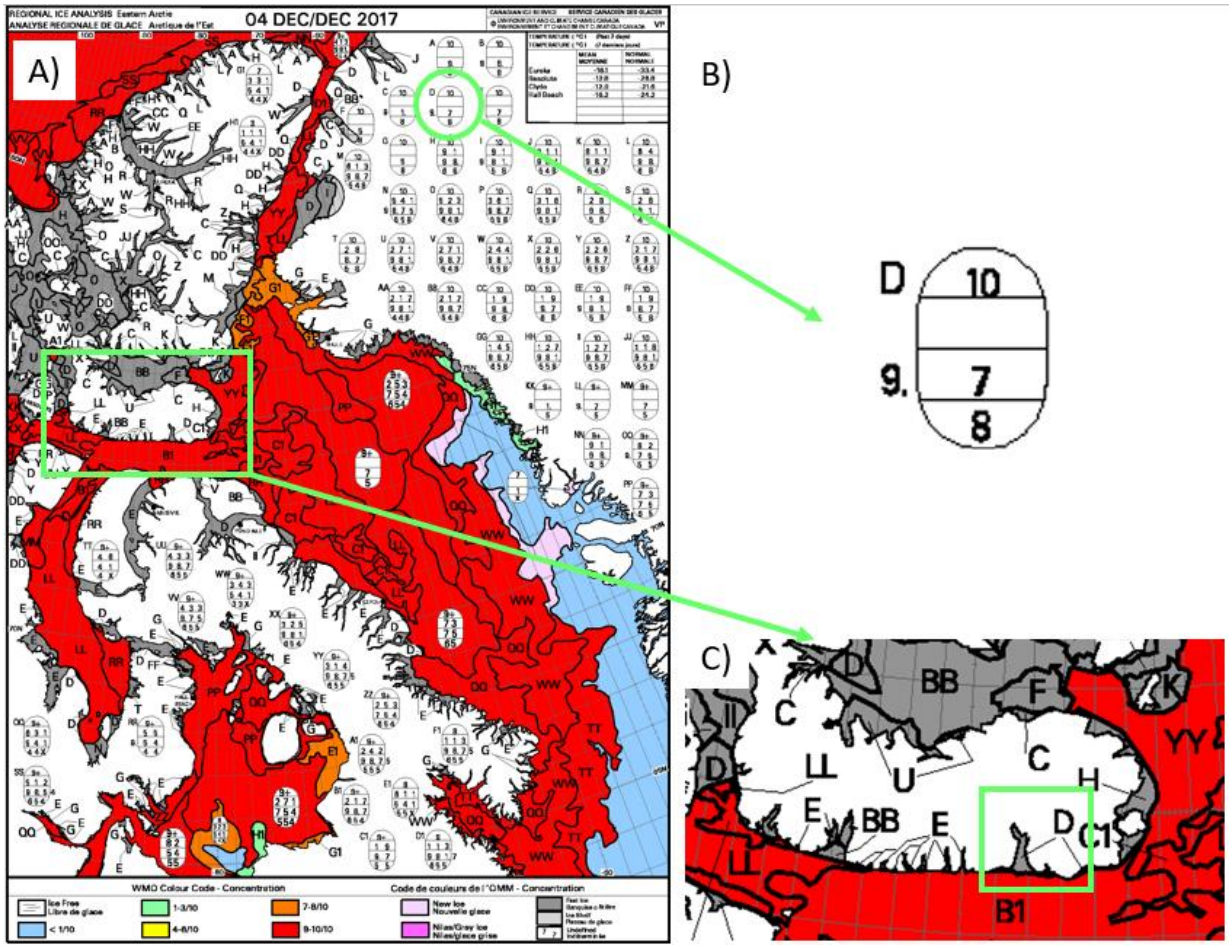

Figure 3-8. A) Canadian Sea Ice Weekly Regional WMO Colour results for the Eastern Arctic, B) EGG code related to Croker Bay Fjord, C) Devon Ice Cap with SCB Glacier annotated on it

3.4.4 Temperature

Air temperature data was used as a proxy for understanding glacier hydrological conditions, as high temperatures produce meltwater and indicate the intensity of the melt season. Two sources of air temperature data were utilized for this study. Primarily, Automated Weather Station (AWS) data was recorded each hour from 2017-01 to 2021-05 on DIC (Danielson, B. Personal Communication). Hourly temperatures were averaged to daily values in Excel and used to calculate the number of Positive Degree Days (PDDs) that occurred each year. Daily averages > 0^{o}C were counted as PDDs (Liu et al., 2021), which were then summed for each month and year. The following equation is used to calculate PDD:

$$\mathrm{PDD} = \sum_{i=1}^{n} T^{+} \qquad (3\text{-}2)$$

where T^{+} is daily temperatures > 0^{o}C per month, and n is the number of days in the month (Liu et al., 2021). Calculating PDDs is a common approach used to compare melt between years and as a proxy for melt water production (Moran & Marshall, 2009; Uszczyk et al., 2019). This information was used to interpret the difference in the intensity of melt occurring between years, and how it affects the velocity dynamics of the glacier.

Average weekly air temperatures are also provided on the Regional Sea Ice Charts (Section 3.4.3 Sea ice buttressing) and this data was used to fill the gaps in AWS coverage. These were transcribed to an Excel Sheet each week from January 2015 to October 2021. This was used as secondary information, as the temperatures are weekly averages recorded at Resolute Bay, which is ~ 343 km to the west of SCB Glacier. As such, this information can only provide an indication of regional climate, but the AWS data is preferred.

3.4.5 Bed topography

To gain an understanding of SCB Glacier's underlying topography, bed elevation data from NASA's Operation IceBridge (OIB) program was retrieved (nsidc.org). The main purpose of the program was to fill in gaps in between the ICESat and ICESat-2 missions (MacGregor et al., 2021). OIB was operational for 13 years from 2009 to 2021, surveying land and sea ice from 15 different aircrafts (MacGregor et al., 2021). The aircrafts were equipped with radar sounders, gravimeters, magnetometers, and cameras (MacGregor et al., 2021). The program allowed for advancements in the understanding of interannual outlet glacier variability and thickness, as well as other snow and ice related knowledge (MacGregor et al., 2021). Two tracks of IceBridge MCoRDS L2 Ice Thickness, Version 1 were obtained. The first tract of data was collected on 05-05-2011 and the second on 04-05-2012. Retrieved data included information about the elevation, surface, bottom, and thickness of the glacier which was obtained using a depth sounder (NSIDC, n.d.). The data was obtained as a .csv file, which was then imported to ArcMap 10.8.1 and visualized using the "Display XY as events" tool and exported as a point shapefile (Figure 3-9). Data was subset to the

extent of SCB glacier basin using the RGI outlines (RGI Consortium, 2017). The 2011 and 2012 data were acquired with differing parameters, and as such they differ slightly in point spacing, with the former having 13 m between points and the latter 30 m. The general uncertainty of the bed elevation data is estimated at 10 to 20 m (Medrzycka et al., 2019).

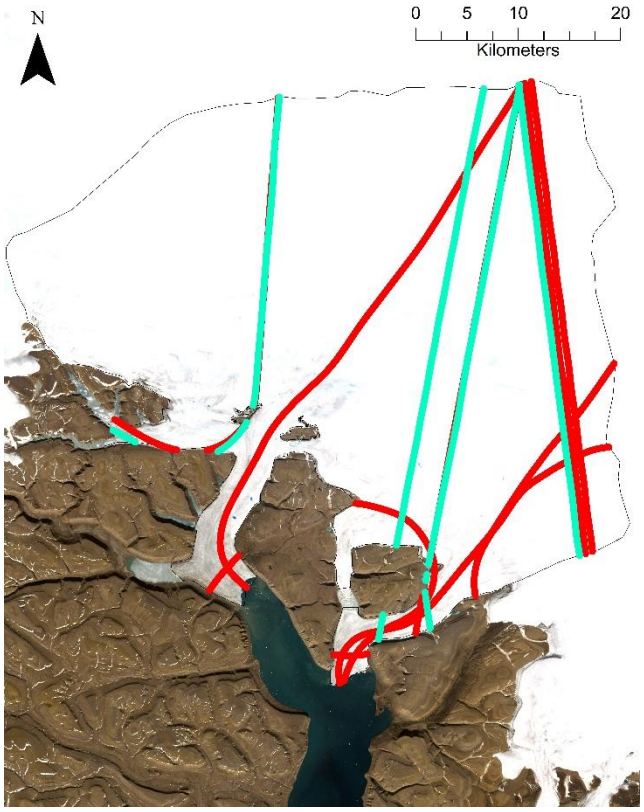

Figure 3-9. Ice thickness data flight lines over SCB Basin with 2011-05-05 in green and 2012-05-04 in red

To assess whether basal topography controls glacier surface velocities, the OIB points were used as an input to the "Extract Multi Value to Point" tool along with each of the velocity results in ArcMap 10.8.1 with the UTM Zone 17N coordinate system. These points, now containing velocity information, were then exported to Excel where monthly velocity averages were calculated using built in functions. Standard deviations of the velocities were calculated in ArcMap 10.8.1 using the "Cell Statistics" tool. This analysis was restricted to the near terminus region of the glacier (up to ~4.5 km) due to data loss in the summer months to prevent winter variability bias up-glacier. This, combined with the OIB topography data was used to assess the potential control of bed topography on surface velocity variability.

3.4.6 Complementary data summary

Combined, these datasets have constructed one of the densest records of ice motion that has been derived for any glacier in the CAA. This was used to assess the seasonal and multi-annual velocity variability of SCB Glacier from 2015 to 2021, as well as the potential drivers of the seasonality. The main data source and all complementary data sets except for sea ice and air temperature are remote sensing based, which also allowed us to assess the feasibility of using remote sensing methods for the detection and investigation of seasonality on a high arctic glacier.

Chapter 4 - Seasonal and Multi-year Variability of Ice Dynamics of South Croker Bay Glacier, Devon Ice Cap, Canadian Arctic from 2015 to 2021

Abstract

South Croker Bay Glacier is the third fastest flowing glacier on Devon Ice Cap, Nunavut, Canada, which has exhibited a large degree of multi-annual velocity variability over the last few decades. This variability does not align with the processes identified on other glaciers in the Canadian Arctic Archipelago, such as surging, pulsing or continuous acceleration. To further understand the processes occurring on South Croker Bay Glacier, a dense record of TerraSAR-X imagery was processed using offset tracking to derive continuous velocities every 11 days from January 2015 to October 2021. Glacier hydrology, sea ice buttressing, and bed topography were investigated as potential drivers and controls of the observed variability. Glacier hydrology was inferred using surface air temperature data and surface lake area. To assess how the variability differs from surging and/or pulsing, terminus positions were delineated throughout the study period. Results demonstrate a seasonal signal in glacier velocities, with acceleration occurring from June to August, peaking in July. On average, melt-season velocities were 49.8% faster than non-melt-season velocities. Sea ice remained landfast until July, suggesting that the observed seasonality is not a product of sea ice buttressing. Multi-annually, non-melt season velocities remained relatively consistent until 2018/19, when velocities increased 28% from the previous winter and remained elevated for the remainder of the study period. It was concluded that this was not the result of a surge or pulse, as the terminus position did not advance or retreat > 250 m, indicating the observed change in position was attributed to seasonal fluctuations alone. Instead, the velocity variability is suggested to be caused by the surface mass balance conditions of the previous season influencing the hydrological network, constrained by bed topography.

4.1 Introduction and Study Area

One of the more extensively studied ice caps in the Canadian Arctic Archipelago (CAA), Devon Ice Cap (DIC) covers ~14,400 km^2 of the eastern portion of Devon Island, Nunavut, Canada (Figure 4-1a; Burgess and Sharp, 2004; Van Wychen et al., 2017). Mass balance (MB) measurements of the ice cap were initiated in the 1960s and have been continued as part of a long-

term glacier monitoring program run by Natural Resources Canada (Burgess, 2017). Ice thickness is greatest at the head of eastward flowing basins, with the highest elevation of 1921 m a.s.l. at the summit (Burgess and Sharp, 2004). The interior of the ice cap is likely frozen to the bed with velocities < 20 m a^{-1} (Dowdeswell et al., 2004; Shepherd et al., 2007; Danielson and Sharp, 2013; Van Wychen et al., 2012; 2017; 2020), while the fastest velocities are located on tidewater terminating glaciers, flowing ~ >150 m a^{-1} (Dowdeswell et al., 2004; Van Wychen et al., 2017). One of the faster flowing glaciers on DIC, South Croker Bay (SCB) Glacier, is located in the southwestern quadrant of the ice cap (Burgess et al., 2005; Figure 4-1a). From 1999 to 2010, SCB Glacier has typically flowed 120 – 180 m a^{-1} in the lowermost 20 km, with the exception of 2005/2006 when velocities reached ~240 m a^{-1} (Van Wychen et al., 2017). The initiation of faster flow along the glacier valley coincides with a bedrock bump located ~20 km from the terminus, and maximum velocities are found within the near terminus region which is grounded below sea level until ~10 km from the calving front (Van Wychen et al., 2017). Ice thickness reduces with proximity to the terminus, with a minimum thickness of ~125 m found in the near terminus region and a maximum of ~596 m in the accumulation area (Van Wychen et al., 2017).

Preceding studies have noted that SCB Glacier seems to undergo flow variability on multi-annual time scales, with higher velocities (> 200 m a^{-1}) initiating in 2018/19 (Van Wychen et al., 2020). This velocity variability is not well aligned with classifications suggested by previous work in the CAA, which have mostly been explained by glacier surge or pulse processes (Van Wychen et al., 2016; 2017; 2020; 2021), or by external factors such as climatically driven thinning and acceleration (Dalton et al., 2022). Surge-type glaciers exhibit cyclical fluctuations in velocity from a short "surge" of accelerated velocities lasting months to years (typically initiating up glacier and then propagating to the near terminus region), to a "quiescent" phase of near stagnant velocities lasting from decades to centuries (Sharp, 1988). Pulse-type cycles are characterized by regions of the glacier which descend below sea level experiencing either years of deceleration or acceleration (initiating in the near terminus region and restricted to only areas below sea level) (Van Wychen et al., 2016). Neither previously derived annual or winter velocities indicate that SCB Glacier experiences a quiescent phase such as what is expected to occur in a surge, nor are the accelerations restricted to areas below sea level such as in pulse-type glaciers. Instead, there has been considerable variability in the velocity pattern with no identified stagnation, propagating from the near terminus region up-glacier into areas where the bed is above sea level, and periods of velocity

variability having no consistent time between acceleration and decelerations (Van Wychen et al., 2017). Given this, the study of the multi-annual variability occurring at SCB Glacier warrants further investigation.

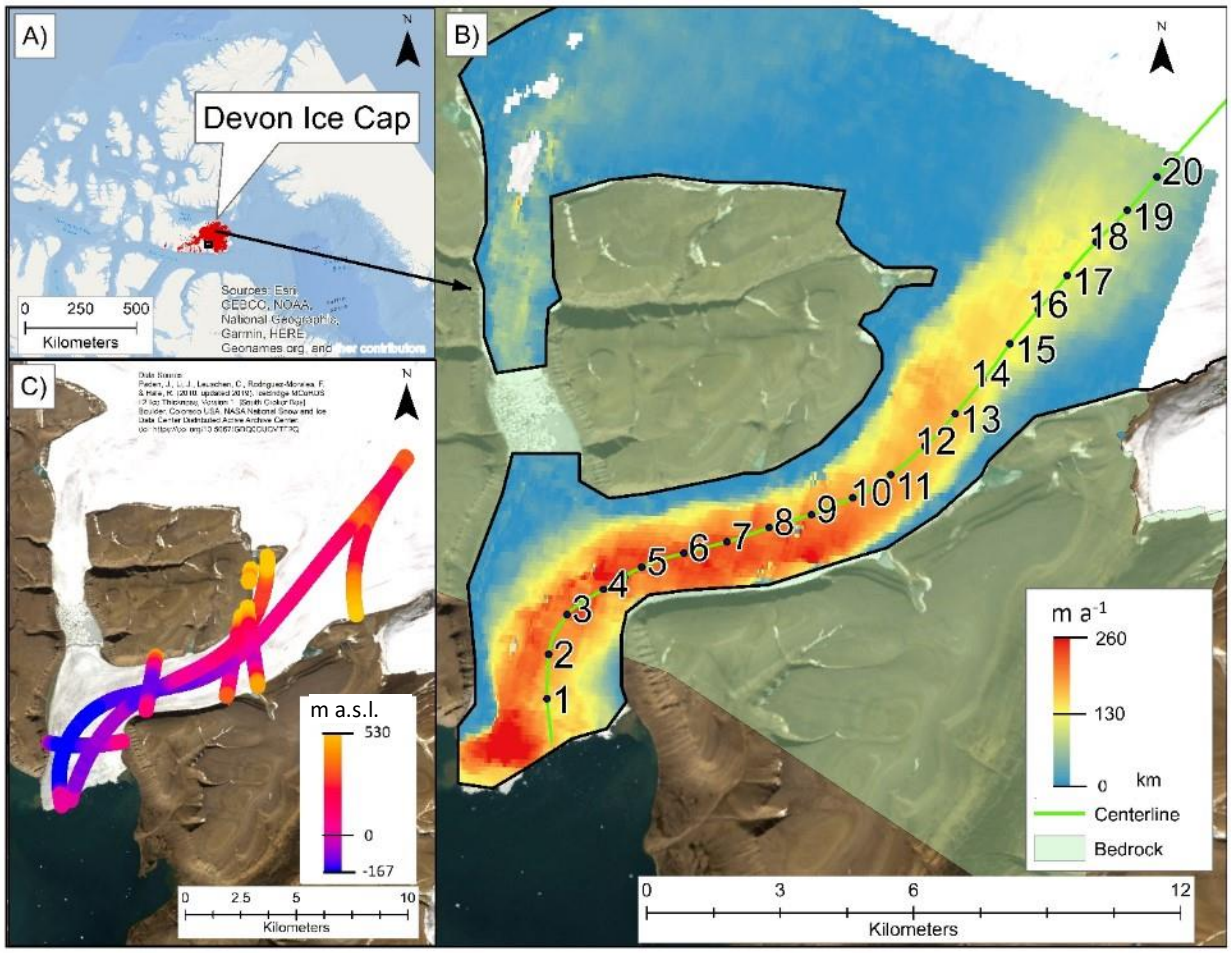

Figure 4-1. A) The location of Devon Ice Cap within the Canadian Arctic Archipelago; B) location of the North and South Croker Bay Glacier basin on Devon Ice Cap with km from centerline; C) bed elevations of South Croker Bay Glacier determined from 3D tomography data collected by NASA's Operation IceBridge program (05/05/2011 and 05/04/2012).

In addition to multi-annual variations in ice flow, seasonal variations in ice motion for SCB Glacier have also been identified (Van Wychen et al., 2017). This was done by comparing velocity results of one image pair during the winter to feature tracking results on annual data (Van Wychen et al., 2017). It is important to note the difference between annual and winter velocities, as higher annual values may indicate the occurrence of a summer speed up. Comparison of annual (feature

tracked) and winter (speckle-tracked) velocity profiles done by Van Wychen and others (2017) identify this discrepancy, where annual values exceeded corresponding winters. Annual velocities in 2009/10 specifically exhibit plug-flow like profiles, where there is uniform flow across the flux gate, while winter velocities are 15% slower along the valley walls. This further indicates the presence of seasonal velocity variability (Van Wychen et al., 2017). The increased temporal density of data available for this study supports further investigation of the variability occurring on SCB Glacier identified by Van Wychen and others (2017).

Seasonal velocity variability is a well-known occurrence in the CAA which was first identified by the pioneering work of Iken (1974). Recent studies have attributed the speed-up of polythermal glaciers in the CAA during the melt season (summer, JJA) to meltwater penetration to the glacier bed facilitating faster ice motion (Schaffer et al., 2017; Bingham et al., 2005; 2006; Williamson et al., 2008; Danielson and Sharp, 2013; Thomson and Copland, 2017). For example, Lake Tuborg and Antionette Glaciers illustrate this process as they progressively increase in velocity throughout the melt season, flowing faster than their annual velocities (an order of magnitude and 60% faster, respectively) (Williamson et al., 2008). Flow regime (FR) mapping can also be used as an indication of where glaciers may experience seasonal velocity variability, as it describes the effect of basal motion, thermal conditions, and meltwater penetration to the bed on surface velocities (Burgess et al., 2005; Van Wychen et al., 2017; Wyatt and Sharp, 2017). Suggesting that the contribution of basal sliding to surface velocities strengthens with proximity to the terminus, the head of SCB Glacier is characterized as FR2 and progressively transitions into FR3 approaching the bedrock bend, moving into FR4 at the terminus (Van Wychen et al., 2017). FR3 and FR4 indicate that seasonality should be widespread on the main trunk of SCB Glacier. The terminus region is highly crevassed and likely underlain by deformable marine sediments, facilitating increased routing of surface and meltwater to the bed (Dowdeswell et al., 2004; Boon et al., 2010). Despite the fact that previous flow regime mapping suggests that seasonality occurs on SCB Glacier and that previous studies have detected seasonality (Van Wychen et al., 2017), the specific knowledge of the seasonal characteristics, such as the amount of speed-up that occurs, over what periods speed-up occurs, and how speed-ups vary between years, remains unresolved.

Given this background, the objective of this study is to characterize and investigate the seasonal and multi-annual variability of ice motion for SCB Glacier at a considerably higher resolution than

has been previously possible. This is enabled by making use of a large catalogue of TerraSAR-X (TSX) and TanDEM-X (TDX) data acquired every 11-days from 2015 to 2021. The specific objectives are to:

1. Quantify the variability of ice motion of SCB Glacier (seasonal and multi-annual variations), a major tidewater terminating glacier on DIC primarily using remote sensing data and methods;
2. Examine the relationship between sea ice conditions, hydrology and glacier bed topography as drivers and controls on the observed variability; and
3. Assess the feasibility of using remote sensing methods to track seasonal changes in glacier motion in the Canadian High Arctic.

4.2 Data and Methods

4.2.1 Offset Tracking

To derive surface ice velocities for SCB Glacier, offset tracking is applied to pairs of TSX/TDX StripMap images, acquired in four imaging geometries. TSX and TDX are German X-band Synthetic Aperture Radar (SAR) systems with an 11-day repeat pass (Eineder et al., 2009). Using SAR data is advantageous because of its ability to image in all weather and illumination conditions, allowing for data to be collected year-round in Arctic environments (McNairn and De Lisle, 2018). This study utilized TSX/TDX scenes collected from 2015 to 2021 provided by the German Aerospace Centre (DLR), which produced 336 image pairs to track glacier velocities. To specifically determine glacier motion from the TSX/TDX data, the Differential Interferometry and Geocoding software module, and GEO and MOCOM packages included in the GAMMA InSAR software were utilized (Wegmüller, 2021). The GAMMA InSAR software is a commonly accepted approach for determining glacier motion and has been used extensively to map ice motion in Arctic regions (Strozzi et al., 2017; Sánchez-Gámez and Navarro, 2017, Luckman et al., 2015). The offset tracking algorithm determines displacements between image pairs acquired on the same orbital path which ensures that the images collected have the same imaging geometries. This study utilizes TSX/TDX Single Look Complex (SLC) products that preserve both pixel amplitude and phase information.

For this process of detecting glacier motion to be successful and not produce erroneous displacement values, the target surface must return similar backscatter to the sensor for both the reference (earlier dated image) and secondary (later dated image) scenes; otherwise, coherence is lost and incorrect displacements are calculated. Coherence is lost when pixels cannot be matched between two images, usually due to a rapidly changing surface. This can be due to snowfall and surface melt, which makes loss of coherence expected during the summer when the glacier surface experiences melt. Areas with prominent surface features, such as crevassing, retain coherence throughout the melt season.

To begin the offset tracking process, the proprietary TSX/TDX data format is converted to the generic GAMMA SLC format. Then the reference and secondary orbit information is read from the metadata products and used to co-register the datasets prior to calculating the displacement. Once co-registered, a cross-correlation algorithm searches the pairs for matching speckle-patterns in user defined pixel search windows and calculates the displacement in both azimuth and range. In this study, window sizes of 256 pixels in range and 512 in azimuth (~ 307 x 1690 m) were used, and the step size was 16 pixels in range and 32 pixels in azimuth. Windows sizes are typically selected to be ~ 250 to 400 m in the CAA for optimal results but are tailored on a case-by-case basis depending on the size and geometry of the glacier (Short and Gray, 2005). The window size chosen for this study was selected through a process of trial and error, using variable window sizes, and comparing the results visually. Total displacement was then calculated (Equation 4-1) using a lookup table derived from the DEM and image parameters from the azimuth and range displacements (Sánchez-Gámez and Navarro, 2017). The equation to calculate the total displacement is:

$$T_d = \sqrt{((d_{az}^2) + (d_r^2))} \qquad (4\text{-}1)$$

where T_d is the total displacement (velocity), d_{az} is displacements in the azimuth direction, and d_r is displacements in the range direction.

In order to correct for potential topographic distortions, convert the velocity values from SAR displacements to ground range displacements and geocode the outputs, the Copernicus 30 m

resolution Digital Elevation Model (GLO-30_DEM) was used (specific DEM tiles utilized were: Copernicus_DSM_10_N74_00_W080_00, Copernicus_DSM_10_N74_00_W081_00, Copernicus_DSM_10_N75_00_W080_00, and Copernicus_DSM_10_N75_00_W081_00 DEM and are available for free download to registered users here: https://panda.copernicus.eu/web/cds-catalogue/panda). This DEM is a Digital Surface Model, representing the Earth surface composed of WorldDEM, and filled in with ASTER, SRTM90, SRTM30, SRTM30plus, GMTED2010, TerraSAR-X Radargrammetric DEM, ALOS World 3D-30m, and Norway National DEM on local scales (European Space Agency, n.d.e). The total calculated displacement between scenes by the GAMMA InSAR processing was then exported as a geocoded GeoTIFF file which represents the total magnitude of displacement between scenes and interpreted as surface velocity. The magnitudes in the resulting GeoTIFFs are in units of meters of displacement per image separation (i.e. the amount of displacement that occurred over the 11-day span of the TSX/TDX images). No post-process filtering was necessary as the GAMMA offset tracking algorithm removes points which do not meet the cross-correlation threshold of 0.1, which produced velocity maps that were largely free of mismatched velocities.

Glacier velocities were extracted from each velocity map along the centerline of SCB Glacier. The centerline was manually drawn using an L7 scene in ArcMap 10.8.1 using UTM Zone 17N (Figure 4-1). Velocities were extracted every 50 m, beginning at the glacier front using the "Extract Multi Values to Point" Tool in ArcMap 10.8.1. The extracted centerline velocities were then brought into Excel and normalized to a common meters per year (m a^{-1}) scale by dividing the value extracted at point along the centerline by the number of days of image separation (11 days for TSX/TDX), then multiplying by 365.25. Meters per year was selected as the normalization as it conforms with the values reported in previous work which allows for ease of comparison with those studies (Van Wychen et al., 2012; 2017; Millan et al., 2017). Finally, velocities for each month were averaged in Excel to create monthly average centerline velocities which were used in this analysis. Image pairs were labelled as the date in the middle of the pair (6 days after the reference date), with pairs spanning two separate months or years separated using this date. As such, if the pair extended further into one month/year than the other, it would be labelled as such. Taking this approach provided velocity results reported along the centerline of SCB glacier up to 19 km from the glacier terminus each year from 2015 to 2021.

To further characterize seasonality across all the velocity data, velocities were extracted at a single point 4.25 km from the terminus (location of this point is shown as a green circle on Figure 4-1b). This point was selected as it is a location where velocities are available in all months throughout the study period. This region is crevassed enough to produce a consistent backscatter pattern which can be tracked reliably using the offset tracking procedure and provide velocity results throughout the entire study period. Upglacier of this location, coherence was lost during the summer months due to changes (melt) in the surface characteristics between image pairs and velocities could not be determined. Finally, when comparing seasonal velocities, the percent difference at the point 4.25 km from the terminus was calculated on the averaged seasonal values, using the following formula:

$$s\Delta = \left(\frac{S_p - S_c}{S_p}\right) \times 100 \qquad (4\text{-}2)$$

where $s\Delta$ is the seasonal change, S_p is the previous seasonal velocity and S_c is the current seasonal velocity. Seasons are defined by the melt season, with "summer" being considered as June, July, and August, and "winter" considered to be the non-melt season from September to May the following year.

Table 4-1. Summary of remote sensing data included in the study

Sensor	Band	Polarization	Imaging Mode	Resolution (range x az)	Repeat Pass	# of scenes	Date Range	Utility
TSX	X /3.8-2.4 cm	HH	StripMap	1.2 x 3.3 m	11 days	149 image pairs	2015 to 2021	Velocity tracking
TSX	X /3.8-2.4 cm	VV	StripMap	1.2 x 3.3 m	11 days	187 image pairs	2015 to 2021	Velocity tracking
TSX	X /3.8-2.4 cm	VV and HH	Ground Range Detected	2.4 x 2.4 m	11 days	468	2015 to 2021	Terminus delineation (orbit cycles 22, 28, 37)
TDX	X /3.8-2.4 cm	VV and HH	StripMap	1.2 x 3.3 m	11 days	265	2015 to 2021	Velocity tracking
L8/9	0.43-12.52 µm	N/A	Earth Observation	50 m	16 days	170	2015 to 2021	Supraglacial lake delineation
S2	0.44-2.20 µm	N/A	Top-Of-Atmosphere	50 m	5 days	23	2017 to 2018	Supraglacial lake delineation
S2	0.44-2.20 µm	N/A	Bottom-Of-Atmosphere	50 m	5 days	121	2018 to 2021	Supraglacial lake delineation
OIB	180-210 MHz		MCoRDS L2 Ice Thickness	2011 = 13 m 2012 = 30 m	1 year	2	2011 and 2012	Underlying bed topography

4.2.2 Glacier Velocity Mapping Uncertainty

Uncertainty of the derived velocity products must be bounded to determine whether the variations observed on SCB Glacier are significant and can be attributed to real glacier change and not simply uncertainty. This is commonly done by quantifying the displacement generated over areas of known zero-motion (ie. bedrock outcrops) (Van Wychen et al., 2016; 2020). To do this, a box-like polygon was drawn covering the area of SCB Glacier and the surrounding bedrock in ArcMap 10.8.1. Then, a glacier outline (shapefile) of SCB provided by version 6.0 of the Randolph Glacier Inventory (RGI; Pfeffer et al., 2017) was used to remove the glacier area from this polygon using the "Erase" tool in ArcMap 10.8.1. This created a new shapefile containing only bedrock areas adjacent to SCB Glacier. Last, a 250 m buffer was removed from this bedrock area to remove any remaining influence of glacier velocities or imperfections in the original outlines.

To calculate error for each derived velocity map, 100 random points were generated within the bedrock polygon, with a minimum distance of 3 m between points to ensure a new pixel is selected each point. Using these points, the velocity for each velocity product was extracted using the "Extract Multi Values to Points" tool and exported to Excel for analysis. The mean velocity over bedrock for VV polarized scenes was 5.1 m a^{-1}, with a standard deviation of 11.7. While for HH the mean and standard deviation were 6.4 m a^{-1} and 12.7, respectively. If the variation identified on the glacier was greater than the margin of error for the method it was considered valid, which to be conservative is a difference of ~ > 15 m a^{-1}, aligning with what has been identified by other studies utilizing this method (Van Wychen et al., 2017; 2021).

4.2.3 Terminus Position Analysis

To track the terminus position of SCB Glacier, four imaging geometries of TSX/TDX Ground Range Detected (GRD) products (provided with the SLC image data) were used to delineate terminus change from 2015 to 2021 (Table 4-1). GRD products were used as they are multi-looked for the reduction of noise, allowing for visual identification (European Space Agency, n.d.a). Using a common approach for measuring terminus position change (Moon and Joughin, 2008; Van Wychen et al., 2022), a box-shaped polygon was drawn around the terminus area for a consistent reference point in measuring any potential advance or retreat for each

geometry. The terminus was then manually digitized in ArcMap 10.8.1 on a variable scale using the UTM Zone 17N coordinate system, using the box to start and end at the digitization's at the same position each time. Each imaging geometry was digitized in its own shapefile and added to a common geodatabase. Area (m^2) and perimeter (m) were automatically calculated with each polygon digitization, and date information was manually added for each delineation. Each TSX/TDX image from the catalogue was considered, digitizing the first image in the collection, then digitizing only the images in which the terminus did not align with the previously digitized terminus position for the same geometry. This resulted in 170 positions (Table 4-2). Because the terminus positions were digitized from the same imagery as the velocity results they coincide temporally and can be used to assess whether terminus position varies with velocity. To assess whether this is the case, the average distance between the greatest and least extent was taken along five points of the terminus using the "Measure" tool in ArcMap 10.8.1.

Table 4-2. Terminus delineation per orbit cycle of South Croker Bay Glacier, 2015-2021

Relative Orbit: Orbit Cycle	Delineations
37:262	79
28:263	19
22:252	38
22:452	14

4.2.4 Terminus Position Uncertainty

Manual digitization, geometric distortion, and image resolution are the primary sources of uncertainty (Moon and Joughin, 2008), as they impact how the terminus is perceived by the digitizer. Since each image had the same image resolution and was geocoded, manual digitization was the greatest factor in terminus position uncertainty. To assess this, the same scene was manually digitized five times in ArcMap 10.8.1 using the UTM 17N projection. Once this was complete, the shapefile was exported to Excel, where the average difference was found to be 1.7%.

4.2.5 Sea Ice and Climate Analysis

To determine the potential impact of sea ice on rates of motion for SCB Glacier, sea ice conditions at the terminus of SCB were assessed using the Weekly Regional Ice Charts for the "Eastern Arctic" from the Government of Canada's Sea Ice Archive (Environment and Climate Change Canada, 2016). Based on satellite imagery, weather and oceanographic information, and in situ observation, weekly coverages provide sea ice conditions and temperature information in the form of an 'egg code' (Environment and Climate Change Canada, 2020). This enabled sea ice conditions for the fjord into which SCB Glacier drains to be tracked over time as an indication of when sea ice forms, weakens, and is no longer present at the terminus. To do this, weekly sea ice conditions were transcribed into an Excel worksheet for the entire study period, recording the concentration from the WMO Colour classes. On a monthly scale however presence or absence was the only consideration. These records of sea ice were then plotted with the derived velocity maps to investigate the connection between variations in glacier flow rates and sea ice conditions. Sea ice presence or absence also provides an indication of the length and intensity of the melt season, as sea ice breaks up earlier during warmer summers and remains intact during colder ones (Tivy et al., 2011). With this information, inferences can be made regarding the degree of melt there might have been on SCB Glacier for interpretation of the effects on velocity.

4.2.6 Positive Degree Days

Positive degree days (PDDs) were considered as a proxy to understand the climatic and hydrologic condition of the glacier. PDDs were calculated from an automated weather station on DIC (Personal Communication, Danielson, B). Data was recorded hourly from 2017-01 to 2021-05. To use this for analysis, hourly temperatures were averaged into daily temperatures and then days with an average temperature > 0^{o}C were counted as PDDs for each month.

4.2.7 Lake Delineation

Five surface lakes on SCB Glacier with the greatest surface area were selected for consideration in this study, all of which reoccured annually in supraglacial depressions. Using

cloud free optical data from L8/9 and S2 obtained from Sentinel Hub EO surface lake extent was delineated from 2015 to 2021 (Table 4-1). Lakes were visually identified using L8/9 and S2 highlight-optimized natural colour composites (Bands 4, 3, 2), and S2 Short Wave Infrared (SWIR) imagery (Bands 12, 8A, and 4). Once identified, they were manually digitized on a variable scale in ArcMap 10.8.1 using the UTM Zone 17N projection. Each lake was labelled and dated during the digitization process in separate shapefiles and added to a common geodatabase. Area (m^2) and perimeter (m) were automatically calculated with each polygon feature digitized. These data were then brought into Excel for analysis, where resulting surface areas were converted from m^2 to km^2. In cases where there were multiple scenes captured on the same day lake areas were averaged together, reducing potential errors from manual digitization.

Due to cloud cover, the only months with viable imagery for analysis were June, July, August, and September. Although sparse, this data likely captures lake evolution during the melt season, as these months correspond with the typical extent of the ablation period for DIC (Danielson and Sharp, 2013). The temporal density of data is an important consideration, as the number of scenes was variable for each month and year, meaning that the true evolution of each lake was not fully captured (Figure 4-2). Most notably, only 2 cloud free images were acquired for 2018, which did not allow for an accurate analysis of conditions during that year. Due to the temporal inconsistency of viable data for this analysis, it can only be used to inform the length of the melt season for each year, as well as the determination of whether variations in ice flow correspond with observed variability of surface area in the imagery.

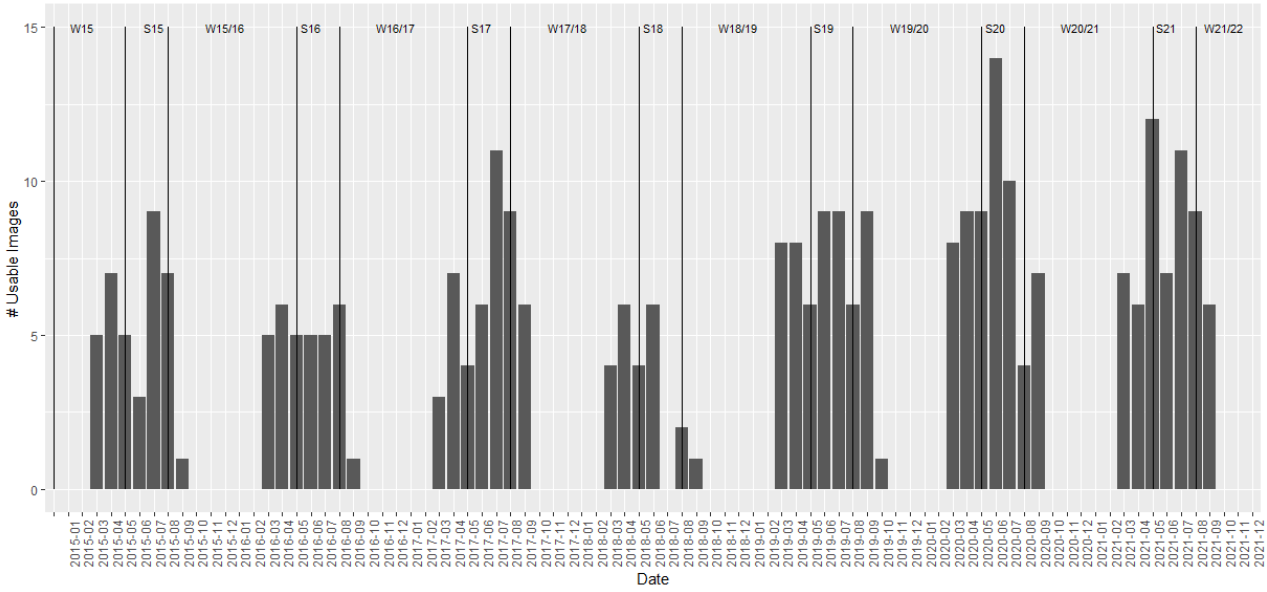

Figure 4-2. Temporal density of L8/9 and S2 scenes for supraglacial lake delineation

4.2.8 Lake Delineation Uncertainty

Like terminus delineation uncertainty, the greatest source of uncertainty in lake delineation is manual digitization, geometric distortion, and image resolution (Moon and Joughin, 2008). To quantify the uncertainty in lake delineation, the smallest and largest lakes were selected for re-digitization, being lake 5 and lake 2 respectively. Each was re-digitized 5 times, and the data was exported to Excel. The mean area of the digitizations was calculated, and the maximum and minimum differences are expressed as a percent error. On average, the area of the digitizations was 9% different.

4.2.9 Bed topography

Glacier bed elevation data was acquired by NASA's Operation Ice Bridge (OIB) program over SCB Glacier on 05-05-2011 and 04-05-2012 and was retrieved from the National Snow & Ice Data Centre, then subset to the study area using the Randolph Glacier Inventory glacier basin outlines (RGI Consortium, 2017). Data was obtained from IceBridge MCoRDS L2 Ice Thickness, Version 1 | National Snow and Ice Data Center (nsidc.org), as a .csv file which was converted into

a point shapefile. This data was collected using a depth sounder which acquires information about the elevation, surface, bottom and thickness of the glacier (NSIDC, n.d.). The data collected in 2011 has a point spacing of 13 m while the 2012 has a spacing of 30 m. This shapefile was then used as an input to the "Extract Multi Value to Point" tool in ArcMap using the UTM 17N coordinate system to extract each velocity product along the glacier, which was then averaged to monthly velocities in Excel. The general uncertainty of the bed elevation data is estimated to be 10 – 20 m (Medrzycka et al., 2019). To investigate whether bed topography influenced glacier velocities, a standard deviation (sd) of velocities was calculated for the near terminus region, up to 4.5 km from the terminus where coherence was maintained throughout the study period to avoid bias introduced by data loss. This was done by inputting each 11-day pair to the "Cell Statistics" Tool in ArcMap 10.8.1, using the standard deviation for the overlay statistic. The area between 1 km and 5 km from the terminus was then extracted.

4.3 Results - Glacier Velocities of SCB Glacier: 2015-2021

4.3.1 General flow structure

The general flow structure of SCB Glacier can be seen in Figure 4-1B, where maximum velocities (> 200 m a^{-1}) were found in the near terminus region and lowermost 12 km. Where the glacier enters the valley from the ice cap velocities reduce to ~ 130 m a^{-1}, slowly transitioning to velocities < 20 m a^{-1} in the interior of the ice cap. There is a small tributary to the west of the main glacier trunk which is disconnected from the terminus by a small lake, with lower velocities of ~100 m a^{-1}. This general flow pattern was spatially and temporally true for all years in the study period. Annually, the highest velocities occur in June, July, and August, when average velocities were observed to be 233 m a^{-1}, which is ~49.8% higher than during other months (Figure 4-3, Table 4-3). Average winter velocities (at 4.25 km from the terminus) throughout the study period were 165 m a^{-1}. Even during the winter, velocities in the near terminus region and lowermost 12 km were highest, reducing < 130 m a^{-1} as the glacier approaches the ice cap interior. The following sections provide a detailed description of both the multi-annual and seasonal variability in ice motion observed over the study period.

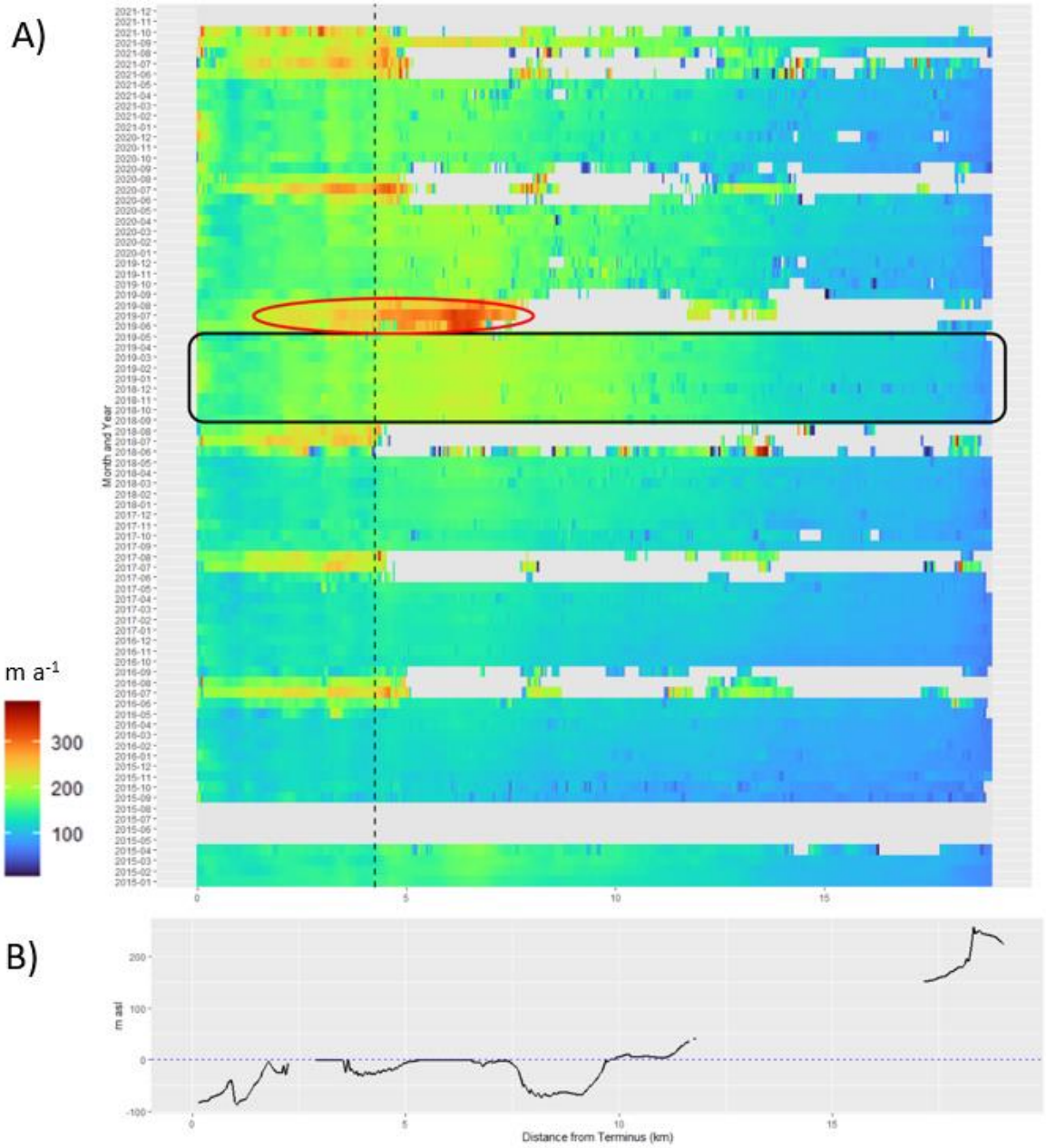

Figure 4-3. A) Average monthly surface ice velocities of SCB Glacier, DIC; from January 2015 to December 2021 derived from offset tracking of TSX/TDX StripMap image pairs. Dashed line at 4.25 km represents the single point used to investigate variations in glacier flow, black box highlights peak winter velocities in 2018/19, and the red ellipse highlights peak summer velocities in 2019 f B) Bed topography along glacier centerline.

4.3.2 Inter-annual velocity variations

Year to year variability of ice motion was apparent on SCB Glacier, which was observed in both summer and winter (Figure 4-3). Average winter velocities ranged between 122 m a^{-1} (in 2015/2016) to 227 m a^{-1} (in 2021), exhibiting a larger range of variability than summer values,

with the greatest change observed between 2017/18 and 2018/19, where winter velocities increased by 28% from 146 m a^{-1} to 189 m a^{-1}. Peak monthly winter velocities occurred in winter 2018/2019 and are annotated with a black box in Figure 4-3. Winter velocities remained elevated after this point, compared to those prior. The fastest recorded summer flow rates occurred immediately following winter 2018/19 (Figure 4-3) with velocities propagating further up glacier (5-7 km from the terminus) than what was observed in other years, although this is difficult to assess fully due to the loss of coherence and consequent missing data in other years. However, due to the crevassing in the near terminus region of SCB Glacier coherence was maintained during the melt season. For the point where there are consistent velocity results (4.25 km from the terminus) data was extracted from all monthly composites, finding a range of summer velocities from 218 m a^{-1} (in 2016) to 243 m a^{-1} (in 2019).

Spatially, the area exhibiting the greatest change in velocity from year to year was located ~2.5 km to ~14 km from the terminus (Figure 4-3). Although this is difficult to assess because coherence was lost after ~4.25 km from the terminus each summer when melt begins to occur. The exception to this is summer 2019 (annotated with the red circle on Figure 4-3) which retains coherence to ~8 km and allows velocities to be determined up to this point reliably only in this year. These results indicate that peak summer velocities for SCB Glacier likely occur within this area, but it was not captured in other summers.

4.3.3 Intra-annual velocity variations

Seasonality was explored at a single point 4.25 km from the terminus where velocities were reliably determined in all months of the study period. While the data loss is disadvantageous, it does provide an indication of where the glacier surface is rapidly changing. As such, it is likely that melt was occurring on the glacier during these months. The largest seasonal acceleration occurred in 2016, with summer average velocities 78.9% higher than the winter average, although it was the slowest summer and winter recorded during the study period (Table 4-3). During this year, flow speeds began increasing in May from ~121 m a^{-1} to ~193 m a^{-1} in June when the melt season begins, peaking in July with speeds of 239 m a^{-1} (Figure 4-4a). Velocities started to reduce slightly in August with values of 220 m a^{-1}, returning to winter baselines in October of 150 m a^{-1} (Figure 4-4a). The second highest seasonal acceleration occurred in 2017, with average summer

velocities (233 m a^{-1}) 64.7% higher than average winter velocities (141 m a^{-1}) (Table 4-3). Peak velocities (281 m a^{-1}) this year occurred in August rather than in July, and peaked sharper than other years as well with velocities steeply declining in September and returning to average winter baselines (147 m a^{-1}) in October (Figure 4-4a).

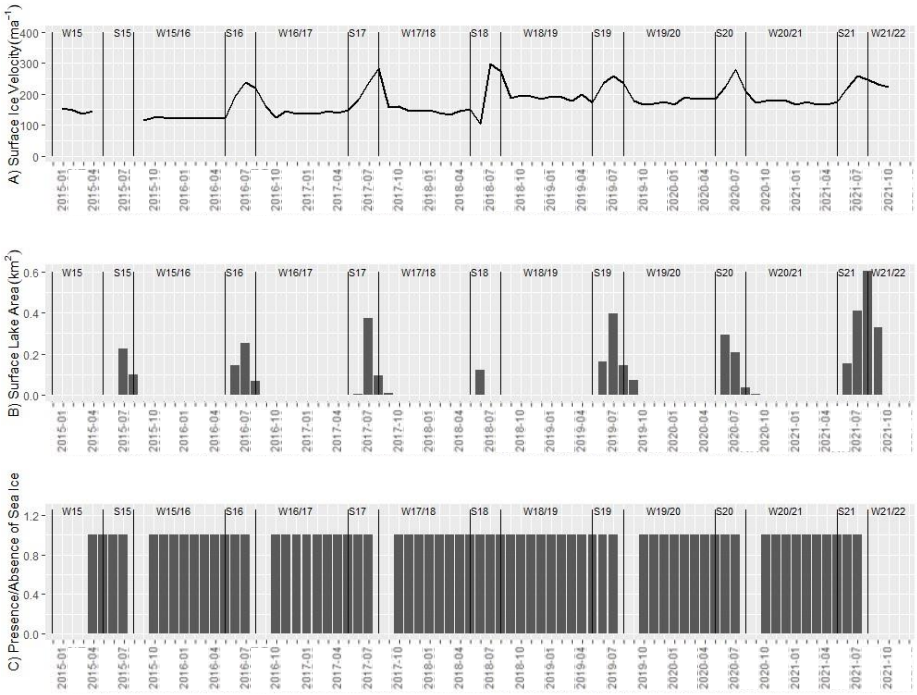

Figure 4-4. A) Average monthly surface velocities of South Croker Bay Glacier extracted at a single location located 4.5 km from the glacier terminus (location indicated with a green circle in figure 3-1b), B) supraglacial lake surface area (km^2) from five sampled lakes on the surface of SCB Glacier, C) Sea ice presence/absence at the SCB terminus.

Summer 2018 stands out compared to other years, as it exhibited a significant dip in velocities in June rather than an increase (Figure 4-4a). Monthly average velocities for June were observed to be 104 m a^{-1}, with the lowermost 3 km of the glacier having slower velocities than other years as well (Figure 4-3). Otherwise, the seasonal signal follows the same pattern as other years, accelerating 53.1% with peak velocities of 297 m a^{-1} in July, decreasing to average winter baselines of 188 m a^{-1} in September (Table 4-3). The winter baselines in 2018/19 were the highest observed in the study period with an average of 189 m a^{-1} (Table 4-3; Figure 4-3). The lowest seasonal acceleration occurred in 2019, with summer average velocities 29.1% higher than winter averages (Table 4-3). Like in the year prior, there is a slight decrease in velocities in June (Figure 4-4a), but

otherwise followed the standard signal, reaching peak velocities of 249 m a^{-1} in July and returning to average non-melt-season baselines of 177 m a^{-1} in September (Table 4-3). In 2020 velocities increased by 33.3% into the summer, with peak velocities of 279 m a^{-1} in July (Table 4-3; Figure 4-4a), decreasing in August more than previous years. Lasting until October, the seasonal signal in 2021 accelerated 39.7% from average winter values, peaking in July with velocities of 258 m a^{-1} (Table 4-3; Figure 4-4a).

Table 4-3. Comparison of winter and summer average seasonal flow speeds, number of ice free weeks, and average seasonal temperatures

Season + Year	# of image pairs	Avg winter flow speed	Avg summer flow speed	Percent difference from previous (%)	# of sea ice free weeks	# of PDDs	# of weeks with lakes present	Avg air temp	Resolute Avg Temp
W2015	18	145			0		0	N/A	-25.8
S2015	7				6		6	N/A	4.1
W2015/16	47	121			6		0	N/A	-20.6
S2016	18		217	78.9	7		9	N/A	2.7
W2016/17	43	141		-35.1	6	0	0	-27.9	-20.1
S2017	8		232	64.7	4	5	8	-5.5	2.2
W2017/18	41	147		-36.7	6	0	4	-25.4	-21.4
S2018	8		225	53.1	2.5	2	1	-6.4	1.1
W2018/19	41	188		-16.4	2	0	0	-25.9	-22.6
S2019	12		243	29.1	7	16	7.5	-3.6	3.2
W2019/20	43	177		-27.0	4	0	2	-26.5	-18.9
S2020	15		237	33.3	6	11	7	-4.1	3.6
W2020/21	46	172		-27.1	6.5	0	1	-23.9	-18.5
S2021	17		241	39.7	5		10	N/A	1.3
W2021	6	226		-6.0	8		3	N/A	1.6
		Avg Summer increase		49.8%					

Generally, velocities were highest in June, July (usually associated with peak velocities), and August throughout the year. On average summer (melt season) velocities were 233 m a^{-1}, which was 49.8% greater than winter (non-melt season) velocities which were 165 m a^{-1} on average. The seasonal signal began in June for all years of the study period, and continued until September (2018, 2019, 2020) or October (2016, 2017, 2021). Velocities in 2018 evolve uniquely compared to other years, with June being anomalously low. Winter values seem to trend upwards, while summer values remained relatively consistent. This is important to consider as it has implications for the reported summer speed up, which looks as though summer velocities were decreasing over time due to greater increases in winter velocities causing the difference to be lower.

4.3.4 Surface Lake Analysis

Figure 4-4b presents the surface area of five supraglacial lakes located on SCB Glacier for the 2015-2021 melt seasons, based on the available optical imagery during the study period (Figure 4-2). On SCB Glacier, supraglacial lakes generally began to form in June, peak in surface area in July, reduce in size in August and disappear in September or October. With the irregular image density retrieved for this study (due to cloud cover), there was no definitive identification of individual lake drainage events coinciding with patterns of velocity variability, however lake extent is still a useful indicator for melt on the glacier and to make broad connections between velocity slowdowns and when lakes generally disappear.

Surface lakes were present in 2015 for 6 weeks from July to August (Table 4-3), reaching maximum extent of 2.0 km^2 in July, then decreasing 80% into August before no longer being detected in the imagery. Lakes persisted 3 weeks longer, from June to August (9 weeks) in 2016 (Table 4-3), peaking in surface area in July (1.2 km^2). In 2017, surface lakes were present for 12 weeks (June to September), suggesting a relatively long melt season that summer. Surface lake area reached a maximum in July, with an extent of 2.9 km^2. Due to cloud cover obstructing the view of the glacier surface, imagery collected in 2018 was sparse and only captured lake presence in June, with no imagery in July when surface area tended to be the greatest in other years presented in this study (Figure 4-2). As such, no information can be reported, but it does suggest that 2018 experienced different climatic conditions than other years in the study period. In 2019, lakes were observed for 9.5 weeks (June to September), with the greatest surface area of 2.7 km^2 observed in July. Following the same pattern, lakes were present for 8 weeks in 2020 (June to September), with the greatest observed extent of 1.6 km^2 occurring in July. The longest period that lakes were observed during the study period occurred in 2021, where they were present for 13 weeks (June to September). It is also notable that the greatest extent occurred in August rather than July, recorded as the highest during the study period at 4.8 km^2.

4.3.5 Sea Ice Analysis

Typically, sea ice was absent at the terminus of SCB Glacier from mid-July to the end of October and present for the remainder of the year (Figure 4-4). Generally, the first two weeks of

July had sea ice present before it dissipated at the end of the month, except for 2017 and 2018 when it dissipated at the beginning of August. When sea ice did dissipate at the terminus it did so abruptly, transitioning from landfast conditions to open water within a weeklong period. August and September experienced sea ice free conditions throughout the study period, aside from 2018. Conditions in 2018 were distinct from other observed years, with sea ice free conditions for only 4.5 weeks of the year (the first 2 weeks of August and the two weeks of September). Ice began to reform at the terminus during the ~second week of October and remained in place until it dissipated again the following year.

The number of sea ice free weeks varied throughout the study period with no clear trend (Table 4-3). In 2015, there were 12 sea ice weeks, which remains relatively consistent into 2016 with 13 (Table 4-3). Ice free weeks then reduced slightly to 10 weeks in 2017, down to the minimum recorded period of 4.5 weeks in 2018. As mentioned previously, conditions were different during 2018 than the rest of the study period, in addition to being significantly shorter, sea ice free periods were not continuous. After this point, ice free conditions returned to previous trends with 11 weeks in 2019, 12.5 weeks in 2020, and 13 weeks in 2021.

4.3.6 Air Temperature Analysis

Annually, temperatures began to increase earlier in the year during the study period, with raising temperatures occurring in April in 2016 and 2017, March in 2015 and 2018, February in 2019 and 2020. In 2021 warming occurred in January, but unfortunately the AWS data did not extend past May, so the entire year was not captured. Based on temperatures at Resolute Bay, seasonal temperatures began to warm consistently in April. As such, generally seasonal temperatures began to increase in April and continued increasing into August, starting to cool again in September. Average monthly temperatures rose to > -9^{o}C from June to August, with temperatures peaking in July (except for 2017, when they peaked in August; Figure 4-5). June, July, and August were the only months during the study period which had PDDs. Temperatures began to cool < -10^{o}C in September. PDDs before 2017 could not be calculated due to the temporal resolution of the Canadian Ice Service data.

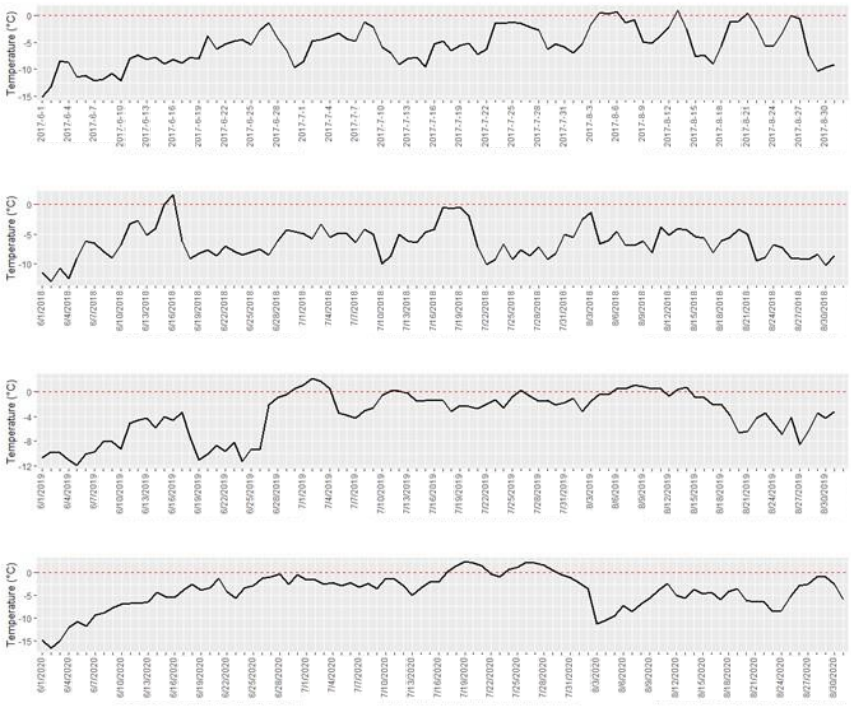

Figure 4-5. Daily averaged SATs, 0 degrees Celsius annotated in red, for 2017 (top), 2018, 2019, and 2020 (bottom)

Figure 4-5 provides the pattern of temperature for each melt season and shows how it varied from 2017 to 2020. In 2017, temperatures were lowest in June and progressively got warmer into August, with periods of colder temperatures scattered throughout. All five PDDs that occurred this year were in August. No clear trend was identified in the temperatures during summer 2018, as averaged daily temperatures peaked in June (when two PDDs occurred), and average monthly temperatures peaked in July. This year however was the coolest melt season on record during the study period, with average temperatures of -6.4^{o}C. Meanwhile in 2019, June had the lowest average monthly temperatures of the melt season (-7.2^{o}C), which remained relatively consistently elevated in July when they peaked at -1.3^{o}C on average and into the end of August, with averages of -2.4^{o}C. This year was on average the warmest melt season recorded during the study period, with an average temperature of -3.6^{o}C and 16 PDDs (1 in June, 7 in July, and 8 in August; Table 4-3). In 2020 the same trend continued with temperatures steadily increasing throughout June, and highest monthly averages in July (-0.8^{o}C). This was the highest monthly average recorded during the study period, with all 11 PDDs contained in July.

4.3.7 Bed Topography of South Croker Bay Glacier

The bed topography of SCB Glacier is spatially variable across the glacier centerline, undulating in short distances. Generally, elevations are greater with increased proximity to the valley walls and accumulation zone and lower along the centerline and in the near terminus region. Because the OIB tracks do not align fully with the centerline of the glacier, gaps in the bed elevation are present in the analysis. The lowermost 2 km of the glacier have the lowest elevation measured across the glacier valley, ranging from -87.7 m a.s.l to -2.4 m a.s.l. Values remain below sea level until ~3.5 km from the terminus where it approaches sea level again (-1.5 m a.s.l.). The bed descends again to -30 m a.s.l from this point up to ~ 4 km from the terminus, approaching sea level again (-1.2 to -7.6 a.s.l.) until ~8 km from the terminus. The western portion of the glacier in the lowermost 5 km descends below sea level to a greater degree than the eastern portion (Figure 4-6). From ~8.5 to 10 km from the terminus there is a steep decline in the bed which plateaus at ~ -70 m a.s.l, forming a bowl like depression, evident in the topography displayed in Figure 4-6. Above ~10 km from the terminus the centerline of the glacier bed rises above sea level, reaching up to 256 m a.s.l in the upper reaches (Figure 4-3). A bedrock bump is located further up glacier at ~ 21 km from the terminus.

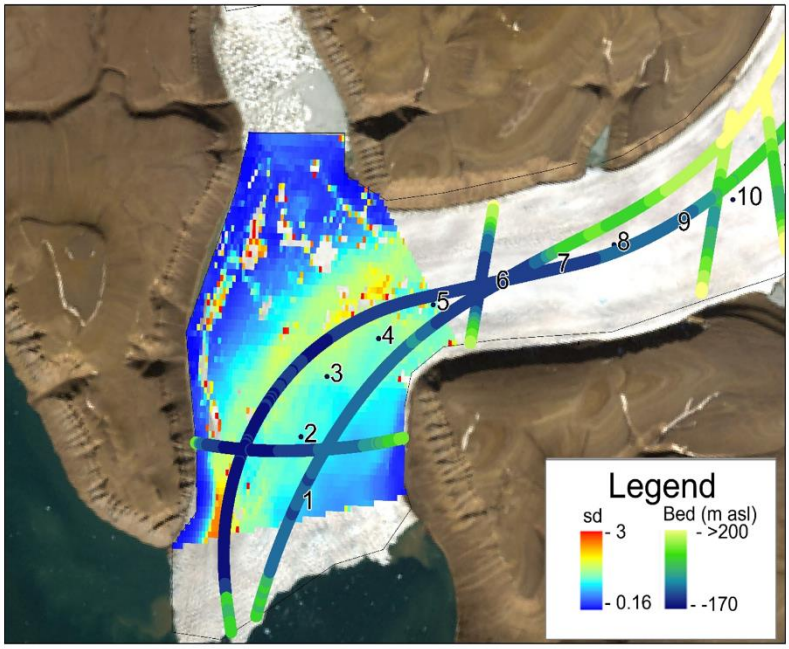

Figure 4-6. Spatial variability of velocities in the near terminus region of SCB with bed elevation

4.3.8 Terminus Position Analysis

Terminus positions throughout the study period were digitized for each available TSX/TDX scene. Because there were four imaging geometries, the geometric distortions varied, and the area of the terminus could not be directly compared (Table 4-2). Instead, the distance between the greatest and least extent was compared for each geometry. Although the date ranges were inconsistent, October had the minimum terminus extent observed in three geometries, one dated in 2020, and the other two in 2021. Maximum terminus extent was inconsistent across each geometry with no apparent pattern identified. The greatest variability in extent was observed in orbit cycle 262, with a difference of 245 m occurring between January 31, 2019 and October 28, 2021; and the lowest was 94.2 m in orbit cycle 452 occurring from July 20, 2021 to October 27, 2021. On average between each minimum and maximum extent, terminus position varied by 180 m, indicating that the glacier front was in a relatively stable position throughout the study period.

Table 4-4. Terminus minimum and maximum extent for each orbit cycle, and the distance between minimum and maximum

Orbit Cycle	Min	Max	Distance (m)
252	10/18/2020	4/15/2015	215.8
262	10/28/2021	1/31/2019	245.4
263	9/2/2016	5/7/2015	166.4
452	10/27/2021	7/20/2021	94.2

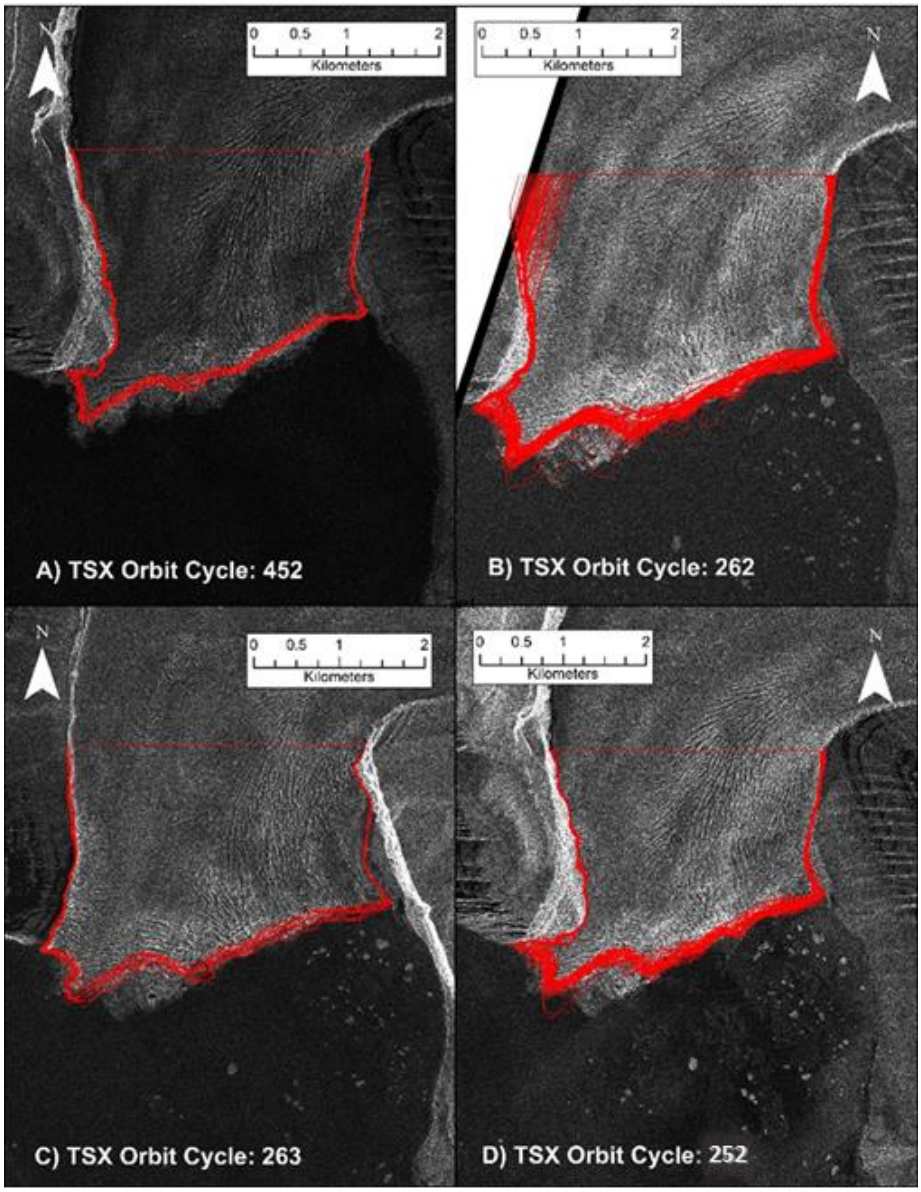

Figure 4-7. Digitized terminus positions from 2015 to 2021 overlaid on TSX imagery, grouped by orbit cycle

4.4 Discussion

The reported results confirm previous observations of SCB Glacier from earlier work (Van Wychen et al., 2017; 2020) but provide velocity records on a finer temporal scale. Previously the glacier was identified as one of the fastest flowing on DIC, with peak winter velocities ranging between 120 m a^{-1} and 200 m a^{-1} in the lowermost 12 km of the glacier from 2015 to 2020 (Millan et al. 2017; Van Wychen et al. 2017; 2020). The previously observed peak winter velocities of 200 m a^{-1} that occurred in 2018/19 were derived using R2 imagery (Van Wychen et al., 2017; 2020)

and were also detected in this study using TSX/TDX data. However, the results provided here indicate that the fast flow in 2018/19 that was observed in previous winters occurred through the entire non-melt-season (October 2018 to May 2019). The results of 11-day tracking on TSX/TDX data have also found that the four winters previous (2015/16 to 2017/18) were in the ~140 m a^{-1} range, accelerating 28% to ~ 189 m a^{-1} in 2018/19. Similarly high velocities of ~ 240 m a^{-1} have been found in the lowermost 20 km in the winter of 2005 (Van Wychen et al., 2017), which indicates that the dynamic pattern of the glacier oscillates between years but without a clear time separation between acceleration and deceleration that would be expected of surging or pulsing. Summer velocities have not been extensively studied for SCB Glacier, but the TSX/TDX data available for this study enabled comprehensive velocity tracking in the summer months. Average summer velocities varied less compared to average winter velocities, ranging from 133 m a^{-1} in 2015 to 196 m a^{-1} in 2019, with velocities not varying outside of the margin of error from one year to the next.

The results presented in this study are more detailed than what has been presented previously (Millan et al., 2017; Van Wychen et al., 2017; 2020) and continue to illustrate that the dynamics of SCB Glacier are unique. The following sections explore the drivers of the observed variability, both multi-year and seasonal variability, using sea ice conditions, hydrology, and bed topography. Temperature and surface lakes are used as indicators for hydrology, as there are no available datasets pertaining to the glacial hydrology for SCB Glacier. In addition to this, the terminus was delineated to gain an understanding of the dynamics of the glacier, as the observed variability did not align well with either surge or pulse processes (Van Wychen et al., 2016; 2020).

4.4.1 Variability in Glacier Flow of SCB Glacier

4.4.1.1 Seasonal variability

Evident in Figure 4-3, an annual seasonal acceleration in flow occurred on SCB glacier each June and lasted until August. This velocity variability was coincident with increased temperatures during the study period (Figure 4-5). Flow rates of SCB Glacier aligned with the progression of the melt season on DIC, which is driven by high surface air temperatures (SATs) occurring from June to August, peaking in July (Figure 4-5). This was generally reflected in the amount of

supraglacial melt stored in lakes as well, which persisted from June to August, and peaked in July. Previous work has correlated the degree of melting with peak velocities (Danielson and Sharp, 2013; Sundal et al., 2011; Copland et al., 2003), which were also coincident with peak temperatures in July throughout the study period. In 2018, peak velocities and temperatures occurred in July. However, the two PDDs which occurred in 2018 were in June, indicating that there may have been a shorter period of more intense melt occurring in the early melt season.

Surface lake area and drainage has previously been shown to be correlated with velocities by Danielson and Sharp (2013) for Belcher Glacier on DIC. The seasonal velocity accelerations observed on Belcher Glacier occurred at the same time as lakes developed and drained, which occurred early in the melt season (Danielson and Sharp, 2013). It was suggested that these acceleration events were the result of meltwater entering an inefficient sub-glacial drainage network (IDN), which in turn contributed to increased basal sliding and accelerated ice flow (Danielson and Sharp, 2013). Although, the same density of data as Danielson and Sharp (2013) was not available for the five lakes selected on SCB Glacier (Figure 4-2), the lake delineation datasets combined with air temperatures were used as a proxy for understanding the evolution of the glacial hydrology of the glacier. Lake area and air temperatures during the study period tended to peak early in the melt season, coincident with the acceleration of SCB Glacier's velocities, suggesting that melt and changes in the glacier's hydrology impact velocities (Figure 4-5). In other areas of the CAA, such as John Evans Glacier (Ellesmere Island), it was found that the first velocity event that occurred for the glacier was one month after the melt season began, which is when the supraglacial and subglacial networks made their initial connection (Copland et al., 2003). This pattern is similar to what was observed for SCB Glacier, with seasonal acceleration occurring within the first two months of each melt season (Figure 4-4).

As such, it follows that meltwater penetration to the bed (via lake drainage events or otherwise) perturbs the subglacial drainage system, contributing to velocity accelerations (Danielson and Sharp, 2013). The surface of SCB Glacier is heavily crevassed and these crevasses likely store and route meltwater to the bed, which can have highly localized effects on velocity acceleration in the terminus region when the underlying drainage network is inefficient (Danielson and Sharp, 2013). This is a widely recognized process for glacier acceleration, which is reflected in the 49% average summer increase in velocities identified on SCB Glacier occurring coincident with the onset of

increased temperatures and supraglacial lake area (Figure 4-5). The same process has been identified on John Evan's Glacier, which experienced a 62% increase in velocity during the melt season (Bingham et al., 2006).

What is likely being captured later in the melt season on SCB Glacier is a switch from an IDN to the efficient drainage network (EDN). A study of John Evans Glacier identified that there was considerable variability in surface velocities across the entire glacier and that these fluctuations corresponded to the configuration of the subglacial drainage network (Bingham et al., 2006). The same mechanism has been observed in other regions of the High Arctic (Svalbard), where the influence of runoff on velocity diminished once the critical threshold of runoff was produced to create an EDN (Van Pelt et al., 2018). During July when peak velocities were observed on SCB Glacier, temperatures and lake extent were also at their greatest, as such it is likely that increased meltwater was being produced and routed to the bed. Velocities began to slow in August, coincident with the decrease and disappearance of surface lakes, while temperatures remained elevated over winter baselines (Figure 4-4). It can be speculated that the reduced surface area of lakes was a result of the development of an increasingly channelized network which was moving water from the glacier surface to the bed. This further supports that the captured seasonal velocity variability is contributed to by the switch from the IDN to EDN. The evolution from IDN to EDN is not necessarily linear, as an EDN can revert to an IDN once inputs and temperatures reduce (Bingham et al., 2006). This was also identified on SCB Glacier in 2019, where temperatures decreased at the end of June to ~ -10^{o}C, before highest velocities (~267 m a^{-1}) of the study period were identified in July (Figure 4-5).

Besides meltwater production, there are additional factors that may influence seasonal velocity variability on tidewater terminating glaciers, including changes at the ice/ocean interface (Pimentel et al., 2017). For example, sea ice at the terminus can provide backstress to the glacier, which has been recognized via longitudinal lines on sea ice at glacier fronts caused by exerted forward pressure of the terminus (Pimentel et al., 2017). Throughout the study period, sea ice largely remained intact at the terminus of SCB Glacier once velocities had already peaked; and reformed at the terminus once velocities had already returned to winter baselines (Figure 4-4). Given this pattern, it does not seem possible that the buttressing effect of sea ice alone was capable of causing the seasonal velocity fluctuations observed in this study, further suggesting run-off as the main

driver (Pimentel et al., 2017; Moon et al., 2015). Terminus position plays a role in the ice/ocean interface and understanding how its position changes over time can inform which glacier dynamics are in action (Van Wychen et al., 2016). The terminus position of the glacier did not fluctuate to the degree which would be expected of a surging or pulsing glacier, such as what has been seen on Hubbard Glacier with fluctuations > 400 m (Ritchie et al., 2008). This suggests that the 180 m average terminus fluctuation was attributed to seasonal velocities (Ritchie et al., 2008).

Although the seasonal velocity variability discussed was observed to some degree across the entire glacier, the greatest variability occurred where the glacier descends below sea level (Figure 4-6). Looking at standard deviation (SD), a measure of variability from the mean (De Veaux et al., 2014), higher SDs occurred in areas that were increasingly below sea level. Within the normal range, SDs of 0-0.5 and 0.5-1 occur at elevations of -12 m a.s.l. and -64 m a.s.l. respectively. Varying outside of a normal distribution, SDs of 1 – 1.5 occurred on average on areas of the bed -114 m a.s.l., with a lower range for SDs 1.5 – 2 occurred on average at -144 m a.s.l. Finally, the largest variability (SDs > 2) occurred from -162 m a.s.l. to -152 m a.s.l., with a mean of -157 m a.s.l., suggesting that lower bed elevations are associated with greater variability. This is likely due to basal sliding increasingly contributing to velocities, which is supported by the FR4 classification of SCB Glacier's near terminus region (Vieli et al., 2004; Van Wychen et al., 2017). While FR4 does inform us about where we can expect seasonality, having this variability mapped out allows for more detailed defining of the area at the terminus which is most impacted by seasonality.

4.4.1.2 Multi-annual variability in winter flow speeds

Winter velocity variability has previously been identified on SCB Glacier on multi-annual time scales, with irregular periods of oscillation between acceleration and deceleration (Van Wychen et al., 2017; 2020). Most notable is the acceleration which occurred in 2018/19 where velocities exceeded 200 m a^{-1} in the lowermost 12 km of the glacier and persisted into 2019/20 which was identified using a pair of R2 imagery (Van Wychen et al., 2017; 2020). TSX/TDX results presented in this study confirm these results and allowed for further investigation on a finer temporal scale. Average winter velocities increased by 28% from 147 m a^{-1} in 2017/18 to 189 m a^{-1} 2018/19, which exceeded the margin of error (Table 4-3; Figure 4-3). Outside of this acceleration event velocities did not vary beyond of the margin of error until 2021, which may be bias however due to data

extending only until October. Average winter temperatures during the study period did not vary outside of 0.5°C, suggesting that winter temperatures were not the driver of the observed variability. However, summer 2018 had the lowest average temperature during the study period, with only two PDDs (the lowest recorded over the study period) recorded which also coincided with a positive mass balance year, (Figure 4-8; World Glacier Monitoring Service, 2021).

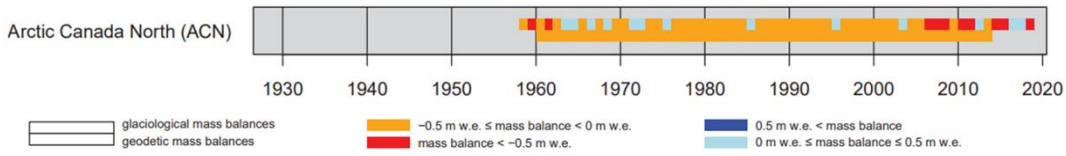

Figure 4-8. Mass balance measurements in Arctic Canada North from 1930 to 2020 (Modified from World Glacier Monitoring Service, 2021)

MB measurements during the study period provide insight to the conditions during the 2018/19 velocity event. Positive MB occurs when accumulation is greater than ablation, which in the Canadian Arctic has been associated with processes such as a reduction in surface melt (Burgess et al., 2013). Reductions in surface meltwater production decrease inputs to the drainage network, which would make the hydraulic switch from an IDN to EDN a longer process that becomes less likely. This is likely what occurred during the summer of 2018, with the AWS temperature record showing that it was the coldest during the study period and optical imagery being predominantly cloud covered. It can be speculated that this anomaly in the data might influence the velocity increase observed in the following winter of 2018/19. This process has previously been identified in the High Arctic (Svalbard), where the drainage network in the preceding summer influenced winter surface velocities (Van Pelt et al., 2018). As such, it is suggested that summer ablation influences velocities in the following winter months (Van Pelt et al., 2018). The process by which this occurs may be the IDN causing storage of water at the ice-bed interface that is not evacuated, allowing for faster hydraulic jacking following a positive MB year (Sundal et al., 2011).

The variability identified on SCB Glacier in previous work, which has been confirmed with these results, does not fit within the classification of dynamics in the CAA (surging, pulsing, or consistent acceleration (Van Wychen et al., 2017). Surging glaciers experience multi-year

variability with oscillations between the surge phase (acceleration initiating up-glacier, propagating downward) and a long quiescent phase (period of stagnation) (Van Wychen et al., 2017). Inconsistent with this definition, SCB Glacier's velocity acceleration initiated in the near-terminus region and did not oscillate into a stagnation, rather just slowed. Pulsing exhibits a similar spatial pattern with acceleration initiating at the near terminus region, but acceleration is restricted to areas grounded below sea level (Van Wychen et al., 2017), which was also not the case for SCB Glacier where accelerated flow propagated into areas of the bed above sea level (i.e. 5 km to 7.5 km from the terminus at -1.2 to -4.3 m a.s.l). Pulsing is also associated with ice flowing over a bedrock sill which induces high variability (Van Wychen et al., 2017). While a bedrock bump is located ~20 km from the terminus (Van Wychen et al., 2017), the velocity variability was not coincident with this point.

Here, it is proposed that the process occurring on SCB Glacier is a distinct from of what is classically understood as surging and pulsing. Terminus variability was more aligned with seasonal fluctuations than surge related fluctuations which have been observed in the CAA, such as on Hubbard Glacier which experiences seasonal fluctuations of 150 to 200 m, aligning with results on SCB Glacier ranging from 94 to 245 m. Surge related fluctuations on Hubbard are 2x greater than the variability observed on SCB Glacier, with an average of ~620 m (Ritchie et al., 2008; Table 4-4). Instead, it is suggested that the dynamics are driven by the hydrological conditions of the glacier. Velocity variability has previously been identified to be greater along the surface where subglacial drainage channels are located due to meltwater penetration to the bed (Copland et al., 2003; Bingham et al., 2006). This follows what was identified in the results presented here, with velocities peaking when the subglacial drainage network remained as an IDN, trapping water at the bed over the winter season (Copland et al., 2003; Bingham et al., 2006).

With this information, previously observed velocity variability reported by Van Wychen and others (2017; 2020) can begin to be explained. It appears the variability is hydrologically driven, which has implications for the glacier, especially in a warming climate. While SCB Glacier does not drain directly into open water (drains into a fjord instead), or impact trade routes, understanding the drivers of variability can inform the dynamics of glaciers in the CAA more generally. This is important as we move into a warming climate where hydrological inputs will increase due to surface meltwater production. Not only this, but considering that the driver of the observed winter

variability is suggested to be the conditions of the previous summer, the classification of pulsing glaciers may be affected by this mechanism as well. As such, this warrants further future investigation.

4.4.2 Feasibility of remote sensing

The dense record of TSX/TDX data available for this study allowed for the generation of a near-continuous velocity record of SCB glacier from 2015 to 2021. The method was able to derive year-round velocities for the study period, with the greatest success in the winter (non-melt-season). However, due to the nature of SAR data and the method which was utilized, loss of coherence between image pairs resulted in data loss. Portions of the glacier with the best coherence occurred in areas that remained relatively unchanged, and/or those with prominent surface features (such as the highly crevassed near terminus region on SCB Glacier). This was evident in the velocities derived during the melt season each year, where coherence was lost upglacier of 4.25 km from the terminus. Up glacier from this point, velocities could not be reliably tracked or compared as a bias towards winter velocities would have been introduced (Figure 4-3). As such, it is feasible to use TSX/TDX imagery for velocity tracking during the winters and in areas with prominent surface features, but to a lesser degree during times of rapid change. Nevertheless, although data loss occured, the method successfully detected seasonality in the near terminus region (where seasonality is expected to occur due to the FR4 classification), providing insight and measurements of seasonal velocity evolution in the CAA where in-situ records of ice motion are not available.

Areas of data loss can be filled using optically derived datasets such as Its-Live (an ongoing program that can give a full view of seasonality when used in combination with SAR; https://its-live.jpl.nasa.gov/). This alleviates some of the concerns with using remote sensing, which has many benefits to the study of velocity. One of these benefits is that spatial and temporal constraints are less of a concern for remote sensing methods compared to in situ measurements, which are restricted by point-locations (if using GPS) and accessibility to the study area. In-situ measurements can also easily become damaged or dislodged due to the extreme climate in the CAA. SAR in particular is advantageous in these conditions due to its all-weather imaging capabilities.

4.5 Conclusion

To conclude, the objectives of this research were to: 1) quantify seasonal and multiannual velocities of SCB Glacier from 2015 to 2021 using 11-day separated TSX/TDX imagery and offset tracking by extracting the centerline velocities, 2) examine the drivers of velocity variability, which were sea ice buttressing, bed topography, and glacier hydrology via SATs and surface lake extent; and 3) assess the feasibility of using remote sensing to track seasonality in the CAA. Seasonally, velocities accelerated from June to August, with peak velocities in July coincident with the greatest number of PDDs and supraglacial lake area; this suggests that hydrology impacts glacier dynamics. A multi-annual and seasonal speed up was identified in the TSX/TDX imagery, most significantly in 2018/19 with winter velocities increasing 41 m a^{-1} (28%) over previous winters in the study period. Lower temperatures in the preceding summer (which was the coldest on record during the study period) are speculated to have caused an IDN to persist and influenced the following winter flow rates by retaining water at the glacier-bed interface. This increased the amount of hydraulic jacking that occurred into the subsequent winter, which increased basal sliding and elevated velocities. The variability on SCB Glacier continues to not conform to either surging or pulsing dynamics due to the propagation of accelerated flow from the near terminus region upglacier into areas of the bed above sea level, as well as no distinctly identifiable quiescence. It is suggested that the fluctuations observed were associated with the hydrology and bed topography of the glacier, while sea ice conditions have been found to have negligible effects on velocities.

This study utilized a catalogue of TSX/TDX data which had not previously been utilized for velocity mapping of SCB Glacier. Results provided a near-continuous 11-day record of velocities over the glacier from 2015 to 2021, which is a level of detail which has not previously been achieved. As such, previous results that were acquired on a coarser resolution can also be validated against observations recorded in this study. One example is the work of Van Wychen and others (2017; 2020), which was the first to identify the acceleration in winter velocities observed in 2018/19 using one pair of R2 imagery. Having this level of detail supports further understanding of glacier dynamics, and how they may change in the future. With rising sea levels,

this is important as velocities impact the amount of meltwater and ice that is discharged to the ocean, contributing directly to sea level rise.

Next steps to build on what has been presented here include the combination of TSX/TDX and Its-Live data to fill the gaps caused by poor coherence. This would increase the level of detail and measurement of the glacier's seasonal velocity evolution above 4.25 km from the terminus. The greatest variability in both summer and winter velocities seems to have occurred at and above this point, as such, combining the data would be valuable in fully capturing what is happening. Further, understanding the mass balance of SCB Glacier would be insightful in terms of gaining the understanding of which processes are occurring. For example, presence of water at the bed can be identified in glacial uplift, and a better understanding of how mass is transferred (in relation to surge/pulse dynamics) would assist in categorizing the glacier. Finally, previous work (Copland et al., 2003; Bingham et al., 2006) has suggested that subglacial hydrology directly corresponds to the velocity variability that occurs in the surface ice. As such, modelling of the glacier hydrological network could inform processes of velocity evolution.

Chapter 5 Conclusions

5.1 Summary

Due to polar amplification, Arctic latitudes will be disproportionately affected by climate change, with effects on glaciers and ice caps (Derksen et al., 2019). Directly contributing to sea level rise through mass loss via meltwater production and ice discharge to the ocean, tidewater terminating glaciers are of particular concern. Understanding how they will behave in an evolving climate will help inform and refine our knowledge of the effects of climate change on the global system (Abram et al., 2019). Devon Ice Cap, Nunavut, Canada has been one of the more extensively studied ice caps in the Canadian Arctic Archipelago (Burgess and Sharp, 2004; Van Wychen et al., 2017). Recent research has identified that most glaciers in the CAA have not been experiencing significant changes in velocities from 2015 to 2020 (Van Wychen et al., 2020). Glaciers which did exhibit significant changes have been classified as pulsing or surging, but there are exceptions in glaciers which have been consistently accelerating (Trinity, Wykeham, and Belcher Glaciers) (Van Wychen et al., 2020). South Croker Bay Glacier provides an interesting case study in the region, as the velocity variability does not align with surging or pulsing, while the glacier has been accelerating in inconsistent time periods (Van Wychen et al., 2017). This variability has not yet been well explained but has been explored in this study using a large collection of TSX/TDX imagery collected since 2015. This dense record of SAR data has been used to derive velocities every 11-days from 2015 to 2021. As such, the major research objectives of this thesis were to:

1) Quantify the seasonal and multi-annual ice motion of SCB, a major tidewater terminating glacier on DIC primarily using remote sensing data and methods;
2) Examine the relationship between sea ice conditions, hydrology and glacier bed topography as drivers and controls on the observed variability; and
3) Assess the feasibility of using remote sensing methods to track seasonal changes in glacier motion in the Canadian High Arctic.

5.2 Primary findings

The following section will review the primary findings related to each of the three major research objectives. It is sub-divided by each major research objective.

5.2.1 Primary Findings in support of Research Objective 1

The main research objective was to quantify the seasonal and multi-annual velocity of SCB Glacier, Devon Ice Cap, Nunavut, Canadian Arctic. From previous work on the ice cap, it has been found that SCB Glacier exhibits multi-annual variability which does not fit within the classifications of dynamics in the CAA, which are surging and pulsing (Van Wychen et al., 2017; 2020). Using TSX/TDX imagery and offset tracking, velocities were found to vary between the melt season (summer) and non-melt season (winter), with average velocities of 233 m a^{-1} and 165 m a^{-1} during the study period, respectively. Velocities were on average 49.8% faster in June, July, and August than in other months, with peak velocities occurring in July. Multi-annually, winter flow rates ranged from 122 m a^{-1} to 227 m a^{-1}. Winters did not vary outside of the margin of error from 2015 to 2017/18, but they did change behaviour in 2018/19 when velocities increased 28% from the previous winter from 147 m a^{-1} to 189 m a^{-1}. Velocities remained elevated compared to prior measurements for the duration of the study period. Summer flow remained relatively consistent each year, with velocities ranging from a minimum of 218 m a^{-1} to a maximum of 243 m a^{-1}. Variability did not exceed the margin of error between any of the years in the study. The observed variability was not attributed to surging or pulsing due to the fluctuations of the terminus position reflecting what is seen during a seasonal evolution rather than a surge.

5.2.2 Primary Findings in support of Research Objective 2

The second research objective was to examine the potential drivers and controls on the observed variability. The selected drivers were sea ice buttressing, hydrology, and the control was glacier bed topography. Sea ice buttressing was investigated using Weekly Regional Ice Charts from the Canadian Ice Service (Environment and Climate Change Canada, 2016), and was not found to have a meaningful effect on seasonal and multi-annual velocity variability. Velocities increased in June, prior to sea ice dissipation at the terminus of the glacier which usually occurred

mid-to-late July; and slowed before ice returned to the terminus of SCB Glacier in late October. Similar conclusions have been made by Pimentel and others (2017) and Moon and others (2015), where the magnitude of velocity observed on tidewater terminating glaciers was found to be too large to be the result of sea ice buttressing alone.

The terminus of SCB Glacier is grounded below sea level, which has been identified by previous literature (Dowdeswell et al., 2004) to be a control on areas of velocity variability. Results support this assertion for SCB Glacier, with the greatest standard deviation of velocities observed on average across areas of the bed -152 m a.s.l, while the least occurred on areas on average -12 m a.s.l. This may be the result of increased likelihood of deformable sediments underlying this area of the glacier (Dowdeswell et al., 2004). Topography is also related to glacier hydrology, as water is more likely to penetrate areas below sea level. Finally, glacier hydrology was investigated via proxies of surface lake area and SATs, which provide indications of meltwater production on the glacier. Surface lake area peaked coincident with velocities throughout the study period, as did SATs. Together with information gathered from previous literature (Danielson and Sharp, 2013; Copland et al., 2003; Bingham et al., 2006), it is suggested that the observed seasonal acceleration that occurred on the glacier was due to an inefficient drainage network becoming pressurized, which caused increased velocities as a result of increased meltwater inputs to the system. The glacier then slowed when the system evolved into an efficient drainage network.

This is also suggested to be the mechanism behind the multi-annual variability observed between 2017/18 and 2018/19. Summer 2018, which preceded the highest average winter flow rates in 2018/19, was the coolest on record (-6.4^{o}C) with the lowest number of PDDs (two) during the study period. This was also a positive mass balance year with a higher frequency of cloud cover present in the optical imagery during the melt season than other years in the study period, indicating that the glacier experienced significantly different climatic conditions in 2018. Taking this into consideration, it is suggested that cooler climatic conditions with reduced meltwater inputs to the hydrological network may have led to storage of water at the ice-bed interface of SCB Glacier in summer 2018 and the following winter 2018/19, resulting in increased hydraulic jacking and basal sliding. This can be the result of oscillations between inefficient and efficient drainage networks during the melt season, as has previously been identified in the CAA (Copland et al.,

2003). This does not fit within the current definition of pulsing, although the temporal evolution is comparable, but may be an extension of the process caused by the hydrological network.

5.2.3 Primary Findings in support of Research Objective 3

The third research objective of the study was to assess the feasibility of using remote sensing to track seasonality in the study area, extending more generally to the CAA. Using TSX/TDX imagery for offset tracking was successful in tracking velocities continuously every 11-days for a 5-year period, regardless of daylight and weather conditions. While this is a benefit over using optical imagery with feature tracking, offset tracking must retain coherence between image pairs to identify displacements. This performed well in areas with prominent surface features (i.e. crevasses) or with little change between the acquisitions, but year-round coherence was maintained only in the area up to 4.25 km from the terminus of SCB Glacier. Up glacier from this point coherence was lost during the summer, likely due to large amounts of surface melt occurring. Therefore, it is suggested that optimal results would be derived from the combination of SAR and optically derived data, such as NASA's Its-Live (https://its-live.jpl.nasa.gov/). Optical data can fill the gap in SAR derived results for year-round velocity tracking, which is not subject to the same spatial and temporal constraints as in situ data collection, proving the feasibility of the method.

5.3 Limitations

This study was limited by supplementary data availability and time constraints. Most significantly, there were no in-situ velocity records to validate TSX/TDX derived velocities against. Velocities were confirmed using studies which employed comparable methods, which would have similar underlying biases. Provided that in-situ data becomes available, it should be compared to enhance confidence in the results presented in this study. Similarly, hydrology and meltwater production (the suggested driver of the observed variability) were determined via proxies of surface lake area and surface air temperatures. As such, literature was used to inform how these processes have affected other glaciers and applied to SCB Glacier, when the hydrological system has not yet been modelled or studied, potentially leading to incorrect conclusions. Next, four imaging geometries were used for terminus position analysis. Due to the

inconsistent geometric distortions, each terminus could only be compared to those digitized on the same geometry, resulting in an inconsistent and discontinuous analysis of position. As such, seasonal and multi-annual fluctuations may have been lost. This can be addressed by georeferencing all the geometries to one another, but this was not possible for this project due to time constraints.

Another limitation when investigating and exploring the drivers of the unusual dynamics of SCB Glacier is that it is relatively understudied. Previous literature reported results on a coarse scale, averaging decades of velocities (Millan et al., 2017) or providing annual estimates of velocities using single winter snapshots (Van Wychen et al., 2017; 2020). While this context is valuable and provides the basis for investigating further, there is little information to compare to. Data in these studies dates back to 1991, while other glaciers have a dense record of in situ results for interpreting changes in velocity dynamics, such as White and Thompson Glaciers which have had records since 1959, investigating velocity structure and terminus positions (Hambrey and Müller, 1978; Iken, 1974; Kälin, 1971). Moving forward, studies like this one will help future research by utilizing existing data to create a large catalogue of glacier velocities that can be used to study.

5.4 Significance

This study has created one of the densest velocity records for the CAA to date using a catalogue of TSX/TDX data which has not previously been utilized for velocity mapping of SCB Glacier. This allowed for the creation of a near-continuous record of velocities every 11 days from 2015 to 2021. The level of detail presented in this work has not previously been presented for the glacier, which has confirmed of results of previous work presented by Van Wychen and others (2017; 2020) that identified poorly understood dynamics. With this, a deeper investigation of the dynamics was done, confirming that SCB Glacier does not fit into the classifications of surging or pulsing. Rather, another mechanism has been proposed which suggests that the observed variability may be a form of pulsing that is driven by the hydrological network. This information provides a basis for further study of the glacier and provides a historical record of seasonal and multi-annual velocities which is valuable in a warming climate. Not only this, but this work

confirms that remote sensing methods can be applied to other glaciers in the CAA which may be difficult to assess using in-situ methods.

5.5 Future work

Due to the loss of coherence during the melt season, valuable velocity data which can inform glacier dynamics was lost. To get a full understanding of the velocity evolution across the entire glacier the inclusion of NASA's Its-Live (https://its-live.jpl.nasa.gov/) is the next step that would improve the quality of these results. This would enable investigation of the seasonal evolution of velocities up glacier from 4.25 km from the terminus, potentially informing the dynamic processes that are driving the observed velocity variability. Results indicate that there may have been faster velocities occurring in the area above 4.25 km from the terminus compared to in the near terminus region. This is of particular interest when investigating the unusual dynamics of SCB Glacier and whether it is surging or pulsing, because surging is initiated in the upper reaches of the glacier, with changes propagating down glacier (Van Wychen et al., 2016), which cannot be observed in this study. The inclusion of Its-Live would fill this gap and elevate the confidence of the suggested hypothesis that the glacier is not surging or pulsing.

Another factor in understanding dynamics is how mass is transferred along a glacier, directly related again to the dynamics of surging and pulsing. As such future work should include Digital Elevation Model differencing. This would also help quantify how much dynamic discharge is being lost to the ocean, refining sea level rise estimates. Not only this, but having an estimate of vertical uplift can inform conditions of the hydrological network, with increased inputs and storage causing uplift which reduce once water is evacuated (Bingham et al., 2006). This can be done using Hugonnet and others (2021) data and resources (GitHub - rhugonnet/ww_tvol_study: Process global-scale satellite and airborne elevation data into time series of glacier mass change: Hugonnet et al. (2021).), which allow for the processing of remotely sensed elevation data to obtain a time series of glacier mass fluctuations. Much emphasis in studying glacier mass balance has been put on Greenland and Antarctica, although glaciers outside of this area have doubled their rates of thinning in the past 20 years (Hugonnet et al., 2021). Understanding the mass balance conditions can help identify co-related processes which may be affecting the mass balance, such

as precipitation and temperature (Hugonnet et al., 2021). This would directly contribute to the understanding of what drives glacier dynamic change.

Finally, the glacier hydrological network has been identified in previous literature (Copland et al., 2003; Bingham et al., 2006) as a direct contributor to surface velocities and areas of greatest variability. The distribution and location of subglacial and englacial channels has been suggested to control storage of water at the bed of a glacier, which would in turn influence the rates of basal sliding (Copland et al., 2003). This becomes increasingly important with climate change causing increased SATs, which contribute to enhanced meltwater production. As such, modelling the hydrology of SCB Glacier can potentially confirm or deny the hypothesis presented by this study, that the inefficient drainage channels are the cause of the surface variability, and allow for predictions of how the glacier may evolve in the future.

References

Abram, N., Gattuso, J. P., Prakash, A., Cheng, L., Chidichimo, M. P., Crate, S., Enomoto, H., Garschagen, M., Gruber, N., Harper, S., Holland, E., Kudela, R. M., Rice, J., Steffen, K. & von Schuckmann, K. (2019). IPCC Special Report on the Ocean and Cryosphere in a Changing Climate: Framing and Context of the Report. *Intergovernmental Panel on Climate Change.*

Airbus Defence and Space. (2015). TerraSAR-X image product guide: Basic and enhanced radar satellite imagery. https://www.intelligence-airbusds.com/files/pmedia/public/r459_9_20171004_tsxx-airbusds-ma-0009_tsx-productguide_i2.01.pdf

Alaskan Satellite Facility. (n.d.) *What is SAR?* Retrieved from: https://asf.alaska.edu/information/sar-information/what-is-sar/

Benn, D. & Evans, D. J. (2010). Glaciers and Glaciation, 2nd Ed. *Routledge: Taylor and Francis Group*, London and New York.

Bingham, R. G., Nienow, P. W., Sharp, M. J. & Boon, S. (2005). Subglacial drainage processes at a High Arctic polythermal valley glacier. *Journal of Glaciology*, 51(172). https://doi.org/10.3189/172756505781829520

Bingham, R. G., Neinow, P. W., Sharp, M. J. & Copland, L. (2006). Hydrology and dynamics of a polythermal (mostly cold) High Arctic glacier. *Earth Surface Processes and Landforms*, 31, 1463-1479. DOI:10.1017/jog.2017.3

Boon, S., Burgess, D. O., Koerner, R. M. & Sharp, M. J. (2010). Forty-seven years of research on the Devon Island Ice Cap, Arctic Canada. *Arctic*, 63(1), p 13-29.

Burgess, D. O. (2017). Mass balance of ice caps in the Queen Elizabeth Islands, Arctic Canada: 2014-2015; Geological Survey of Canada, Open File 8223, p. 38. Doi: 10.4095/300231

Burgess, E. W., Larsen, C. F. & Forster, R. R. (2013). Summer melt regulates winter glacier flow speeds throughout Alaska. *Geophysical Research Letters*, 40. doi:10.1002/2013GL058228

Burgess, D. O. & Sharp, M. J. (2004). Recent changes in areal extent of the Devon Ice Cap, Nunavut, Canada. *Arctic, Antarctic and Alpine Research*, 36(2). DOI: 10.1657/1523-0430(2004)036[0261:RCIAEO]2.0.CO;2

Burgess, D. O., Sharp, M. J., Mair, D. W. F., Dowdeswell, J. A. & Benham, T. J. (2005). Flow dynamics and iceberg calving rates of Devon Ice Cap, Nunavut, Canada. *Journal of Glaciology*, 51(173). https://doi.org/10.3189/172756505781829430

Carr, J. R., Vieli, A. & Stokes, C. (2013). Influence of sea ice decline, atmospheric warming, and glacier width on marine-terminating outlet glacier behaviour in northwest Greenland at seasonal to interannual timescales. *Journal of Geophysical Research: Earth Surface*, 118. DOI: 10.1080/01431161.2019.1658238

Copland, L., Sharp, J. M. & Dowdeswell, J. A. (2003). The distribution and flow characteristics of surge-type glaciers in the Canadian High Arctic. *Annals of Glaciology*, 36. https://doi.org/10.3189/172756403781816301

Dalton, A., Copland, L., Tivy, A., Van Wychen, W. & Cook, A. (2019). Iceberg production and characteristics around the Prince of Wales Icefield, Ellesmere Island, 1997-2015. *Arctic, Antarctic, and Alpine Research*, 51(1). DOI: 10.1080/15230430.2019.1634442

Dalton, A., Van Wychen, W., Copland, L., Gray, L. & Burgess, D. (2022). Seasonal and multiyear flow variability on the Prince of Wales Icefield, Ellesmere Island: 2009 – 2019. *Journal of Geophysical Research: Earth Surface,* 127, https://doi.org/10.1029/2021JF006501

Danielson, B. & Sharp, M. (2013). Development and application of a time-lapse photograph analysis method to investigate the link between tidewater glacier flow variations and supraglacial lake drainage events. *Journal of Glaciology*, 59(214). doi:10.3189/2013JoG12J108

Davison, B. J,, Sole, A. J., Cowton, T. R., Lea, J. M., Slater, D. A., Fahrner, D. & Nienow, P. W. (2020). Subglacial drainage evolution modulates seasonal ice flow variability of three tidewater glaciers in southwest Greenland. *Journal of Geophysical Research: Earth Surface*, 125(9), https://doi.org/10.1029/2019JF005492

Dingle-Robertson, L. (August, 2021). Synthetic Aperture Radar Remote Sensing. *Carleton University*.

Dowdeswell, J. A., Benham, T. J., Gorman, M. R., Burgess, D. & Sharp, M. J. (2004). Form and flow of the Devon Island Ice Cap, Canadian Artic. *Journal of Geophysical Research: Earth Surface*, 109(F2). https://doi.org/10.1029/2003JF000095

Derksen, C., Burgess, D., Duguay, C., Howell, S., Mudryk, L., Smith, S., Thackeray, C. and Kirchmeier-Young, M. (2019). Changes in snow, ice, and permafrost across Canada; Chapter 5 in Canada's Changing Climate Report, (ed.) E. Bush and D.S. Lemmen; Government of Canada, Ottawa, Ontario, p.194–260.

De Veaux, R. D., Velleman, P. F., Bock, D. E., Vukov, A. M. & Wong, A. (2014). Stats: Data and models, 2nd ed. *Pearson Canada*.

EarthData. (n.d.). *IceBridge data: NASA's Operation IceBridge aircraft missions*. NASA Distributed Active Archive Center at NSIDC. https://nsidc.org/data/icebridge

Earth Resources Observation and Science Center. (2020). *USGS EROS archive – Landsat archives – Landsat 8-9 operational land imager and thermal infrared sensor collection 2*

level-1 data. https://www.usgs.gov/centers/eros/science/usgs-eros-archive-landsat-archives-landsat-8-9-operational-land-imager-and

Eineder, M., Fritz, T., Mittermayer, J., Roth, A., Börner, E. & Breit, H. (2009). *TerraSAR-X ground segment: Basic product specification document* (TX-GS-DD-3302). German Aerospace Center. https://tandemx-science.dlr.de/pdfs/TX-GS-DD-3302_Basic-Products-Specification-Document_V1.6.pdf

Environment and Climate Change Canada. (2016, March 7). *Information about archived ice data*. Government of Canada. https://www.canada.ca/en/environment-climate-change/services/ice-forecasts-observations/latest-conditions/archive-overview/information-about-data.html

Environment and Climate Change Canada. (2020, November 9). *Ice chart descriptions*. Government of Canada. https://www.canada.ca/en/environment-climate-change/services/ice-forecasts-observations/latest-conditions/products-guides/chart-descriptions.html#weekly_ice

European Space Agency. (n.d.a). *Level-1*. https://sentinels.copernicus.eu/web/sentinel/user-guides/sentinel-1-sar/product-types-processing-levels/level-1#:~:text=Level%2D1%20data%20can%20be,reduce%20the%20impact%20of%20speckle.

European Space Agency. (n.d.b). *Operational Land Imager (OLI) overview*. Earth Online. https://earth.esa.int/eogateway/instruments/oli-landsat-8-/description

European Space Agency. (n.d.c). *Sentinel 2*. https://sentinel.esa.int/web/sentinel/missions/sentinel-2

European Space Agency. (n.d.d). *TerraSAR-X and TanDEM-X*. Retrieved from: https://earth.esa.int/eogateway/missions/terrasar-x-and-tandem-

x#:~:text=TerraSAR%2DX%20and%20TanDEM%2DX%20are%20German%20radar%20satellites%20from,by%20any%20other%20spaceborne%20sensor.

European Space Agency. (n.d.e). *Copernicus DEM – Global and European Digital Elevaation Model (COP-DEM)*. https://spacedata.copernicus.eu/web/cscda/dataset-details?articleId=394198

Gogineni, P. (2012). *Radar depth sounder data products*. Digital Media, Lawrence, Kansas, USA. https://data.cresis.ku.edu/

Government of Canada. (2015). *Radar basics.* Retrieved from: https://www.nrcan.gc.ca/maps-tools-and-publications/satellite-imagery-and-air-photos/tutorial-fundamentals-remote-sensing/microwave-remote-sensing/radar-basics/9355

Government of Canada. (2016). *Viewing geometry and spatial resolution.* Retrieved from: https://www.nrcan.gc.ca/maps-tools-and-publications/satellite-imagery-and-air-photos/tutorial-fundamentals-remote-sensing/microwave-remote-sensing/viewing-geometry-and-spatial-resolution/9341

Hall, N. (2017). *IceBridge MCoRDS L2 ice thickness, version 1: User guide* (IRMCR2-V001). National Snow and Ice Data Center. https://nsidc.org/data/IRMCR2/versions/1

Hambrey, M. J. & Müller, F. (1978). Structures and ice deformation in the White Glacier, Axel Heiberg Island, Northwest Territories, Canada. *Journal of Glaciology*, 20(82). https://doi.org/10.3189/S0022143000021213

Harcourt, W. D., Palmer, S. J., Mansell, D. T., Le Brocq, A., Bartlett, O., Gourmelen, N., Tepes, P., Dowdeswell, J. A., Blankenship, D. D. & Young, D. A. (2020). Subglacial controls on dynamic thinning at Trinity-Wykeham Glacier, Prince of Wales Ice Field, Canadian Arctic. *International Journal of Remote Sensing*, 41(3), DOI: 10.1080/01431161.2019.1658238

Herdes, E., Copland, L., Danielson, B. & Sharp, M. (2012). Relationship between iceberg plumes and sea-ice conditions on northeast Devon Ice Cap, Nunavut, Canada. *Annals of Glaciology*, 53(60). doi: 10.3189/2012AoG60A163

Hugonnet, R., McNabb, R., Berthier, E., Menounos, B., Nuth, C., Girod, L., Farinotti, D., Huss, M., Dussaillant, I., Brun, F. & Kaab, A. (2021). Accelerated global glacier mass loss in the early twenty-first century. *Nature Letters*, 592, https://doi.org/10.1038/s41586-021-03436-z

Iken, A. (1972). Measurements of water pressure in moulins as part of a movement study of the White Glacier, Axel Heiberg Island, Northwest Territories, Canada. *Journal of Glaciology*, 11(61). https://www.cambridge.org/core/services/aop-cambridge-core/content/view/28CF7B38892C543D229A0E1D780A8D8E/S0022143000022486a.pdf/measurements_of_water_pressure_in_moulins_as_part_of_a_movement_study_of_the_white_glacier_axel_heiberg_island_northwest_territories_canada.pdf

Iken, A. (1974). Velocity fluctuations of an arctic valley glacier: a study of the White Glacier, Axel Heiberg Island, Canadian Arctic Archipelago. *Jacobsen-McGill Arctic Research Expedition 1959-2962*, 5. https://doi.org/10.3929/ethz-a-000090485

Kälin, M. (1971). The active push moraine of the Thompson Glacier, Axel Heiberg Island, Canadian Arctic Archipelago, Canada. *Doctoral thesis*. https://doi.org/10.3929/ethz-a-000088589

Krumwiede, B. S., Kamp, U. Leonard, G. J., Kargel, J. S., Dashtseren, A. & Walther, M. (2014). Recent glacier changes in the Mongolian Altai Mountains: Case studies from Munkh Khairkhan and Tavan Bogd.

Liu, G., Chen, R. & Wang, X. (2021). Spatial and temporal variability in positive degree day in Western China under climate change. *Atmosphere*, 12(443). https://doi.org/10.3390/atmos12040443

Luckman, A., Benn, D. I., Cottier, F., Bevan, S., Nilsen, F. & Inall, M. (2015). Calving rates at tidewater glaciers vary strongly with ocean temperature. *Nature Communications*, 6(8566). doi: 10.1038/ncomms9566

MacGregor, J. A., Boisvert, L. N., Medley, B., Petty, A. A., Harbeck, J. P., Bell, R. E., Blair, J. B., Blanchard-Wrigglesworth, E., Buckley, E. M., Christoffersen, M. S., Cochran, J. R., Csatho, B. M., De Marco, E. L., Dominguez, R. T., et al. (2021). The scientific legacy of NASA's Operation IceBridge. *Reviews of Geophysics*, 59. https://doi.org/10.1029/2020RG000712

Mair, D., Burgess, D. & Sharp, M. (2005). Thirty-seven year mass balance of Devon Ice Cap, Nunavut, Canada, determined by shallow ice coring and melt modeling. *Journal of Geophysical Research*, 110, doi: 10.1029/2003JF000099

McNairn, H. & De Lisle, D. (2018). *The RADARSAT-Constellation Mission (RCM).* https://directory.eoportal.org/web/eoportal/satellite-missions/r/rcm#references

Medrzycka, D., Copland, L., Van Wychen, W. & Burgess, D. (2019). Seven decades of uninterrupted advance of Good Friday Glacier, Axel Heiberg Island, Arctic Canada. *Journal of Glaciology*, 65(251). doi: 10.1017/jog.2019.21

Millan, R., Mouginot, J. & Rignot, E. (2017). Mass budget of the glaciers and ice caps of the Queen Elizabeth Islands, Canada, from 1991 to 2015. *Environmental Research Letters*, 12(2). https://doi.org/10.1088/1748-9326/aa5b04

Moon, T. & Joughin, I. (2008). Changes in ice front position on Greenland's outlet glaciers from

1992 to 2007. *Journal of Geophysical Research: Earth Surface*, 112(F2). https://doi.org/10.1029/2007JF000927

Moon, T., Joughin, I. & Smith, B. (2015). Seasonal to multiyear variability of glacier surface velocity, terminus position, and sea ice/ice mélange in northwest Greenland. *Journal of Geophysical Research,* 120, doi: 10.1002/2015JF003494

Moran, T. & Marshall, S. (2009). The effects of meltwater percolation on the seasonal isotopic signals in an Arctic snowpack. *Journal of Glaciology*, 55(194). doi:10.3189/002214309790794896

Mortimer, C. A., Sharp, M. & Van Wychen, W. (2018). Influence of recent warming and ice dynamics on glacier surface elevations in the Canadian High Arctic, 1995-2014. *Journal of Glaciology,* 64(245), 450-464. doi: 10.1017/jog.2018.37

NASA. (2021, December 21). *Landsat 8: Landsat science.* Landsat Science. https://landsat.gsfc.nasa.gov/satellites/landsat-8/

Noël, B., Jan van de Berg, W., Lhermitte, S., Wouters, B., Schaffer, N., & van den Broek, M. R. (2018). Six decades of glacial mass loss in the Canadian Arctic Archipelago. *Journal of Geophysical Research: Earth Surface*, 123(6). https://doi.org/10.1029/2017JF004304

NSIDC. (n.d.) IceBridge MCoRDS L2 Ice Thickness, Version 1 (IRMCR2). https://nsidc.org/data/irmcr2/versions/1

Paden, J., Li, J., Leuschen, C., Rodrigues-Morales, F. & Hale, R. (2010). IceBridge MCoRDS L2 ice thickness, Version 1 [South Croker Bay]. Boulder, Colarado USA. *NASA National Snow and Ice Data Center Distributed Active Archive Center,* https://doi.org/10.5067/GDQ0CUCVTE2Q

Pfeffer, W. T., Arendt, A. A., Bliss, A., Bolch, T., Cogley, J. G., Gardner, A. S., Hagen, J. O., Hock, R., Kaser, G., Kienholz, C., Miles, E. S., Moholdt, G., Mölg, N., Paul, F., Radić, V., Rastner, P., Raup, B. H., Rich, J., Sharp, M. J. & The Randolph Consortium. (2017). The Randolph Glacier Inventory: a globally complete inventory of glaciers. *Journal of Glaciology*, 60(221).

Pimentel, S., Flowers, G. E., Sharp, M. J., Danielson, B., Copland, L., Van Wychen, W., Duncan, A. & Kavanaugh, L. J. (2017). Modelling intra-annual dynamics of a major marine-terminating Arctic glacier. *Annals of Glaciology*, 58(74). doi: 10.1017/aog.2017.23

RGI Consortium. (2017). Randolph Glacier Inventory – A dataset of global glacier outlines, version 6. Boulder, Colorado USA. *NSIDC: National Snow and Ice Data Center*. doi: https://doi.org/10.7265/4m1f-gd79

Ritchie, J. B., Lingle. C. S., Motyka, R. J. & Truffer, M. (2008). Seasonal fluctuations in the advance of a tidewater glacier and potential causes: Hubbard Glacier, Alaska, USA. *Journal of Glaciology*, 54.

Rohner, C., Small, D., Beutel, J., Henke, D., Luthi, M. P. & Vieli, A. (2019). Multisensor validation of tidewater glacier flow fields derived from synthetic aperture radar (SAR) intensity tracking. *The Cryosphere*, 13. https://doi.org/10.5194/tc-13-2953-2019

Sánchez-Gámez, P. & Navarro, F. J. (2017). Glacier surface velocity retrieval using D-InSAR and offset tracking techniques applied to ascending and descending passes of Sentinel-1 data for Southern Ellesmere Ice Caps, Canadian Arctic. *Remote Sensing of Glaciers,* 9(422). doi:10.3390/rs9050442

Schaffer, N., Copland, L. & Zdanowicz, C. (2017). Ice velocity changes on Penny Ice Cap, Baffin Island, since the 1950s. *Journal of Glaciology*, 63(240), 716-730. https://doi.org/10.1017/jog.2017.40

Schellenberger, T., Van Wychen, W., Copland, L., Kääb, A. & Gray, L. (2016). An inter-comparison of techniques for determining velocities of maritime arctic glaciers, Svalbard, using radarsat-2 wide fine mode data. *Remote Sensing*, 8(785). doi:10.3390/rs8090785

Schubert, A., Faes, A., Kääb, A. & Meier, E. (2013). Glacier surface velocity estimation using repeat TerraSAR-X Images: Wavelet- vs. correlation-based image matching. *IPRS Journal of Photogrammetry and Remote Sensing*, 82.

Sentinel Hub. (n.d.a). *Sentinel-2 L1C.* https://docs.sentinel-hub.com/api/latest/data/sentinel-2-l1c/

Sentinel Hub. (n.d.b). *Sentinel-2 L2A.* https://docs.sentinel-hub.com/api/latest/data/sentinel-2-l2a/

Sharp, M. (1988). Surging glaciers: behaviour and mechanisms. *Progress in physical geography*, 12(3). DOI: 10.1177/030913338801200302

Sharp, M., Burgess, D. O., Cawkwell, F., Copland, L., Davis, J. A., Dowdeswell, E. K., Dowdeswell, J. A., Gardner, A. S., Mair, D., Wang, L., Williamson, S. N., Wolken, G. J. & Wyatt, F. (2014). Remote sensing of recent changes in the Canadian Arctic. *Global Land Ice Measurements from Space*. https://doi.org/10.1007/978-3-540-79818-7_9

Sharp, M., Burgess, D. O., Cogley, J. G., Eccleston, M., Labine, C. & Wolken, G. J. (2011). Extreme melt on Canada's Arctic ice caps in the 21st century. *Geophysical Research Letters*, 38. doi:10.1029/2011GL047381

Shepherd, A., Du, Z., Benham, T. J., Dowdeswell, J. A. & Morris, E. (2007). Mass balance of Devon Ice Cap, Canadian Arctic. *Annals of Glaciology*, 46. https://doi.org/10.3189/172756407782871279

Short, , N. H. & Gray, A. L. (2005). Glacier dynamics in the Canadian High Arctic from RADARSAT-1 speckle tracking. *Canadian Journal of Remote Sensing*, 31(3). doi: 10.5589/m05-010

Strozzi, T., Luckman, A., Murray, T., Wegmüller, U. & Werner, C. L. (2002). Glacier motion estimation using SAR offset-tracking procedures. *IEEE Transaction on Geoscience and Remote Sensing*, 40(11). https://doi.org/10.1109/TGRS.2002.805079

Strozzi, T., Paul, F., Wiesmann, A., Schellengerger, T. & Kääb, A. (2017). Circum-arctic changes in the flow of glaciers and ice caps from satellite SAR data between the 1990s and 2017. *Remote Sensing*, 9. doi:10.3390/rs9090947

Sundal, A. V., Shepherd, A., Nienow, P., Hanna, E., Palmer, S. & Huybrechts, P. (2011). Melt-induced speed-up of Greenland ice sheet offset by efficient subglacial drainage. *Nature Letters*, 469. doi:10.1038/nature09740

Thomson, L. I. & Copland, L. (2017). Multi-decadal reduction in glacier velocities and mechanisms driving deceleration at polythermal White Glacier, Arctic Canada. *Journal of Glaciology*, 63(239). DOI:10.1017/jog.2017.3

Tivy, A., Howell, S. E. L., Alt, B., McCourt, S., Chagnon, R., Crocker, G., Carrieres, T. & Yackel, J. J. (2011). Trends and variability in summer sea ice cover in the Canadian Arctic based on the Canadian Ice Service digital archive, 1960-2008 and 1968-2008. *Journal of Geophysical Research*, 116, https://doi.org/10.1029/2009JC005855

U.S. Geological Survey. (2019, February 1). *What are the band designations for the Landsat satellites?* https://www.usgs.gov/faqs/what-are-band-designations-landsat-satellites

Uszczyk, A., Grabeic, M., Laska, M., Kuhn, M. & Ignatiuk, D. (2019). The importance of snow as a component of surface mass balance of Arctic glacier (Hansbreen, southern Spitsbergen). *Polish Polar Research*, 40(4). doi: 10.24425/ppr.2019.130901

van Pelt, W. J. J., Pohjola, V. A., Pettersson, R., Ehwald, L. E., Reijmer, C. H., Boot, W. & Jakobs, C. L. (2018). Dynamic response of a High Arctic glacier to melt and runoff variations. *Geophysical Research Letters*, 45. https://doi.org/10.1029/2018GL077252

Van Wychen, W., Burgess, D., Gray, L., Copland, L., Sharp, M., Dowdeswell, J. A. & Benham, T. J. (2014). Glacier velocities and dynamic discharge from the Queen Elizabeth Islands, Nunavut, Canada. *Geophysical Research Letters*, 41(2). doi: 10.1002/2013GL058558

Van Wychen, W., Burgess, D., Kochtitzky, W., Nikolic, N., Copland, L. & Gray, L. (2020). RADARSAT-2 derived glacier velocities and dynamic discharge estimates for the Canadian High Arctic: 2015-2020. *Canadian Journal of Remote Sensing*, 46(6), 695-714. https://doi.org/10.1080/07038992.2020.1859359

Van Wychen, W., Copland, L., Gray, L., Burgess, D., Danielson, B. & Sharp, M. (2012). Spatial and temporal variation of ice motion and ice flux from Devon Ice Cap, Nunavut, Canada. *Journal of Glaciology*, 58(210). doi: 10.3189/2012JoG11J164

Van Wychen, W., Davis, J., Burgess, D. O., Copland, L., Gray, L., Sharp, M. & Mortimer, Colleen. (2016). Characterizing interannual variability of glacier dynamics and dynamic discharge (1999-2015) for the ice masses of Ellesmere and Axel Heiberg Islands, Nunavut, Canada. *Journal of Geophysical Research: Earth Suface*, 121, 39-63. doi:10.1002/ 2015JF003708

Van Wychen, W., Davis, J., Copland, L., Burgess, D. O., Gray, L., Sharp, M., Dowdeswell, J. A. & Benham, T. J. (2017). Variability in ice motion and dynamic discharge from Devon Ice Cap, Nunavut, Canada. *Journal of Glaciology*, 63(239), 436-449. doi: 10.1017/jog.2017.2

Van Wychen, W., Halle, D. A. M., Copland, L. & Gray, L. (2022). Anomalous surface elevation, velocity and area changes of Split Lake Glacier, western Prince of Wales Icefield, Canadian High Arctic. *Arctic Science*.

Vieli, A., Jania, J., Blatter, H. & Funk, M. (2004). Short-term velocity variations on Hansbreen, a tidewater glacier in Spitsbergen. *Journal of Glaciology*, 50(170), https://doi.org/10.3189/172756504781829963

Wegmüller, U. (2021). *GAMMA software information, v2.2*. GAMMA Remote Sensing. https://GAMMA-rs.ch/uploads/media/GAMMA_Software_information.pdf

Williamson, S., Sharp, M., Dowdeswell, J. & Benham, T. (2008). Iceberg calving rates from northern Ellesmere Island ice caps, Canadian Arctic, 1999-2003. *Journal of Glaciology*, 54(186). https://doi.org/10.3189/002214308785837048

World Glacier Monitoring Service. (2021). Global glacier change bulletin No. 4 (2018-2019). Zemp, M., Nussbaumer, S. U., Gartner-Roer, I., Bannwart, J., Paul, F. & Hoelzle, M (eds). *ISC(WDS)/IUGG(IACS)/UNEP/UNESCO/WMO*. doi:10.5904/wgms-fog-2021-05

Wyatt, F. R. & Sharp, M. J. (2015). Linking surface hydrology to flow regimes and patterns of velocity variability on Devon Ice Cap, Nunavut. *Journal of Glaciology*, 61(226). doi: 10.3189/2015JoG14J109

Wyatt, F. R. & Sharp, M. J. (2017). Linking surface hydrology to flow regimes and patterns of velocity variability on Devon Ice Cap, Nunavut. *Journal of Glaciology*, 61(226). https://doi.org/10.3189/2015JoG14J109

Appendix

Appendix A.

This table lists all of the quick looks that were downloaded from Sentinel Hub EO to delineate supraglacial lake surface areas, using Landsat 8 (L8), Landsat-8/9 (L8/9), and Sentinel-2. Only cloud free imagery was selected for download.

	2015	
Sensor Type	**Image**	**Count**
L8	2015-03-18-00_00_2015-03-18-23_59_Landsat_8_L2_Highlight_Optimized_Natural_Color	
L8	2015-03-20-00_00_2015-03-20-23_59_Landsat_8_L2_Highlight_Optimized_Natural_Color	
L8	2015-03-20-00_00_2015-03-20-23_59_Landsat_8_L2_Highlight_Optimized_Natural_Color	
L8	2015-03-27-00_00_2015-03-27-23_59_Landsat_8_L2_Highlight_Optimized_Natural_Color	
L8	2015-03-29-00_00_2015-03-29-23_59_Landsat_8_L2_Highlight_Optimized_Natural_Color	
L8	2015-04-03-00_00_2015-04-03-23_59_Landsat_8_L2_Highlight_Optimized_Natural_Color	
L8	2015-04-05-00_00_2015-04-05-23_59_Landsat_8_L2_Highlight_Optimized_Natural_Color	
L8	2015-04-07-00_00_2015-04-07-23_59_Landsat_8_L2_Highlight_Optimized_Natural_Color	
L8	2015-04-12-00_00_2015-04-12-23_59_Landsat_8_L2_Highlight_Optimized_Natural_Color	
L8	2015-04-12-00_00_2015-04-12-23_59_Landsat_8_L2_Highlight_Optimized_Natural_Color	
L8	2015-04-28-00_00_2015-04-28-23_59_Landsat_8_L2_Highlight_Optimized_Natural_Color	
L8	2015-04-30-00_00_2015-04-30-23_59_Landsat_8_L2_Highlight_Optimized_Natural_Color	
L8	2015-05-05-00_00_2015-05-05-23_59_Landsat_8_L2_Highlight_Optimized_Natural_Color	
L8	2015-05-07-00_00_2015-05-07-23_59_Landsat_8_L2_Highlight_Optimized_Natural_Color	
L8	2015-05-09-00_00_2015-05-09-23_59_Landsat_8_L2_Highlight_Optimized_Natural_Color	
L8	2015-05-16-00_00_2015-05-16-23_59_Landsat_8_L2_Highlight_Optimized_Natural_Color	
L8	2015-05-25-00_00_2015-05-25-23_59_Landsat_8_L2_Highlight_Optimized_Natural_Color	
L8	2015-06-06-00_00_2015-06-06-23_59_Landsat_8_L2_Highlight_Optimized_Natural_Color	
L8	2015-06-15-00_00_2015-06-15-23_59_Landsat_8_L2_Highlight_Optimized_Natural_Color	
L8	2015-06-24-00_00_2015-06-24-23_59_Landsat_8_L2_Highlight_Optimized_Natural_Color	
L8	2015-07-03-00_00_2015-07-03-23_59_Landsat_8_L2_Highlight_Optimized_Natural_Color	
L8	2015-07-08-00_00_2015-07-08-23_59_Landsat_8_L2_Highlight_Optimized_Natural_Color	
L8	2015-07-10-00_00_2015-07-10-23_59_Landsat_8_L2_Highlight_Optimized_Natural_Color	
L8	2015-07-12-00_00_2015-07-12-23_59_Landsat_8_L2_Highlight_Optimized_Natural_Color	
L8	2015-07-17-00_00_2015-07-17-23_59_Landsat_8_L2_Highlight_Optimized_Natural_Color	
L8	2015-07-19-00_00_2015-07-19-23_59_Landsat_8_L2_Highlight_Optimized_Natural_Color	
L8	2015-07-24-00_00_2015-07-24-23_59_Landsat_8_L2_Highlight_Optimized_Natural_Color	
L8	2015-07-26-00_00_2015-07-26-23_59_Landsat_8_L2_Highlight_Optimized_Natural_Color	
L8	2015-07-28-00_00_2015-07-28-23_59_Landsat_8_L2_Highlight_Optimized_Natural_Color	
L8	2015-08-02-00_00_2015-08-02-23_59_Landsat_8_L2_Highlight_Optimized_Natural_Color	
L8	2015-08-09-00_00_2015-08-09-23_59_Landsat_8_L2_Highlight_Optimized_Natural_Color	37

L8 2015-08-11-00_00_2015-08-11-23_59_Landsat_8_L2_Highlight_Optimized_Natural_Color
L8 2015-08-13-00_00_2015-08-13-23_59_Landsat_8_L2_Highlight_Optimized_Natural_Color
L8 2015-08-18-00_00_2015-08-18-23_59_Landsat_8_L2_Highlight_Optimized_Natural_Color
L8 2015-08-25-00_00_2015-08-25-23_59_Landsat_8_L2_Highlight_Optimized_Natural_Color
L8 2015-08-27-00_00_2015-08-27-23_59_Landsat_8_L2_Highlight_Optimized_Natural_Color
L8 2015-09-12-00_00_2015-09-12-23_59_Landsat_8_L2_Highlight_Optimized_Natural_Color

2016

L8 2016-08-13-00_00_2016-08-13-23_59_Landsat_8_L2_Highlight_Optimized_Natural_Color
L8 2016-08-15-00_00_2016-08-15-23_59_Landsat_8_L2_Highlight_Optimized_Natural_Color
L8 2016-08-27-00_00_2016-08-27-23_59_Landsat_8_L2_Highlight_Optimized_Natural_Color
L8 2016-08-29-00_00_2016-08-29-23_59_Landsat_8_L2_Highlight_Optimized_Natural_Color
L8 2016-09-23-00_00_2016-09-23-23_59_Landsat_8_L2_Highlight_Optimized_Natural_Color
L8 2016-03-20-00:00_2016-03-20-23:59_Landsat_8_L2_Highlight_Optimized_Natural_Color
L8 2016-03-22-00:00_2016-03-22-23:59_Landsat_8_L2_Highlight_Optimized_Natural_Color
L8 2016-03-24-00:00_2016-03-24-23:59_Landsat_8_L2_Highlight_Optimized_Natural_Color
L8 2016-03-29-00:00_2016-03-29-23:59_Landsat_8_L2_Highlight_Optimized_Natural_Color
L8 2016-03-31-00:00_2016-03-31-23:59_Landsat_8_L2_Highlight_Optimized_Natural_Color
L8 2016-04-05-00:00_2016-04-05-23:59_Landsat_8_L2_Highlight_Optimized_Natural_Color
L8 2016-04-07-00:00_2016-04-07-23:59_Landsat_8_L2_Highlight_Optimized_Natural_Color
L8 2016-04-14-00:00_2016-04-14-23:59_Landsat_8_L2_Highlight_Optimized_Natural_Color
L8 2016-04-16-00:00_2016-04-16-23:59_Landsat_8_L2_Highlight_Optimized_Natural_Color
L8 2016-04-23-00:00_2016-04-23-23:59_Landsat_8_L2_Highlight_Optimized_Natural_Color
L8 2016-04-30-00:00_2016-04-30-23:59_Landsat_8_L2_Highlight_Optimized_Natural_Color
L8 2016-05-07-00:00_2016-05-07-23:59_Landsat_8_L2_Highlight_Optimized_Natural_Color
L8 2016-05-09-00:00_2016-05-09-23:59_Landsat_8_L2_Highlight_Optimized_Natural_Color
L8 2016-05-11-00:00_2016-05-11-23:59_Landsat_8_L2_Highlight_Optimized_Natural_Color
L8 2016-05-25-00:00_2016-05-25-23:59_Landsat_8_L2_Highlight_Optimized_Natural_Color
L8 2016-05-27-00:00_2016-05-27-23:59_Landsat_8_L2_Highlight_Optimized_Natural_Color
L8 2016-06-10-00:00_2016-06-10-23:59_Landsat_8_L2_Highlight_Optimized_Natural_Color
L8 2016-06-17-00:00_2016-06-17-23:59_Landsat_8_L2_Highlight_Optimized_Natural_Color
L8 2016-06-19-00:00_2016-06-19-23:59_Landsat_8_L2_Highlight_Optimized_Natural_Color
L8 2016-06-24-00:00_2016-06-24-23:59_Landsat_8_L2_Highlight_Optimized_Natural_Color
L8 2016-06-28-00:00_2016-06-28-23:59_Landsat_8_L2_Highlight_Optimized_Natural_Color
L8 2016-07-03-00:00_2016-07-03-23:59_Landsat_8_L2_Highlight_Optimized_Natural_Color
L8 2016-07-05-00:00_2016-07-05-23:59_Landsat_8_L2_Highlight_Optimized_Natural_Color
L8 2016-07-10-00:00_2016-07-10-23:59_Landsat_8_L2_Highlight_Optimized_Natural_Color
L8 2016-07-12-00:00_2016-07-12-23:59_Landsat_8_L2_Highlight_Optimized_Natural_Color
L8 2016-07-28-00:00_2016-07-28-23:59_Landsat_8_L2_Highlight_Optimized_Natural_Color
L8 2016-08-06-00:00_2016-08-06-23:59_Landsat_8_L2_Highlight_Optimized_Natural_Color
L8 2016-08-11-00:00_2016-08-11-23:59_Landsat_8_L2_Highlight_Optimized_Natural_Color 33

2017

S2 2017-03-19-00:00_2017-03-19-23:59_Sentinel-2_L1C_Highlight_Optimized_Natural_Color
S2 2017-03-19-00:00_2017-03-19-23:59_Sentinel-2_L1C_SWIR
L8 2017-03-23-00:00_2017-03-23-23:59_Landsat_8_L2_Highlight_Optimized_Natural_Color
L8 2017-03-27-00:00_2017-03-27-23:59_Landsat_8_L2_Highlight_Optimized_Natural_Color 66

L8 2017-04-01-00:00_2017-04-01-23:59_Landsat_8_L2_Highlight_Optimized_Natural_Color
L8 2017-07-15-00:00_2017-07-15-23:59_Landsat_8_L2_Highlight_Optimized_Natural_Color
S2 2017-04-15-00:00_2017-04-15-23:59_Sentinel-2_L1C_Highlight_Optimized_Natural_Color
S2 2017-04-15-00:00_2017-04-15-23:59_Sentinel-2_L1C_SWIR
L8 2017-04-19-00:00_2017-04-19-23:59_Landsat_8_L2_Highlight_Optimized_Natural_Color
L8 2017-04-24-00:00_2017-04-24-23:59_Landsat_8_L2_Highlight_Optimized_Natural_Color
L8 2017-04-26-00:00_2017-04-26-23:59_Landsat_8_L2_Highlight_Optimized_Natural_Color
L8 2017-04-28-00:00_2017-04-28-23:59_Landsat_8_L2_Highlight_Optimized_Natural_Color
S2 2017-04-28-00:00_2017-04-28-23:59_Sentinel-2_L1C_Highlight_Optimized_Natural_Color
S2 2017-04-28-00:00_2017-04-28-23:59_Sentinel-2_L1C_SWIR
L8 2017-05-05-00:00_2017-05-05-23:59_Landsat_8_L2_Highlight_Optimized_Natural_Color
S2 2017-05-05-00:00_2017-05-05-23:59_Sentinel-2_L1C_Highlight_Optimized_Natural_Color
S2 2017-05-05-00:00_2017-05-05-23:59_Sentinel-2_L1C_SWIR
L8 2017-05-14-00:00_2017-05-14-23:59_Landsat_8_L2_Highlight_Optimized_Natural_Color
L8 2017-05-28-00:00_2017-05-28-23:59_Landsat_8_L2_Highlight_Optimized_Natural_Color
L8 2017-06-06-00:00_2017-06-06-23:59_Landsat_8_L2_Highlight_Optimized_Natural_Color
S2 2017-06-07-00:00_2017-06-07-23:59_Sentinel-2_L1C_Highlight_Optimized_Natural_Color
S2 2017-06-07-00:00_2017-06-07-23:59_Sentinel-2_L1C_SWIR
L8 2017-06-20-00:00_2017-06-20-23:59_Landsat_8_L2_Highlight_Optimized_Natural_Color
L8 2017-06-22-00:00_2017-06-22-23:59_Landsat_8_L2_Highlight_Optimized_Natural_Color
L8 2017-06-29-00:00_2017-06-29-23:59_Landsat_8_L2_Highlight_Optimized_Natural_Color
S2 2017-06-29-00:00_2017-06-29-23:59_Sentinel-2_L1C_Highlight_Optimized_Natural_Color
S2 2017-06-29-00:00_2017-06-29-23:59_Sentinel-2_L1C_SWIR
S2 2017-07-04-00:00_2017-07-04-23:59_Sentinel-2_L1C_Highlight_Optimized_Natural_Color
S2 2017-07-04-00:00_2017-07-04-23:59_Sentinel-2_L1C_SWIR
L8 2017-07-06-00:00_2017-07-06-23:59_Landsat_8_L2_Highlight_Optimized_Natural_Color
L8 2017-07-08-00:00_2017-07-08-23:59_Landsat_8_L2_Highlight_Optimized_Natural_Color
S2 2017-07-10-00:00_2017-07-10-23:59_Sentinel-2_L1C_Highlight_Optimized_Natural_Color
S2 2017-07-10-00:00_2017-07-10-23:59_Sentinel-2_L1C_SWIR
L8 2017-07-13-00:00_2017-07-13-23:59_Landsat_8_L2_Highlight_Optimized_Natural_Color
S2 2017-07-15-00:00_2017-07-15-23:59_Sentinel-2_L1C_Highlight_Optimized_Natural_Color
S2 2017-07-15-00:00_2017-07-15-23:59_Sentinel-2_L1C_SWIR
L8 2017-07-17-00:00_2017-07-17-23:59_Landsat_8_L2_Highlight_Optimized_Natural_Color
S2 2017-07-17-00:00_2017-07-17-23:59_Sentinel-2_L1C_Highlight_Optimized_Natural_Color
S2 2017-07-17-00:00_2017-07-17-23:59_Sentinel-2_L1C_SWIR
S2 2017-07-19-00:00_2017-07-19-23:59_Sentinel-2_L1C_Highlight_Optimized_Natural_Color
S2 2017-07-19-00:00_2017-07-19-23:59_Sentinel-2_L1C_SWIR
L8 2017-07-24-00:00_2017-07-24-23:59_Landsat_8_L2_Highlight_Optimized_Natural_Color
S2 2017-08-01-00:00_2017-08-01-23:59_Sentinel-2_L1C_Highlight_Optimized_Natural_Color
S2 2017-08-01-00:00_2017-08-01-23:59_Sentinel-2_L1C_SWIR
L8 2017-08-02-00:00_2017-08-02-23:59_Landsat_8_L2_Highlight_Optimized_Natural_Color
S2 2017-08-06-00:00_2017-08-06-23:59_Sentinel-2_L1C_Highlight_Optimized_Natural_Color
S2 2017-08-06-00:00_2017-08-06-23:59_Sentinel-2_L1C_SWIR
L8 2017-08-14-00:00_2017-08-14-23:59_Landsat_8_L2_Highlight_Optimized_Natural_Color
L8 2017-08-16-00:00_2017-08-16-23:59_Landsat_8_L2_Highlight_Optimized_Natural_Color

L8 2017-08-18-00:00_2017-08-18-23:59_Landsat_8_L2_Highlight_Optimized_Natural_Color
S2 2017-08-19-00:00_2017-08-19-23:59_Sentinel-2_L1C_Highlight_Optimized_Natural_Color
S2 2017-08-19-00:00_2017-08-19-23:59_Sentinel-2_L1C_SWIR
S2 2017-08-21-00:00_2017-08-21-23:59_Sentinel-2_L1C_Highlight_Optimized_Natural_Color
S2 2017-08-21-00:00_2017-08-21-23:59_Sentinel-2_L1C_SWIR
L8 2017-08-30-00:00_2017-08-30-23:59_Landsat_8_L2_Highlight_Optimized_Natural_Color
S2 2017-09-02-00:00_2017-09-02-23:59_Sentinel-2_L1C_Highlight_Optimized_Natural_Color
S2 2017-09-02-00:00_2017-09-02-23:59_Sentinel-2_L1C_SWIR
S2 2017-09-10-00:00_2017-09-10-23:59_Sentinel-2_L1C_Highlight_Optimized_Natural_Color
S2 2017-09-10-00:00_2017-09-10-23:59_Sentinel-2_L1C_SWIR
S2 2017-09-15-00:00_2017-09-15-23:59_Sentinel-2_L1C_Highlight_Optimized_Natural_Color
S2 2017-09-15-00:00_2017-09-15-23:59_Sentinel-2_L1C_SWIR
S2 2017-09-22-00:00_2017-09-22-23:59_Sentinel-2_L1C_Highlight_Optimized_Natural_Color
S2 2017-09-22-00:00_2017-09-22-23:59_Sentinel-2_L1C_SWIR
L8 2017-09-24-00:00_2017-09-24-23:59_Landsat_8_L2_Highlight_Optimized_Natural_Color
S2 2017-09-30-00:00_2017-09-30-23:59_Sentinel-2F_L1C_Highlight_Optimized_Natural_Color.tiff
S2 2017-09-30-00:00_2017-09-30-23:59_Sentinel-2_L1C_SWIR

2018

L8 2018-03-19-00:00_2018-03-19-23:59_Landsat_8_L2_Highlight_Optimized_Natural_Color
L8 2018-03-21-00:00_2018-03-21-23:59_Landsat_8_L2_Highlight_Optimized_Natural_Color
S2 2018-03-29-00:00_2018-03-29-23:59_Sentinel-2_L1C_Highlight_Optimized_Natural_Color
S2 2018-03-29-00:00_2018-03-29-23:59_Sentinel-2_L1C_SWIR
L8 2018-03-30-00:00_2018-03-30-23:59_Landsat_8_L2_Highlight_Optimized_Natural_Color
L8 2018-04-04-00:00_2018-04-04-23:59_Landsat_8_L2_Highlight_Optimized_Natural_Color
L8 2018-04-06-00:00_2018-04-06-23:59_Landsat_8_L2_Highlight_Optimized_Natural_Color
L8 2018-04-11-00:00_2018-04-11-23:59_Landsat_8_L2_Highlight_Optimized_Natural_Color
L8 2018-04-15-00:00_2018-04-15-23:59_Landsat_8_L2_Highlight_Optimized_Natural_Color
L8 2018-04-22-00:00_2018-04-22-23:59_Landsat_8_L2_Highlight_Optimized_Natural_Color
S2 2018-04-30-00:00_2018-04-30-23:59_Sentinel-2_L1C_Highlight_Optimized_Natural_Color
S2 2018-04-30-00:00_2018-04-30-23:59_Sentinel-2_L1C_SWIR
L8 2018-05-01-00:00_2018-05-01-23:59_Landsat_8_L2_Highlight_Optimized_Natural_Color
L8 2018-05-13-00:00_2018-05-13-23:59_Landsat_8_L2_Highlight_Optimized_Natural_Color
L8 2018-05-17-00:00_2018-05-17-23:59_Landsat_8_L2_Highlight_Optimized_Natural_Color
L8 2018-05-22-00:00_2018-05-22-23:59_Landsat_8_L2_Highlight_Optimized_Natural_Color
L8 2018-06-07-00:00_2018-06-07-23:59_Landsat_8_L2_Highlight_Optimized_Natural_Color
L8 2018-06-14-00:00_2018-06-14-23:59_Landsat_8_L2_Highlight_Optimized_Natural_Color
L8 2018-06-16-00:00_2018-06-16-23:59_Landsat_8_L2_Highlight_Optimized_Natural_Color
L8 2018-06-23-00:00_2018-06-23-23:59_Landsat_8_L2_Highlight_Optimized_Natural_Color
L8 2018-06-30-00:00_2018-06-30-23:59_Landsat_8_L2_Highlight_Optimized_Natural_Color
S2 2018-06-30-00:00_2018-06-30-23:59_Sentinel-2_L1C_Highlight_Optimized_Natural_Color
S2 2018-06-30-00:00_2018-06-30-23:59_Sentinel-2_L1C_SWIR
S2 2018-08-29-00:00_2018-08-29-23:59_Sentinel-2_L2A_Highlight_Optimized_Natural_Color
S2 2018-08-29-00:00_2018-08-29-23:59_Sentinel-2_L2A_SWIR
S2 2018-08-31-00:00_2018-08-31-23:59_Sentinel-2_L2A_Highlight_Optimized_Natural_Color 29

S2 2018-08-31-00:00_2018-08-31-23:59_Sentinel-2_L2A_SWIR
S2 2018-09-30-00:00_2018-09-30-23:59_Sentinel-2_L2A_Highlight_Optimized_Natural_Color
S2 2018-09-30-00:00_2018-09-30-23:59_Sentinel-2_L2A_SWIR

2019

S2 2019-03-15-00:00_2019-03-15-23:59_Sentinel-2_L2A_Highlight_Optimized_Natural_Color
S2 2019-03-15-00:00_2019-03-15-23:59_Sentinel-2_L2A_SWIR
L8/9 2019-03-17-00:00_2019-03-17-23:59_Landsat_8-9_L2_Highlight_Optimized_Natural_Color
S2 2019-03-17-00:00_2019-03-17-23:59_Sentinel-2_L2A_Highlight_Optimized_Natural_Color
S2 2019-03-17-00:00_2019-03-17-23:59_Sentinel-2_L2A_SWIR
S2 2019-03-19-00:00_2019-03-19-23:59_Sentinel-2_L2A_Highlight_Optimized_Natural_Color
S2 2019-03-19-00:00_2019-03-19-23:59_Sentinel-2_L2A_SWIR
L8/9 2019-03-22-00:00_2019-03-22-23:59_Landsat_8-9_L2_Highlight_Optimized_Natural_Color
L8/9 2019-03-24-00:00_2019-03-24-23:59_Landsat_8-9_L2_Highlight_Optimized_Natural_Color
L8/9 2019-03-29-00:00_2019-03-29-23:59_Landsat_8-9_L2_Highlight_Optimized_Natural_Color
S2 2019-03-29-00:00_2019-03-29-23:59_Sentinel-2_L2A_Highlight_Optimized_Natural_Color
S2 2019-03-29-00:00_2019-03-29-23:59_Sentinel-2_L2A_SWIR
L8/9 2019-04-02-00:00_2019-04-02-23:59_Landsat_8-9_L2_Highlight_Optimized_Natural_Color
L8/9 2019-04-09-00:00_2019-04-09-23:59_Landsat_8-9_L2_Highlight_Optimized_Natural_Color
L8/9 2019-04-14-00:00_2019-04-14-23:59_Landsat_8-9_L2_Highlight_Optimized_Natural_Color
L8/9 2019-04-16-00:00_2019-04-16-23:59_Landsat_8-9_L2_Highlight_Optimized_Natural_Color
S2 2019-04-16-00:00_2019-04-16-23:59_Sentinel-2_L2A_Highlight_Optimized_Natural_Color
S2 2019-04-16-00:00_2019-04-16-23:59_Sentinel-2_L2A_SWIR
L8/9 2019-04-18-00:00_2019-04-18-23:59_Landsat_8-9_L2_Highlight_Optimized_Natural_Color
S2 2019-04-20-00:00_2019-04-20-23:59_Sentinel-2_L2A_Highlight_Optimized_Natural_Color
S2 2019-04-20-00:00_2019-04-20-23:59_Sentinel-2_L2A_SWIR
L8/9 2019-04-23-00:00_2019-04-23-23:59_Landsat_8-9_L2_Highlight_Optimized_Natural_Color
S2 2019-05-05-00:00_2019-05-05-23:59_Sentinel-2_L2A_Highlight_Optimized_Natural_Color
S2 2019-05-05-00:00_2019-05-05-23:59_Sentinel-2_L2A_SWIR
S2 2019-05-13-00:00_2019-05-13-23:59_Sentinel-2_L2A_Highlight_Optimized_Natural_Color
S2 2019-05-13-00:00_2019-05-13-23:59_Sentinel-2_L2A_SWIR
L8/9 2019-05-16-00:00_2019-05-16-23:59_Landsat_8-9_L2_Highlight_Optimized_Natural_Color
L8/9 2019-05-20-00:00_2019-05-20-23:59_Landsat_8-9_L2_Highlight_Optimized_Natural_Color
S2 2019-05-23-00:00_2019-05-23-23:59_Sentinel-2_L2A_Highlight_Optimized_Natural_Color
S2 2019-05-23-00:00_2019-05-23-23:59_Sentinel-2_L2A_SWIR
S2 2019-05-29-00:00_2019-05-29-23:59_Sentinel-2_L2A_Highlight_Optimized_Natural_Color
S2 2019-05-29-00:00_2019-05-29-23:59_Sentinel-2_L2A_SWIR
L8/9 2019-06-01-00:00_2019-06-01-23:59_Landsat_8-9_L2_Highlight_Optimized_Natural_Color
S2 2019-06-08-00:00_2019-06-08-23:59_Sentinel-2_L2A_Highlight_Optimized_Natural_Color
S2 2019-06-08-00:00_2019-06-08-23:59_Sentinel-2_L2A_SWIR
S2 2019-06-20-00:00_2019-06-20-23:59_Sentinel-2_L2A_Highlight_Optimized_Natural_Color
S2 2019-06-20-00:00_2019-06-20-23:59_Sentinel-2_L2A_SWIR
S2 2019-06-24-00:00_2019-06-24-23:59_Sentinel-2_L2A_Highlight_Optimized_Natural_Color
S2 2019-06-24-00:00_2019-06-24-23:59_Sentinel-2_L2A_SWIR
L8/9 2019-06-26-00:00_2019-06-26-23:59_Landsat_8-9_L2_Highlight_Optimized_Natural_Color
S2 2019-06-26-00:00_2019-06-26-23:59_Sentinel-2_L2A_Highlight_Optimized_Natural_Color 92

S2 2019-06-26-00:00_2019-06-26-23:59_Sentinel-2_L2A_SWIR
L8/9 2019-06-28-00:00_2019-06-28-23:59_Landsat_8-9_L2_Highlight_Optimized_Natural_Color
S2 2019-06-28-00:00_2019-06-28-23:59_Sentinel-2_L2A_Highlight_Optimized_Natural_Color
S2 2019-06-28-00:00_2019-06-28-23:59_Sentinel-2_L2A_SWIR
S2 2019-06-30-00:00_2019-06-30-23:59_Sentinel-2_L2A_Highlight_Optimized_Natural_Color
S2 2019-06-30-00:00_2019-06-30-23:59_Sentinel-2_L2A_SWIR
S2 2019-07-01-00:00_2019-07-01-23:59_Sentinel-2_L2A_Highlight_Optimized_Natural_Color
S2 2019-07-01-00:00_2019-07-01-23:59_Sentinel-2_L2A_SWIR
L8/9 2019-07-03-00:00_2019-07-03-23:59_Landsat_8-9_L2_Highlight_Optimized_Natural_Color
S2 2019-07-03-00:00_2019-07-03-23:59_Sentinel-2_L2A_Highlight_Optimized_Natural_Color
S2 2019-07-03-00:00_2019-07-03-23:59_Sentinel-2_L2A_SWIR
L8/9 2019-07-05-00:00_2019-07-05-23:59_Landsat_8-9_L2_Highlight_Optimized_Natural_Color
S2 2019-07-05-00:00_2019-07-05-23:59_Sentinel-2_L2A_Highlight_Optimized_Natural_Color
S2 2019-07-05-00:00_2019-07-05-23:59_Sentinel-2_L2A_SWIR
S2 2019-07-09-00:00_2019-07-09-23:59_Sentinel-2_L2A_Highlight_Optimized_Natural_Color
S2 2019-07-09-00:00_2019-07-09-23:59_Sentinel-2_L2A_SWIR
L8/9 2019-07-14-00:00_2019-07-14-23:59_Landsat_8-9_L2_Highlight_Optimized_Natural_Color
S2 2019-07-29-00:00_2019-07-29-23:59_Sentinel-2_L2A_Highlight_Optimized_Natural_Color
S2 2019-07-29-00:00_2019-07-29-23:59_Sentinel-2_L2A_SWIR
S2 2019-07-31-00:00_2019-07-31-23:59_Sentinel-2_L2A_Highlight_Optimized_Natural_Color
S2 2019-07-31-00:00_2019-07-31-23:59_Sentinel-2_L2A_SWIR
S2 2019-08-03-00:00_2019-08-03-23:59_Sentinel-2_L2A_Highlight_Optimized_Natural_Color
S2 2019-08-03-00:00_2019-08-03-23:59_Sentinel-2_L2A_SWIR
L8/9 2019-08-04-00:00_2019-08-04-23:59_Landsat_8-9_L2_True_color
L8/9 2019-08-15-00:00_2019-08-15-23:59_Landsat_8-9_L2_Highlight_Optimized_Natural_Color
S2 2019-08-15-00:00_2019-08-15-23:59_Sentinel-2_L2A_Highlight_Optimized_Natural_Color
S2 2019-08-15-00:00_2019-08-15-23:59_Sentinel-2_L2A_SWIR
S2 2019-08-17-00:00_2019-08-17-23:59_Sentinel-2_L2A_Highlight_Optimized_Natural_Color
S2 2019-08-17-00:00_2019-08-17-23:59_Sentinel-2_L2A_SWIR
S2 2019-08-23-00:00_2019-08-23-23:59_Sentinel-2_L2A_Highlight_Optimized_Natural_Color
S2 2019-08-23-00:00_2019-08-23-23:59_Sentinel-2_L2A_SWIR
S2 2019-09-02-00:00_2019-09-02-23:59_Sentinel-2_L2A_Highlight_Optimized_Natural_Color
S2 2019-09-02-00:00_2019-09-02-23:59_Sentinel-2_L2A_SWIR
S2 2019-09-06-00:00_2019-09-06-23:59_Sentinel-2_L2A_Highlight_Optimized_Natural_Color
S2 2019-09-06-00:00_2019-09-06-23:59_Sentinel-2_L2A_SWIR
S2 2019-09-08-00:00_2019-09-08-23:59_Sentinel-2_L2A_Highlight_Optimized_Natural_Color
S2 2019-09-08-00:00_2019-09-08-23:59_Sentinel-2_L2A_SWIR
S2 2019-09-10-00:00_2019-09-10-23:59_Sentinel-2_L2A_Highlight_Optimized_Natural_Color
S2 2019-09-10-00:00_2019-09-10-23:59_Sentinel-2_L2A_SWIR
S2 2019-09-12-00:00_2019-09-12-23:59_Sentinel-2_L2A_Highlight_Optimized_Natural_Color
S2 2019-09-12-00:00_2019-09-12-23:59_Sentinel-2_L2A_SWIR
S2 2019-09-14-00:00_2019-09-14-23:59_Sentinel-2_L2A_Highlight_Optimized_Natural_Color
S2 2019-09-14-00:00_2019-09-14-23:59_Sentinel-2_L2A_SWIR
S2 2019-09-16-00:00_2019-09-16-23:59_Sentinel-2_L2A_Highlight_Optimized_Natural_Color
S2 2019-09-16-00:00_2019-09-16-23:59_Sentinel-2_L2A_SWIR

S2 2019-09-20-00:00_2019-09-20-23:59_Sentinel-2_L2A_Highlight_Optimized_Natural_Color
S2 2019-09-20-00:00_2019-09-20-23:59_Sentinel-2_L2A_SWIR
S2 2019-09-30-00:00_2019-09-30-23:59_Sentinel-2_L2A_Highlight_Optimized_Natural_Color
S2 2019-09-30-00:00_2019-09-30-23:59_Sentinel-2_L2A_SWIR
S2 2019-10-08-00:00_2019-10-08-23:59_Sentinel-2_L2A_Highlight_Optimized_Natural_Color
S2 2019-10-08-00:00_2019-10-08-23:59_Sentinel-2_L2A_SWIR

2020

S2 2020-03-05-00:00_2020-03-05-23:59_Sentinel-2_L2A_Highlight_Optimized_Natural_Color
S2 2020-03-05-00:00_2020-03-05-23:59_Sentinel-2_L2A_SWIR
S2 2020-03-11-00:00_2020-03-11-23:59_Sentinel-2_L2A_Highlight_Optimized_Natural_Color
S2 2020-03-11-00:00_2020-03-11-23:59_Sentinel-2_L2A_SWIR
S2 2020-03-13-00:00_2020-03-13-23:59_Sentinel-2_L2A_Highlight_Optimized_Natural_Color
S2 2020-03-13-00:00_2020-03-13-23:59_Sentinel-2_L2A_SWIR
L8/9 2020-03-19-00:00_2020-03-19-23:59_Landsat_8-9_L2_Highlight_Optimized_Natural_Color
S2 2020-03-19-00:00_2020-03-19-23:59_Sentinel-2_L2A_Highlight_Optimized_Natural_Color
S2 2020-03-19-00:00_2020-03-19-23:59_Sentinel-2_L2A_SWIR
S2 2020-03-29-00:00_2020-03-29-23:59_Sentinel-2_L2A_Highlight_Optimized_Natural_Color
S2 2020-03-29-00:00_2020-03-29-23:59_Sentinel-2_L2A_SWIR
L8/9 2020-03-31-00:00_2020-03-31-23:59_Landsat_8-9_L2_Highlight_Optimized_Natural_Color
S2 2020-03-31-00:00_2020-03-31-23:59_Sentinel-2_L2A_Highlight_Optimized_Natural_Color
S2 2020-03-31-00:00_2020-03-31-23:59_Sentinel-2_L2A_SWIR
L8/9 2020-04-02-00:00_2020-04-02-23:59_Landsat_8-9_L2_Highlight_Optimized_Natural_Color
S2 2020-04-02-00:00_2020-04-02-23:59_Sentinel-2_L2A_Highlight_Optimized_Natural_Color
S2 2020-04-02-00:00_2020-04-02-23:59_Sentinel-2_L2A_SWIR
L8/9 2020-04-04-00:00_2020-04-04-23:59_Landsat_8-9_L2_Highlight_Optimized_Natural_Color
S2 2020-04-10-00:00_2020-04-10-23:59_Sentinel-2_L2A_Highlight_Optimized_Natural_Color
S2 2020-04-10-00:00_2020-04-10-23:59_Sentinel-2_L2A_SWIR
S2 2020-04-14-00:00_2020-04-14-23:59_Sentinel-2_L2A_Highlight_Optimized_Natural_Color
S2 2020-04-14-00:00_2020-04-14-23:59_Sentinel-2_L2A_SWIR
L8/9 2020-04-16-00:00_2020-04-16-23:59_Landsat_8-9_L2_Highlight_Optimized_Natural_Color
L8/9 2020-04-18-00:00_2020-04-18-23:59_Landsat_8-9_L2_Highlight_Optimized_Natural_Color
S2 2020-04-22-00:00_2020-04-22-23:59_Sentinel-2_L2A_Highlight_Optimized_Natural_Color
S2 2020-04-22-00:00_2020-04-22-23:59_Sentinel-2_L2A_SWIR
S2 2020-04-24-00:00_2020-04-24-23:59_Sentinel-2_L2A_Highlight_Optimized_Natural_Color
S2 2020-04-24-00:00_2020-04-24-23:59_Sentinel-2_L2A_SWIR
L8/9 2020-05-02-00:00_2020-05-02-23:59_Landsat_8-9_L2_Highlight_Optimized_Natural_Color
S2 2020-05-02-00:00_2020-05-02-23:59_Sentinel-2_L2A_Highlight_Optimized_Natural_Color
S2 2020-05-02-00:00_2020-05-02-23:59_Sentinel-2_L2A_SWIR
S2 2020-05-08-00:00_2020-05-08-23:59_Sentinel-2_L2A_Highlight_Optimized_Natural_Color
S2 2020-05-08-00:00_2020-05-08-23:59_Sentinel-2_L2A_SWIR
L8/9 2020-05-11-00:00_2020-05-11-23:59_Landsat_8-9_L2_Highlight_Optimized_Natural_Color
L8/9 2020-05-20-00:00_2020-05-20-23:59_Landsat_8-9_L2_Highlight_Optimized_Natural_Color
L8/9 2020-05-20-00:00_2020-05-20-23:59_Landsat_8-9_L2_Highlight_Optimized_Natural_Color
S2 2020-05-20-00:00_2020-05-20-23:59_Sentinel-2_L2A_Highlight_Optimized_Natural_Color
S2 2020-05-20-00:00_2020-05-20-23:59_Sentinel-2_L2A_SWIR 103

S2 2020-05-24-00:00_2020-05-24-23:59_Sentinel-2_L2A_Highlight_Optimized_Natural_Color
S2 2020-05-24-00:00_2020-05-24-23:59_Sentinel-2_L2A_SWIR
S2 2020-05-28-00:00_2020-05-28-23:59_Sentinel-2_L2A_Highlight_Optimized_Natural_Color
S2 2020-05-28-00:00_2020-05-28-23:59_Sentinel-2_L2A_SWIR
L8/9 2020-05-29-00:00_2020-05-29-23:59_Landsat_8-9_L2_Highlight_Optimized_Natural_Color
L8/9 2020-06-05-00:00_2020-06-05-23:59_Landsat_8-9_L2_Highlight_Optimized_Natural_Color
S2 2020-06-06-00:00_2020-06-06-23:59_Sentinel-2_L2A_Highlight_Optimized_Natural_Color
S2 2020-06-06-00:00_2020-06-06-23:59_Sentinel-2_L2A_SWIR
S2 2020-06-08-00:00_2020-06-08-23:59_Sentinel-2_L2A_Highlight_Optimized_Natural_Color
S2 2020-06-08-00:00_2020-06-08-23:59_Sentinel-2_L2A_SWIR
L8/9 2020-06-12-00:00_2020-06-12-23:59_Landsat_8-9_L2_Highlight_Optimized_Natural_Color
L8/9 2020-06-14-00:00_2020-06-14-23:59_Landsat_8-9_L2_Highlight_Optimized_Natural_Color
S2 2020-06-14-00:00_2020-06-14-23:59_Sentinel-2_L2A_Highlight_Optimized_Natural_Color
S2 2020-06-14-00:00_2020-06-14-23:59_Sentinel-2_L2A_SWIR
S2 2020-06-16-00:00_2020-06-16-23:59_Sentinel-2_L2A_Highlight_Optimized_Natural_Color
S2 2020-06-16-00:00_2020-06-16-23:59_Sentinel-2_L2A_SWIR
L8/9 2020-06-19-00:00_2020-06-19-23:59_Landsat_8-9_L2_Highlight_Optimized_Natural_Color
L8/9 2020-06-23-00:00_2020-06-23-23:59_Landsat_8-9_L2_Highlight_Optimized_Natural_Color
S2 2020-06-24-00:00_2020-06-24-23:59_Sentinel-2_L2A_Highlight_Optimized_Natural_Color
S2 2020-06-24-00:00_2020-06-24-23:59_Sentinel-2_L2A_SWIR
L8/9 2020-06-26-00:00_2020-06-26-23:59_Landsat_8-9_L2_Highlight_Optimized_Natural_Color
S2 2020-06-26-00:00_2020-06-26-23:59_Sentinel-2_L2A_Highlight_Optimized_Natural_Color
S2 2020-06-26-00:00_2020-06-26-23:59_Sentinel-2_L2A_SWIR
L8/9 2020-06-28-00:00_2020-06-28-23:59_Landsat_8-9_L2_Highlight_Optimized_Natural_Color
S2 2020-06-28-00:00_2020-06-28-23:59_Sentinel-2_L2A_Highlight_Optimized_Natural_Color
S2 2020-06-28-00:00_2020-06-28-23:59_Sentinel-2_L2A_SWIR
S2 2020-07-01-00:00_2020-07-01-23:59_Sentinel-2_L2A_Highlight_Optimized_Natural_Color
S2 2020-07-01-00:00_2020-07-01-23:59_Sentinel-2_L2A_SWIR
S2 2020-07-05-00:00_2020-07-05-23:59_Sentinel-2_L2A_Highlight_Optimized_Natural_Color
S2 2020-07-05-00:00_2020-07-05-23:59_Sentinel-2_L2A_SWIR
S2 2020-07-09-00:00_2020-07-09-23:59_Sentinel-2_L2A_Highlight_Optimized_Natural_Color
S2 2020-07-09-00:00_2020-07-09-23:59_Sentinel-2_L2A_SWIR
S2 2020-07-13-00:00_2020-07-13-23:59_Sentinel-2_L2A_Highlight_Optimized_Natural_Color
S2 2020-07-13-00:00_2020-07-13-23:59_Sentinel-2_L2A_SWIR
S2 2020-07-19-00:00_2020-07-19-23:59_Sentinel-2_L2A_Highlight_Optimized_Natural_Color
S2 2020-07-19-00:00_2020-07-19-23:59_Sentinel-2_L2A_SWIR
L8/9 2020-07-21-00:00_2020-07-21-23:59_Landsat_8-9_L2_Highlight_Optimized_Natural_Color
S2 2020-07-21-00:00_2020-07-21-23:59_Sentinel-2_L2A_Highlight_Optimized_Natural_Color
S2 2020-07-21-00:00_2020-07-21-23:59_Sentinel-2_L2A_SWIR
S2 2020-07-23-00:00_2020-07-23-23:59_Sentinel-2_L2A_Highlight_Optimized_Natural_Color
S2 2020-07-23-00:00_2020-07-23-23:59_Sentinel-2_L2A_SWIR
L8/9 2020-07-25-00:00_2020-07-25-23:59_Landsat_8-9_L2_Highlight_Optimized_Natural_Color
S2 2020-07-25-00:00_2020-07-25-23:59_Sentinel-2_L2A_Highlight_Optimized_Natural_Color
S2 2020-07-25-00:00_2020-07-25-23:59_Sentinel-2_L2A_SWIR
S2 2020-08-03-00:00_2020-08-03-23:59_Sentinel-2_L2A_Highlight_Optimized_Natural_Color

S2 2020-08-03-00:00_2020-08-03-23:59_Sentinel-2_L2A_SWIR
S2 2020-08-05-00:00_2020-08-05-23:59_Sentinel-2_L2A_Highlight_Optimized_Natural_Color
S2 2020-08-05-00:00_2020-08-05-23:59_Sentinel-2_L2A_SWIR
S2 2020-08-07-00:00_2020-08-07-23:59_Sentinel-2_L2A_Highlight_Optimized_Natural_Color
S2 2020-08-07-00:00_2020-08-07-23:59_Sentinel-2_L2A_SWIR
S2 2020-08-09-00:00_2020-08-09-23:59_Sentinel-2_L2A_Highlight_Optimized_Natural_Color
S2 2020-08-09-00:00_2020-08-09-23:59_Sentinel-2_L2A_SWIR
S2 2020-09-03-00:00_2020-09-03-23:59_Sentinel-2_L2A_Highlight_Optimized_Natural_Color
S2 2020-09-03-00:00_2020-09-03-23:59_Sentinel-2_L2A_SWIR
S2 2020-09-05-00:00_2020-09-05-23:59_Sentinel-2_L2A_Highlight_Optimized_Natural_Color
S2 2020-09-05-00:00_2020-09-05-23:59_Sentinel-2_L2A_SWIR
S2 2020-09-07-00:00_2020-09-07-23:59_Sentinel-2_L2A_Highlight_Optimized_Natural_Color
S2 2020-09-07-00:00_2020-09-07-23:59_Sentinel-2_L2A_SWIR
S2 2020-09-15-00:00_2020-09-15-23:59_Sentinel-2_L2A_Highlight_Optimized_Natural_Color
S2 2020-09-15-00:00_2020-09-15-23:59_Sentinel-2_L2A_SWIR
S2 2020-09-17-00:00_2020-09-17-23:59_Sentinel-2_L2A_Highlight_Optimized_Natural_Color
S2 2020-09-17-00:00_2020-09-17-23:59_Sentinel-2_L2A_SWIR
S2 2020-09-20-00:00_2020-09-20-23:59_Sentinel-2_L2A_Highlight_Optimized_Natural_Color
S2 2020-09-20-00:00_2020-09-20-23:59_Sentinel-2_L2A_SWIR
S2 2020-09-28-00:00_2020-09-28-23:59_Sentinel-2_L2A_Highlight_Optimized_Natural_Color

2021

S2 2021-03-05-00:00_2021-03-05-23:59_Sentinel-2_L2A_Highlight_Optimized_Natural_Color
S2 2021-03-05-00:00_2021-03-05-23:59_Sentinel-2_L2A_SWIR
S2 2021-03-11-00:00_2021-03-11-23:59_Sentinel-2_L2A_Highlight_Optimized_Natural_Color
S2 2021-03-11-00:00_2021-03-11-23:59_Sentinel-2_L2A_SWIR
S2 2021-03-13-00:00_2021-03-13-23:59_Sentinel-2_L2A_Highlight_Optimized_Natural_Color
S2 2021-03-13-00:00_2021-03-13-23:59_Sentinel-2_L2A_SWIR
S2 2021-03-15-00:00_2021-03-15-23:59_Sentinel-2_L2A_Highlight_Optimized_Natural_Color
S2 2021-03-15-00:00_2021-03-15-23:59_Sentinel-2_L2A_SWIR
L8/9 2021-03-22-00:00_2021-03-22-23:59_Landsat_8-9_L2_Highlight_Optimized_Natural_Color
S2 2021-03-25-00:00_2021-03-25-23:59_Sentinel-2_L2A_Highlight_Optimized_Natural_Color
S2 2021-03-25-00:00_2021-03-25-23:59_Sentinel-2_L2A_SWIR
L8/9 2021-03-27-00:00_2021-03-27-23:59_Landsat_8-9_L2_Highlight_Optimized_Natural_Color
L8/9 2021-04-03-00:00_2021-04-03-23:59_Landsat_8-9_L2_Highlight_Optimized_Natural_Color
L8/9 2021-04-12-00:00_2021-04-12-23:59_Landsat_8-9_L2_Highlight_Optimized_Natural_Color
S2 2021-04-12-00:00_2021-04-12-23:59_Sentinel-2_L2A_Highlight_Optimized_Natural_Color
S2 2021-04-12-00:00_2021-04-12-23:59_Sentinel-2_L2A_SWIR
S2 2021-04-20-00:00_2021-04-20-23:59_Sentinel-2_L2A_Highlight_Optimized_Natural_Color
S2 2021-04-20-00:00_2021-04-20-23:59_Sentinel-2_L2A_SWIR
L8/9 2021-04-21-00:00_2021-04-21-23:59_Landsat_8-9_L2_Highlight_Optimized_Natural_Color
S2 2021-04-28-00:00_2021-04-28-23:59_Sentinel-2_L2A_Highlight_Optimized_Natural_Color
S2 2021-04-28-00:00_2021-04-28-23:59_Sentinel-2_L2A_SWIR
S2 2021-05-03-00:00_2021-05-03-23:59_Sentinel-2_L2A_Highlight_Optimized_Natural_Color
S2 2021-05-03-00:00_2021-05-03-23:59_Sentinel-2_L2A_SWIR
L8/9 2021-05-05-00:00_2021-05-05-23:59_Landsat_8-9_L2_Highlight_Optimized_Natural_Color 97

S2 2021-05-05-00:00_2021-05-05-23:59_Sentinel-2_L2A_Highlight_Optimized_Natural_Color
S2 2021-05-05-00:00_2021-05-05-23:59_Sentinel-2_L2A_SWIR
S2 2021-05-09-00:00_2021-05-09-23:59_Sentinel-2_L2A_Highlight_Optimized_Natural_Color
S2 2021-05-09-00:00_2021-05-09-23:59_Sentinel-2_L2A_SWIR
L8/9 2021-05-14-00:00_2021-05-14-23:59_Landsat_8-9_L2_Highlight_Optimized_Natural_Color
S2 2021-05-19-00:00_2021-05-19-23:59_Sentinel-2_L2A_Highlight_Optimized_Natural_Color
S2 2021-05-19-00:00_2021-05-19-23:59_Sentinel-2_L2A_SWIR
L8/9 2021-05-21-00:00_2021-05-21-23:59_Landsat_8-9_L2_Highlight_Optimized_Natural_Color
L8/9 2021-05-25-00:00_2021-05-25-23:59_Landsat_8-9_L2_Highlight_Optimized_Natural_Color
S2 2021-05-25-00:00_2021-05-25-23:59_Sentinel-2_L2A_Highlight_Optimized_Natural_Color
S2 2021-05-25-00:00_2021-05-25-23:59_Sentinel-2_L2A_SWIR
S2 2021-05-27-00:00_2021-05-27-23:59_Sentinel-2_L2A_Highlight_Optimized_Natural_Color
S2 2021-05-27-00:00_2021-05-27-23:59_Sentinel-2_L2A_SWIR
L8/9 2021-05-30-00:00_2021-05-30-23:59_Landsat_8-9_L2_Highlight_Optimized_Natural_Color
S2 2021-05-31-00:00_2021-05-31-23:59_Sentinel-2_L2A_Highlight_Optimized_Natural_Color
S2 2021-05-31-00:00_2021-05-31-23:59_Sentinel-2_L2A_SWIR
L8/9 2021-06-01-00:00_2021-06-01-23:59_Landsat_8-9_L2_Highlight_Optimized_Natural_Color
S2 2021-06-08-00:00_2021-06-08-23:59_Sentinel-2_L2A_Highlight_Optimized_Natural_Color
S2 2021-06-08-00:00_2021-06-08-23:59_Sentinel-2_L2A_SWIR
S2 2021-06-12-00:00_2021-06-12-23:59_Sentinel-2_L2A_Highlight_Optimized_Natural_Color
S2 2021-06-12-00:00_2021-06-12-23:59_Sentinel-2_L2A_SWIR
S2 2021-06-14-00:00_2021-06-14-23:59_Sentinel-2_L2A_Highlight_Optimized_Natural_Color
S2 2021-06-14-00:00_2021-06-14-23:59_Sentinel-2_L2A_SWIR
S2 2021-06-20-00:00_2021-06-20-23:59_Sentinel-2_L2A_Highlight_Optimized_Natural_Color
S2 2021-06-20-00:00_2021-06-20-23:59_Sentinel-2_L2A_SWIR
S2 2021-06-26-00:00_2021-06-26-23:59_Sentinel-2_L2A_Highlight_Optimized_Natural_Color
S2 2021-06-26-00:00_2021-06-26-23:59_Sentinel-2_L2A_SWIR
S2 2021-06-28-00:00_2021-06-28-23:59_Sentinel-2_L2A_Highlight_Optimized_Natural_Color
S2 2021-06-28-00:00_2021-06-28-23:59_Sentinel-2_L2A_SWIR
L8/9 2021-07-01-00:00_2021-07-01-23:59_Landsat_8-9_L2_Highlight_Optimized_Natural_Color
S2 2021-07-03-00:00_2021-07-03-23:59_Sentinel-2_L2A_Highlight_Optimized_Natural_Color
L8/9 2021-07-06-00:00_2021-07-06-23:59_Landsat_8-9_L2_Highlight_Optimized_Natural_Color
S2 2021-07-07-00:00_2021-07-07-23:59_Sentinel-2_L2A_Highlight_Optimized_Natural_Color
S2 2021-07-07-00:00_2021-07-07-23:59_Sentinel-2_L2A_SWIR
L8/9 2021-07-08-00:00_2021-07-08-23:59_Landsat_8-9_L2_Highlight_Optimized_Natural_Color
S2 2021-07-09-00:00_2021-07-09-23:59_Sentinel-2_L2A_Highlight_Optimized_Natural_Color
S2 2021-07-09-00:00_2021-07-09-23:59_Sentinel-2_L2A_SWIR
L8/9 2021-07-10-00:00_2021-07-10-23:59_Landsat_8-9_L2_Highlight_Optimized_Natural_Color
S2 2021-07-11-00:00_2021-07-11-23:59_Sentinel-2_L2A_Highlight_Optimized_Natural_Color
S2 2021-07-11-00:00_2021-07-11-23:59_Sentinel-2_L2A_SWIR
S2 2021-07-15-00:00_2021-07-15-23:59_Sentinel-2_L2A_Highlight_Optimized_Natural_Color
S2 2021-07-15-00:00_2021-07-15-23:59_Sentinel-2_L2A_SWIR
L8/9 2021-07-24-00:00_2021-07-24-23:59_Landsat_8-9_L2_Highlight_Optimized_Natural_Color
S2 2021-07-31-00:00_2021-07-31-23:59_Sentinel-2_L2A_Highlight_Optimized_Natural_Color
S2 2021-07-31-00:00_2021-07-31-23:59_Sentinel-2_L2A_SWIR

S2 2021-08-01-00:00_2021-08-01-23:59_Sentinel-2_L2A_Highlight_Optimized_Natural_Color
S2 2021-08-01-00:00_2021-08-01-23:59_Sentinel-2_L2A_SWIR
S2 2021-08-05-00:00_2021-08-05-23:59_Sentinel-2_L2A_Highlight_Optimized_Natural_Color
S2 2021-08-05-00:00_2021-08-05-23:59_Sentinel-2_L2A_SWIR
S2 2021-08-07-00:00_2021-08-07-23:59_Sentinel-2_L2A_Highlight_Optimized_Natural_Color
S2 2021-08-07-00:00_2021-08-07-23:59_Sentinel-2_L2A_SWIR
S2 2021-08-17-00:00_2021-08-17-23:59_Sentinel-2_L2A_Highlight_Optimized_Natural_Color
S2 2021-08-17-00:00_2021-08-17-23:59_Sentinel-2_L2A_SWIR
L8/9 2021-08-18-00:00_2021-08-18-23:59_Landsat_8-9_L2_Highlight_Optimized_Natural_Color
S2 2021-08-21-00:00_2021-08-21-23:59_Sentinel-2_L2A_Highlight_Optimized_Natural_Color
S2 2021-08-21-00:00_2021-08-21-23:59_Sentinel-2_L2A_SWIR
S2 2021-08-23-00:00_2021-08-23-23:59_Sentinel-2_L2A_Highlight_Optimized_Natural_Color
S2 2021-08-23-00:00_2021-08-23-23:59_Sentinel-2_L2A_SWIR
L8/9 2021-08-27-00:00_2021-08-27-23:59_Landsat_8-9_L2_Highlight_Optimized_Natural_Color
S2 2021-08-27-00:00_2021-08-27-23:59_Sentinel-2_L2A_Highlight_Optimized_Natural_Color
S2 2021-08-27-00:00_2021-08-27-23:59_Sentinel-2_L2A_SWIR
S2 2021-09-06-00:00_2021-09-06-23:59_Sentinel-2_L2A_Highlight_Optimized_Natural_Color
S2 2021-09-06-00:00_2021-09-06-23:59_Sentinel-2_L2A_SWIR
S2 2021-09-10-00:00_2021-09-10-23:59_Sentinel-2_L2A_Highlight_Optimized_Natural_Color
S2 2021-09-10-00:00_2021-09-10-23:59_Sentinel-2_L2A_SWIR
S2 2021-09-12-00:00_2021-09-12-23:59_Sentinel-2_L2A_Highlight_Optimized_Natural_Color
S2 2021-09-12-00:00_2021-09-12-23:59_Sentinel-2_L2A_SWIR
S2 2021-09-14-00:00_2021-09-14-23:59_Sentinel-2_L2A_Highlight_Optimized_Natural_Color
S2 2021-09-14-00:00_2021-09-14-23:59_Sentinel-2_L2A_SWIR
S2 2021-09-22-00:00_2021-09-22-23:59_Sentinel-2_L2A_Highlight_Optimized_Natural_Color
S2 2021-09-22-00:00_2021-09-22-23:59_Sentinel-2_L2A_SWIR
S2 2021-09-26-00:00_2021-09-26-23:59_Sentinel-2_L2A_Highlight_Optimized_Natural_Color
S2 2021-09-26-00:00_2021-09-26-23:59_Sentinel-2_L2A_SWIR